Malignant Tumors of Bone

17

Yong-Whee Bahk and Won-Jong Bahk

Malignant bone tumors are either primary or metastatic in nature. The high sensitivity and accuracy of ^{99m}Tc-MDP bone scintigraphy in diagnosing bone metastasis were established as long ago as 1961 (Fleming et al. 1961) (Fig. 1.2). In contrast, its usefulness in the investigation of primary bone tumors, both malignant and benign, appears not to be fully appreciated. The main reason is the low diagnostic yield of conventional planar bone scintigraphy; this is true. However, recognizing the fact that the magnified images of pinhole scintigraphy can depict anatomy in amazing detail along with unique metabolic information, a number of primary tumors and tumorlike diseases of bone have become among the most important and challenging indications for bone scanning.

In actuality ^{99m}Tc-MDP bone scintigraphy reinforced with the pinhole magnification technique and nuclear angiography has been demonstrated to be helpful in the diagnosis of primary bone tumors. The malignant tumors so far studied by this means include skeletal metastases and primary osteosarcoma, fibrosarcoma, Ewing's sarcoma, multiple myeloma, leukemia, and lymphoma, and the benign tumors comprise osteoid osteoma, enchondroma, osteochondroma, simple bone cyst, and giant cell tumor (Bahk 1996; Bahk 1998; Kim et al. 1992). The method has also been applied to (a) the mapping of the multiple lesions in polyostotic diseases such as enchondromatosis or Ollier's disease, familial exostosis, fibrous dysplasia, and histiocytosis X (Kirchner and Simon 1981); (b) preoperative localization of the nidus in osteoid osteoma in flat or irregular bones in particular (Lisbona and Rosenthall 1979); (c) detection of the intramedullary skip metastasis in osteosarcoma and giant cell tumor (Levine et al. 1984); (d) assessment of regional tumor extent; (e) evaluation of tumors with ambiguous radiographic and histological findings; (f) distinction among osteosarcoma, Ewing's sarcoma, and chondrosarcoma (McLean and Murray 1984) and between bone cyst and cystic bone lesions (Hudson 1984); and (g) unexplained bone pains.

The use of gallium-67 citrate, thallium-201 chloride, ^{99m}Tc-MIBI, and other agents for bone tumors is not considered in this chapter since these radiopharmaceuticals have fully been described in numerous publications including standard nuclear medicine textbooks and a number of excellent review articles (Nadel and Rossleigh 1995; Neumann et al. 1995; Waxman 1995; Focacci et al. 1998; Pinkas et al. 2001).

17.1 Metastasis

Radiography plays a relatively less crucial role in bone metastases in the early phase when bone changes are minimal or undetectable. It is also true that radiography is less suitable for the diagnosis of metastases in anatomically complex and thickly overshadowed bones or conversely in small or thin bones such as the cervical and thoracic vertebrae, the sternum, the ribs, the lumbosacral junction, and the sacroiliac joints. The reason is simply that osteolysis or neoplastic osteogenesis in those bones and structures is easily hidden unless the change is overt. Severe porosis in elderly and bedridden patients prevents radiographic detection of metastases and often makes conventional or computed tomography powerless. Not infrequently, however, ^{99m}Tc-MDP bone scintigraphy diagnoses radiographically invisible or uncertain metastases because they accumulate tracer emitting enough γ-rays from within porotic or thin bones (Fig. 17.1) or through thick or superimposed bones (Fig. 17.2). In addition, whole-body scanning advantageously permits scrutiny of the entire skeleton. In particular, the early metastasis of pediatric malignant tumors deserves a high index of suspicion in differential diagnosis (Bahk et al. 2017). For example, if only the skull is radiographed for local swelling on the forehead, the true state of affairs may be disguised as a local pathology, while the cranial lesion is just one of multiple metastases (Fig. 17.3).

Y.-W. Bahk, *Combined Scintigraphic and Radiographic Diagnosis of Bone and Joint Diseases*,
DOI 10.1007/978-981-10-2759-8_17

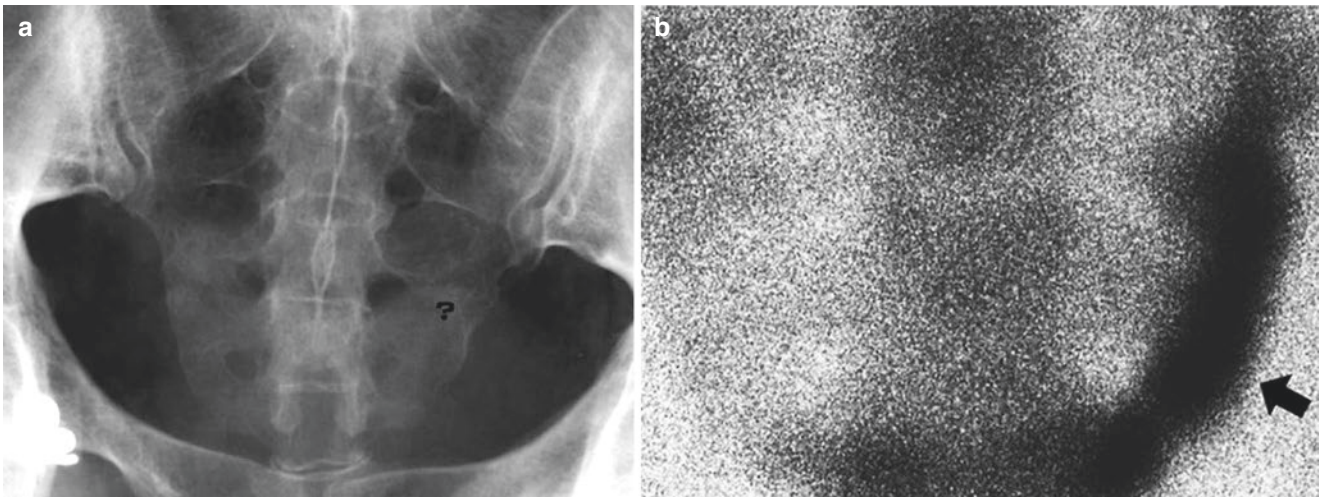

Fig. 17.1 Usefulness of bone scintigraphy in the diagnosis of metastasis. (**a**) Anteroposterior radiograph of the sacrum in a 37-year-old female with known primary breast cancer and left sacral pain shows no abnormality (*?*). (**b**) Anterior pinhole scintigraph reveals prominent tracer uptake along the left lateral sacral border representing metastasis (*arrow*)

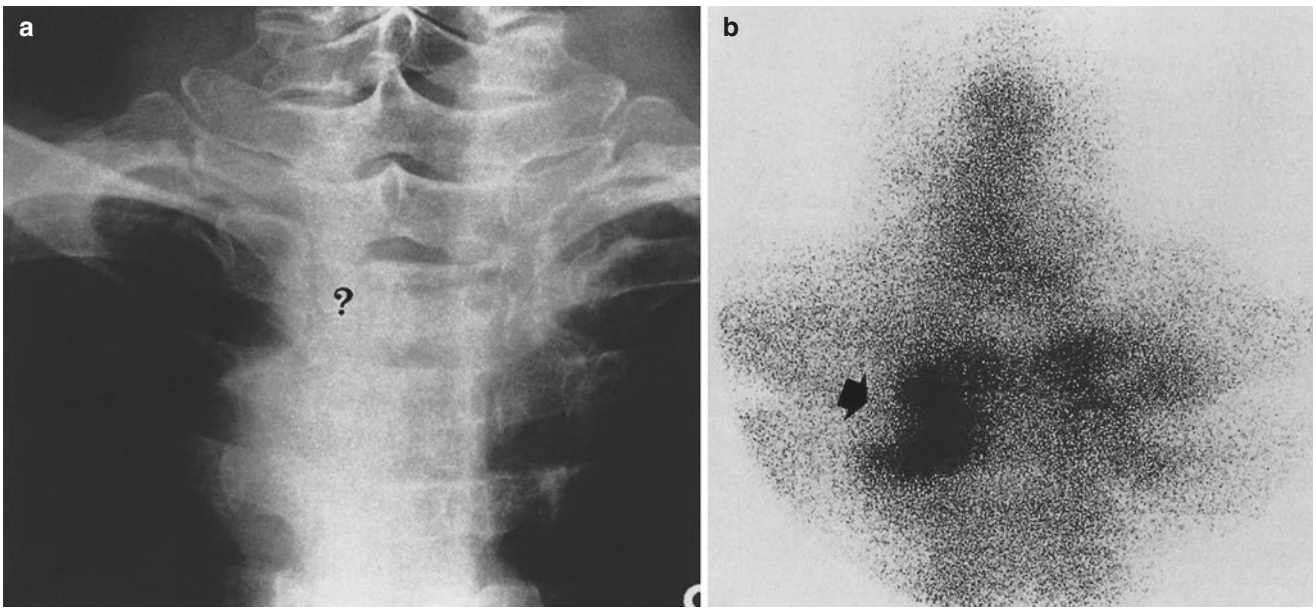

Fig. 17.2 Advantage of pinhole scintigraphy in the study of the diseases hidden in the overlapping structures of the thoracic cage and mediastinum. (**a**) Posteroanterior radiograph of the chest in a 63-year-old man with known bronchogenic carcinoma with a pain in the upper thoracic spine reveals no pathology (*?*). The radiograph is printed with the right side on the left to match the scintigraph. (**b**) Posterior pinhole scintigraph of the area in question reveals patchy tracer uptake in the left lateral aspect of the T3 vertebra, indicating metastasis (*arrow*)

Three basic radiographic changes of malignant metastases are osteolysis, osteogenesis, and a combination of both. The individual bone change is not specific by itself, but certain features or patterns are of diagnostic value. For example, the metastasis from renal cell carcinoma is often lytic and solitary (Fig. 17.4a), and the metastases from prostate carcinoma are usually osteoblastic and multiple or diffuse (Fig. 17.5a). It is also worth remembering that bronchogenic carcinomas, the squamous cell variety in particular (Greenspan and Norman 1988) (Fig. 17.6a), strongly tend to eccentrically metastasize to the cortex (Deutch and Resnick 1980), and multiple myeloma produces characteristic

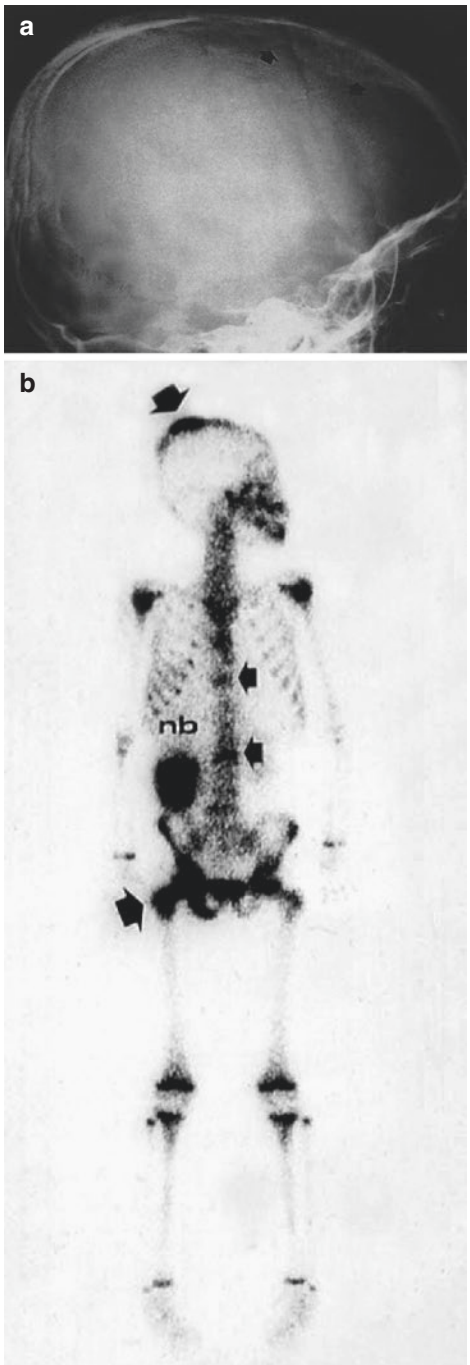

Fig. 17.3 Value of whole-body bone scintigraphy in bone tumor. (**a**) Lateral radiograph of the skull in an 8-year-old girl with a mass in the cranium shows diploic space widening and erosions in both the outer and inner tables (*arrows*). Differential diagnoses included meningioma which was considered most likely. (**b**) Anterior whole-body scintigraph clearly indicates that the cranial lesion is just one of many such lesions in the skeleton (*arrows*) and also the right kidney is caudally displaced (*nb*), correctly indicating the diagnosis of neuroblastoma with multiple skeletal metastases

punched-out or soap bubble-like lytic lesions in the skull, spine, pelvis, and proximal limb bones (Fig. 17.7a).

^{99m}Tc-MDP bone scanning is highly regarded for its ability to diagnose metastases, especially when the primary tumor has a great propensity toward early dissemination (Pistenma et al. 1975; Kirchner and Simon 1981). Its usefulness in detecting both distant and local intramedullary spread of a malignancy is well appreciated, making the study a sine qua non in the staging and managing of many malignant tumors (Fogelman and McKillop 1991) (Fig. 17.8). It should also be emphasized that ordinary scintigraphy has three pitfalls: relatively high false-negative results, ambiguous photopenic manifestation, and the lack of specificity in the majority of individual lesions. Previously, the incidence of false-negative bone scintigraphy in metastases was reported to be as high as 3% (Pistenma et al. 1975; Citrin and McKillop 1978). Publications also indicated that in a small percentage of patients, radiography could detect metastases that were not visualized on scintigraph. The main reasons are the smallness and photopenic presentation. However, many such lesions can correctly be diagnosed by properly using pinhole scintigraphy (the closer the detector to the objects, the higher the resolution and the greater the sensitivity), dramatically reducing the incidence of false-negative scans. Indeed, magnified scintigraphy can visualize not only tiny bone metastases (Fig. 17.9) but also soft-tissue invasion when richly vascularized or mineralized (Fig. 17.10).

On the other hand, elusive photopenic metastases can be identified as such by noting reactive tracer uptake in the periphery of the lesion on the pinhole scintigraph (Fig. 17.11). Among the primary malignancies whose metastatic lesions are often photopenic, carcinomas of the kidney (Kim et al. 1983) (Figs. 17.4 and 17.11), stomach (Fig. 17.12a), breast (Fig. 17.12b), larynx (Fig. 17.12c), and biliary tract (Fig. 17.12d) deserve mention. In addition, the involvement of certain bones has been related to malignant metastases. Examples are the "hot" areas in the calvaria, the scapula, the sternum, the pelvis, the vertebra, and the long-bone shaft (Kirchner and Simon 1981). Generally, however, no tumor-specific pattern of bone metastases has been recognized because the metastatic behavior of malignant tumors is so diverse and unpredictable. As shown in Fig. 17.13, different carcinomas can cause metastasis that shows exactly the same scintigraphic sign such as fusiform intracortical tracer uptake: the primary tumors were bronchogenic carcinoma in Fig. 17.13a and renal cell carcinoma in Fig. 17.13b. Conversely, it is also true that the same primary carcinomas create metastases of different types in two different bones at

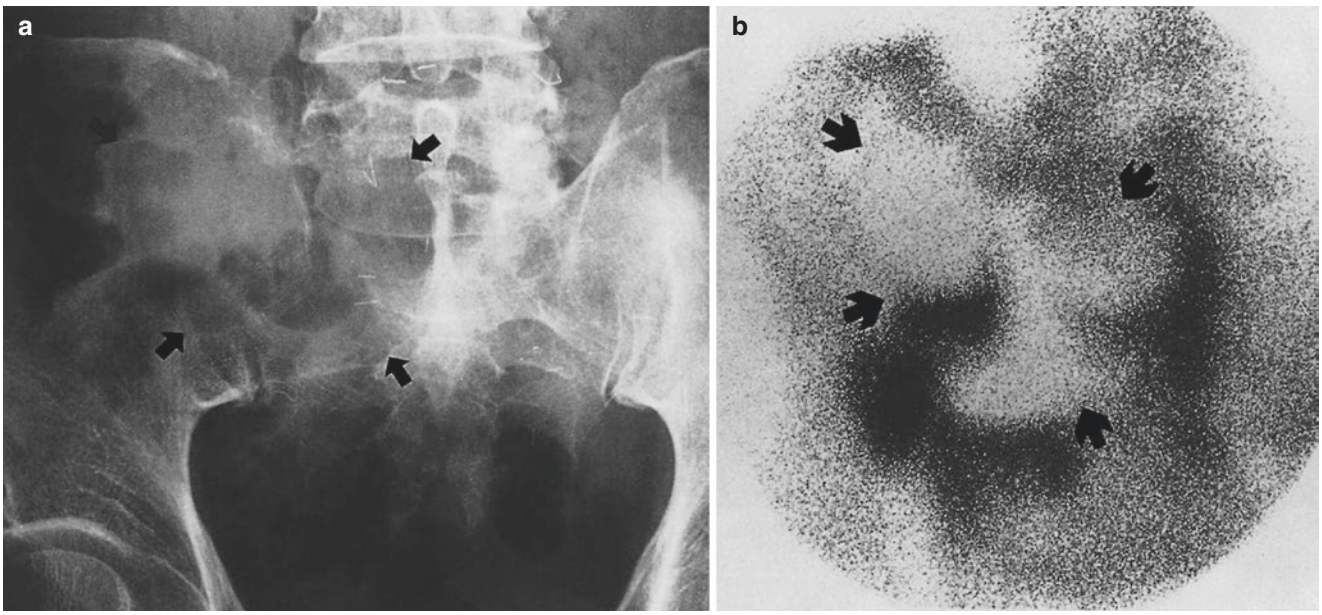

Fig. 17.4 Solitary osteolytic and photopenic metastasis in renal cell carcinoma. (**a**) Anteroposterior radiograph of the left iliac bone in a 48-year-old man with known renal cell carcinoma shows a large, irregularly shaped lysis in the left ilium and the neighboring sacrum (*arrows*). The radiograph is printed with the right side on the left to match the scintigraph. (**b**) Posterior pinhole scan shows a large, lobulated photon defect surrounded by intense tracer uptake in the left ilium and the neighboring sacrum (*arrows*)

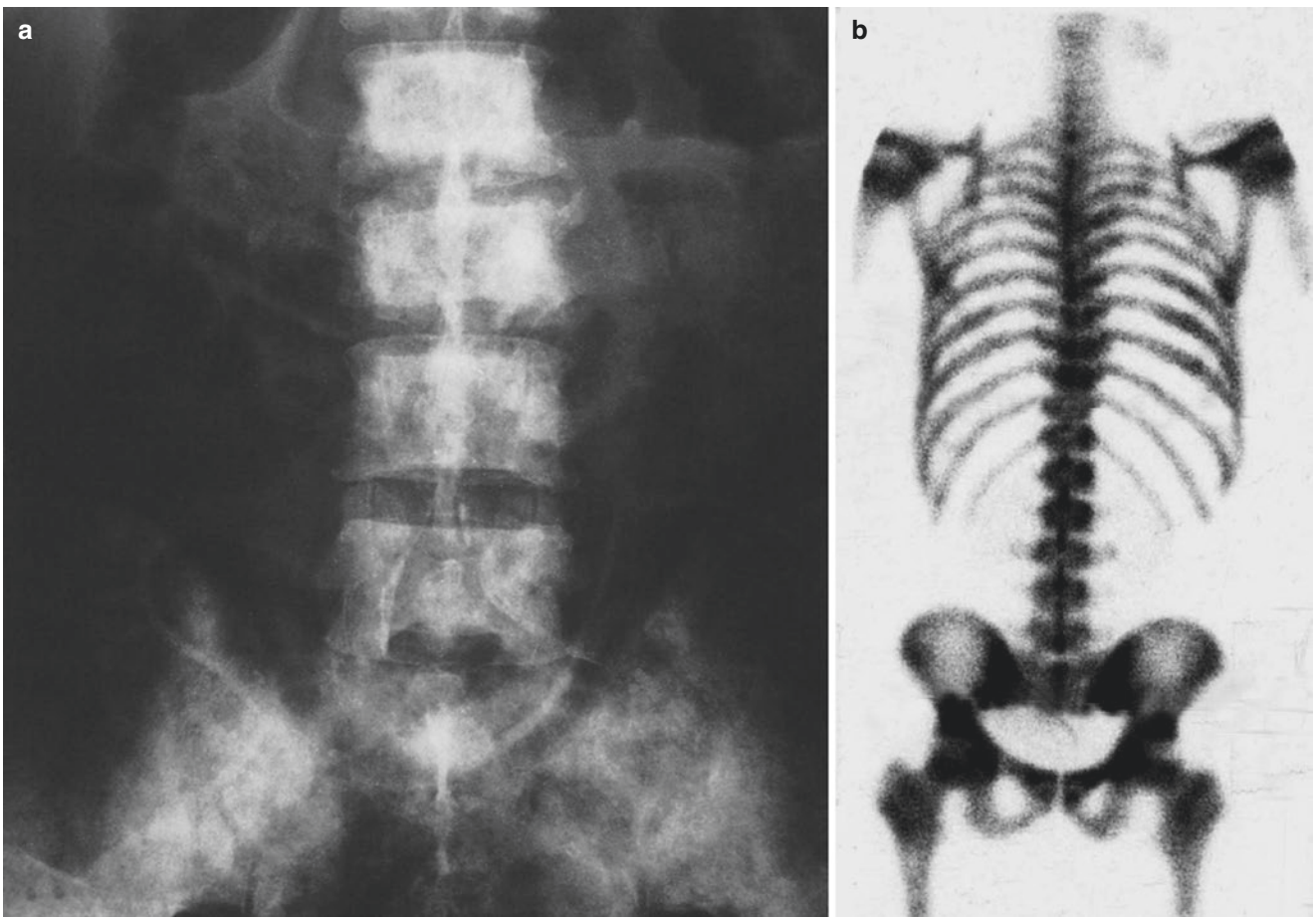

Fig. 17.5 Diffuse osteoblastic and "hot" metastases in prostatic carcinoma. (**a**) Anteroposterior radiograph of the lumbosacral region in a 75-year-old man with prostate cancer metastases shows widely disseminated patchy opacities involving the lumbar vertebrae, the sacrum, and the iliac bones. (**b**) Composite posterior scintigraph of the axial skeleton reveals a generalized increase in tracer uptake, producing the "superscan" appearance

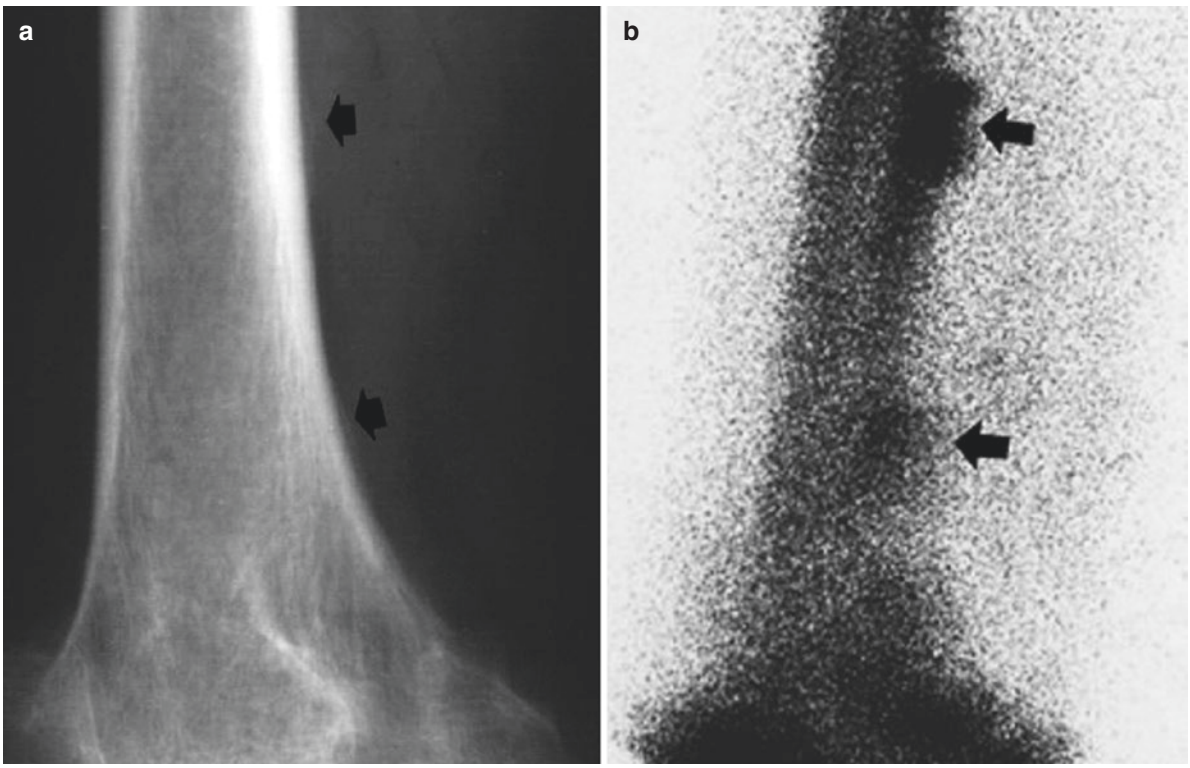

Fig. 17.6 Corticoperiosteal metastasis of bronchogenic carcinoma. (**a**) Lateral radiograph of the right distal femur in a 65-year-old male shows barely discernible periosteal thickening (*arrows*). (**b**) Lateral pinhole scintigraph reveals areas of intense tracer uptake localized to the distal femoral corticoperiosteum (*arrows*). Radiographic changes were discovered retrospectively

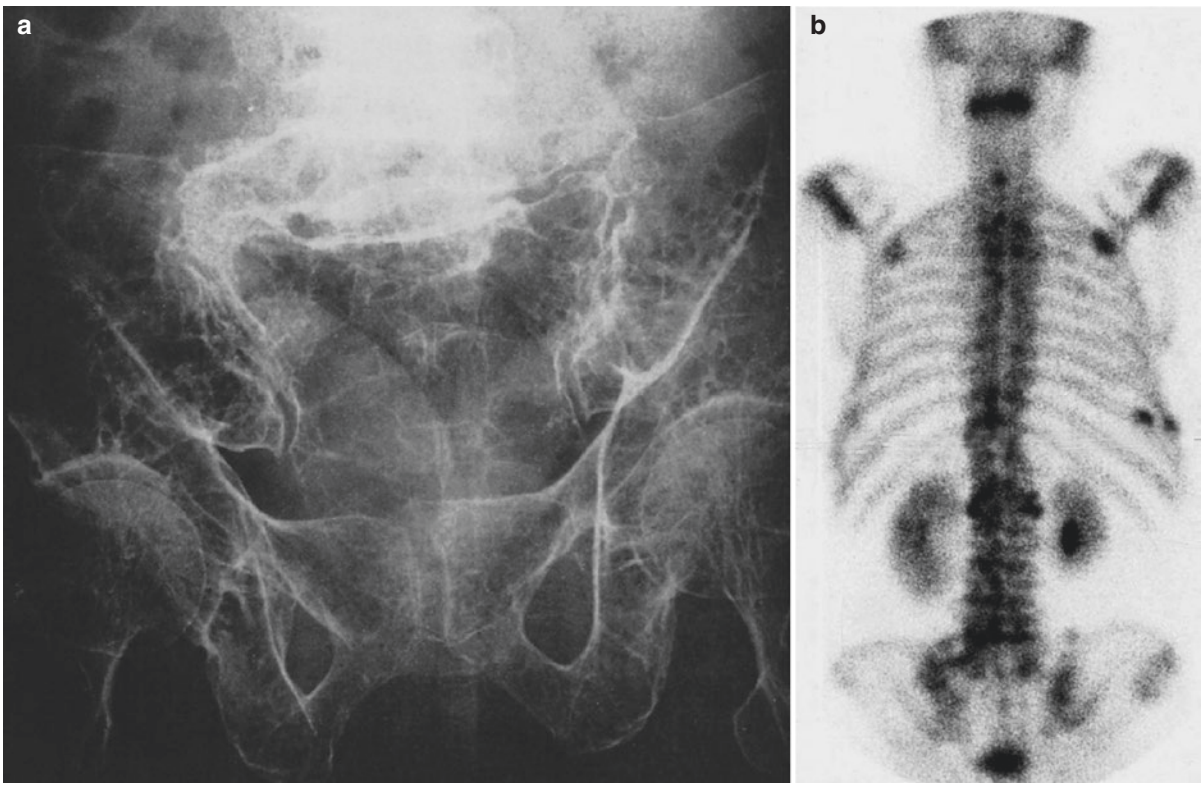

Fig. 17.7 Diffuse cystic and photopenic lesions in myelomatosis. (**a**) Anteroposterior radiograph of the pelvis in a 59-year-old woman shows extensive cystic bone destruction, producing a "soap bubble" appearance. (**b**) Composite posterior scintigraph of the axial skeleton and rib cage shows extensive, ill-defined photopenic defects in the spine, pelvis, and rib cage, producing a "pale" skeleton. The scattered "hot" spots in the rib cage and lumbar spine represent fractures complicating myelomatosis

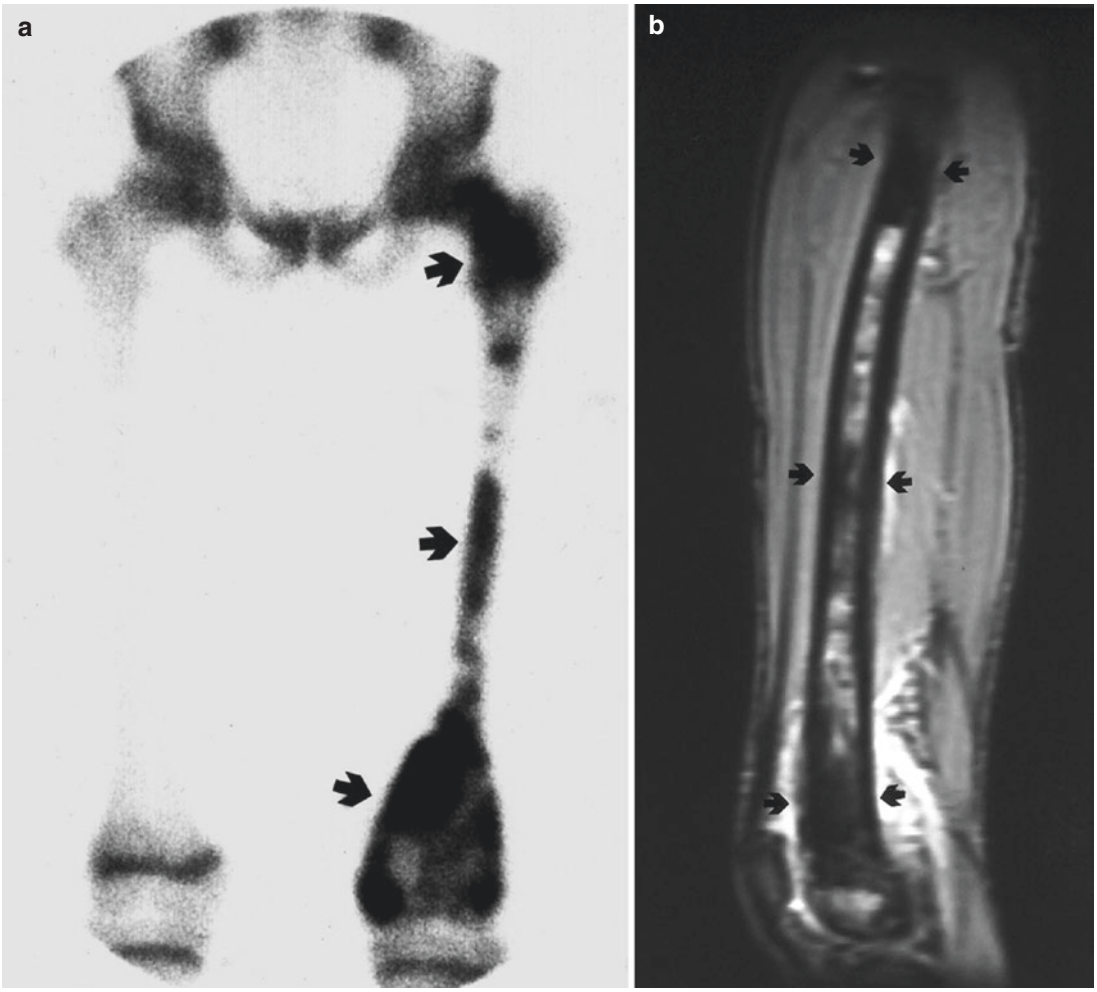

Fig. 17.8 Usefulness of scintigraphy in the detection of local intramedullary metastasis. (**a**) Composite anterior scintigraph of the pelvis and left femur in a 17-year-old man with a large primary osteosarcoma in the distal epimetaphysis reveals expansile, patchy intense tracer uptake (*bottom arrow*). In addition, two other "hot" areas are seen in the proximal and middle aspects (*middle and top arrows*), representing intramedullary metastases. (**b**) T1-weighted sagittal MRI reveals irregularly diminished signal intensity in the primary tumor (*bottom arrows*) as well as in the other two local metastases (*middle and top arrows*)

the same time (Fig. 17.14) or simultaneous mixed-type metastasis in the same bone (Fig. 17.15).

The multiplicity is a distinctive feature of metastasis. Indeed, the diagnosis becomes likelier if lesions are scattered randomly with the heavier involvement of the bones containing active hematopoietic marrow (Fig. 17.16). Metastases are called the "superscan" when diffuse and extensive (Fig. 17.17). Cranial spread of carcinoma may be considered as a modified expression of widespread metastasis that is not yet systemic. The number of bone metastases may vary from a few to numerous and even innumerable, and the scintigraphic expression may be either "hot" or "cold." Radiographic changes are predominantly osteolytic, mixed, or osteoblastic. Figure 17.18 demonstrates innumerable radiographically geographic and scintigraphically photopenic cranial metastases from esophageal carcinoma, and Fig. 17.19 is an example of scanty mixed-type cranial metastases from breast carcinoma.

As in certain primary bone tumors (McLean and Murray 1984; Goodgold et al. 1984; Hudson 1984), the characteristics of metastasis can be analyzed scintigraphically by the pinhole technique (Bahk et al. 1987). As predicted by

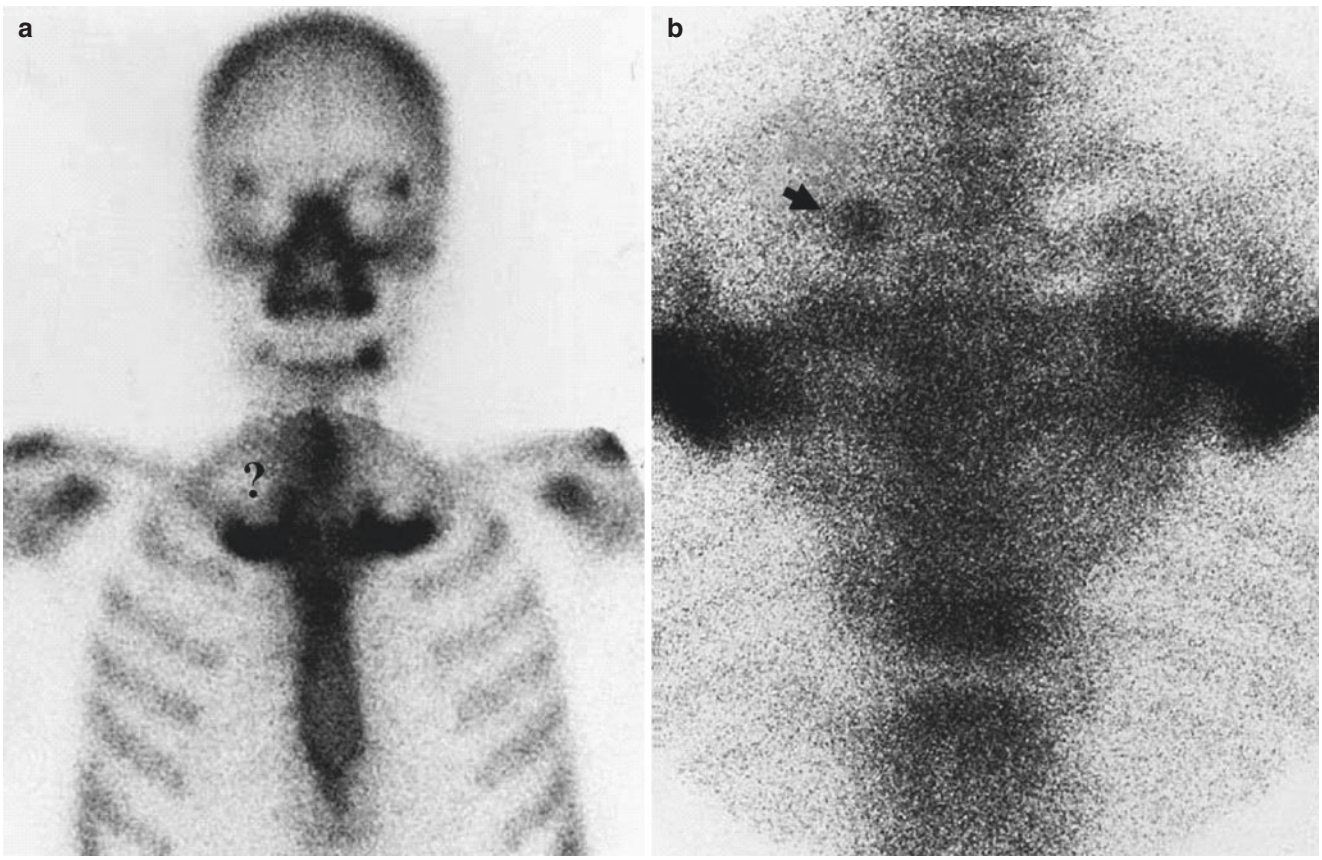

Fig. 17.9 Effect of pinhole scan. (**a**) Anterior planar scan of the upper chest shows suspicious tracer uptake in the right upper paravertebral region (*?*). (**b**) Pinhole scan distinctly demonstrates metastasis (*arrow*). Prominent tracer uptake in the sternocostoclavicular joints is a physiological finding

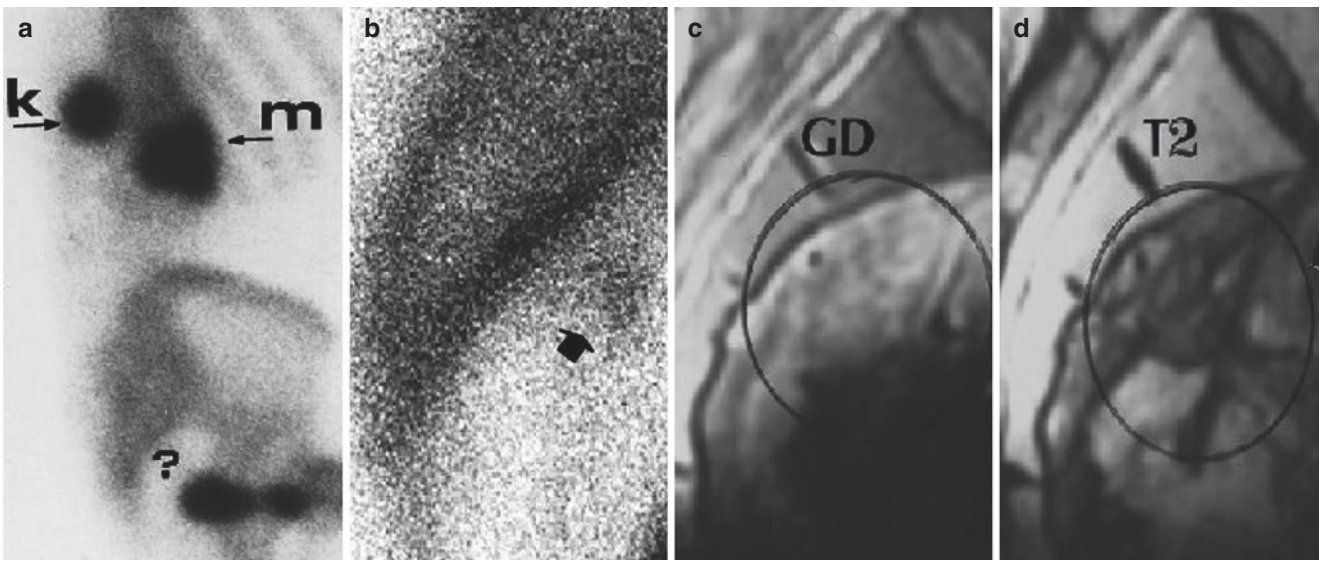

Fig. 17.10 Enhanced lesion detectability of pinhole scan. (**a**) Lateral planar scintigram of the sacrum taken as a part of metastasis series following colectomy for rectal carcinoma in a 42-year-old male shows no abnormal finding (*?*). *k* and *m* denote kidney and metastasis to the spine, respectively. (**b**) Lateral pinhole scintigram portrays increased uptake in the presacral recurrence (*arrow*). (**c**) Gadolinium-enhanced sagittal MRI reveals an area of high signal intensity in the upper presacral soft-tissue metastasis (*circle*). (**d**) T2-weighted sagittal MRI shows low signal intensity (*circle*)

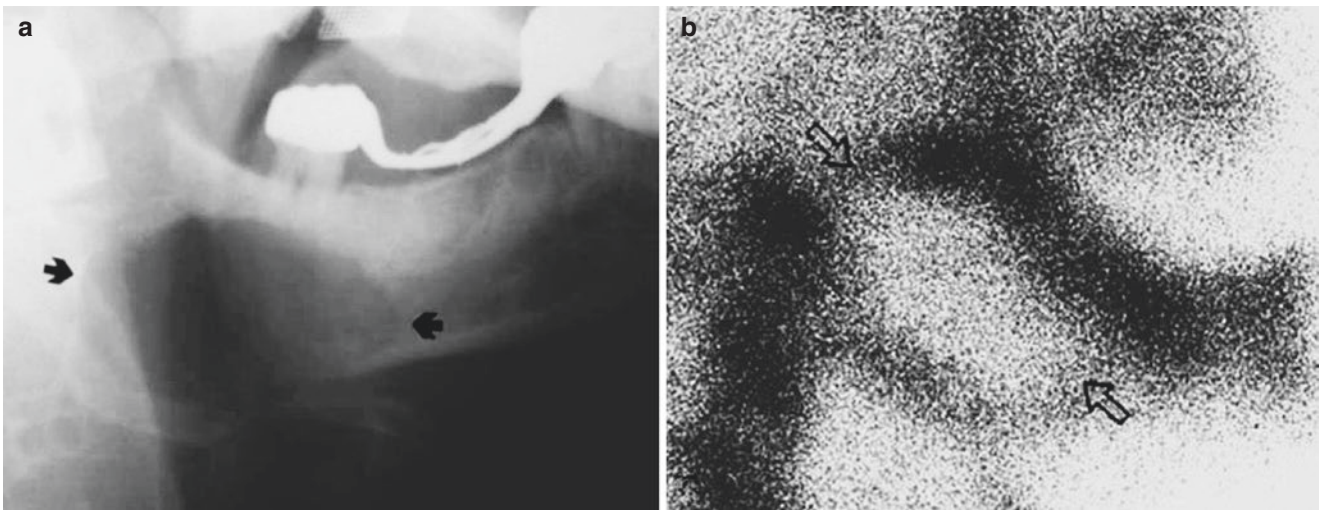

Fig. 17.11 Photopenic metastasis of renal carcinoma. (**a**) Lateral radiograph of the right mandible in a 61-year-old man shows a large osteolytic lesion (*arrows*). (**b**) Lateral pinhole scintigraph reveals typical photopenic presentation of renal cell carcinoma metastasis (*open arrows*)

McKillop (1987), it is not uncommon that pinhole scintigraphy depicts a photopenic component within apparently "hot" lesions shown on an ordinary scintigraph, giving rise to a ringlike or picture frame-like appearance. Pathologically, photopenia is related to osteonecrosis, hypovascularity, and aggressive invasion and is typically seen in metastases from carcinoma of the lung (Fig. 17.20a), breast (Fig. 17.20b), stomach, and kidney. The "ring" may be single or double and simple or signet shaped. Conversely, the pinhole scan occasionally discloses septum-like or mottled areas of tracer uptake within photopenic metastases. The bone metastasis from follicular thyroid carcinoma is a typical example (Kim et al. 1993) (Fig. 17.21). As discussed above, photopenic changes are encountered more commonly in metastases from renal cell carcinoma and occasionally in those from carcinomas of the lung, stomach, breast, and head and neck.

Pinhole scintigraphy plays a decisive role in discriminating vertebral metastasis (Fig. 17.22) from infection (Fig. 17.23) and fracture (Fig. 17.24), all of which radiographically manifest as bone destruction (Bahk et al. 1987). Pinhole scanning is also extremely valuable in the staging of malignant tumors and searching for distant metastases since the entire skeleton can be scrutinized (Fig. 17.25). In the investigation of an early metastasis, a high index of suspicion and keen judgment cannot be overemphasized. However, trifling a lesion may appear at first scanning; it should not be dismissed at once but rather be closely followed up with great concern preferably in 3 months at first, particularly when the primary tumor has a strong proclivity toward early and high-rate bone metastasis (Tanaka et al. 1991). One notorious tumor of this kind is breast carcinoma. The case presented in Fig. 17.26 was a 47-year-old female patient with well-differentiated invasive ductal adenocarcinoma of the right breast with positive axillary nodes. The first follow-up scintigraph was taken 10 months after mastectomy. There was a tiny, ambiguous uptake in the lateral edge of the right 11th rib. The second follow-up was 8 months later and showed unmistakable metastasis. Fortunately, the lesion had remained solitary.

Direct invasion of local bone is another mode of metastasis. Well-known examples are Pancoast's tumor of the thoracic inlet (Fig. 17.27) and peripherally located lung carcinomas with contiguous invasion of the local rib (Fig. 17.28), rectal carcinoma with spread to the sacrum, and

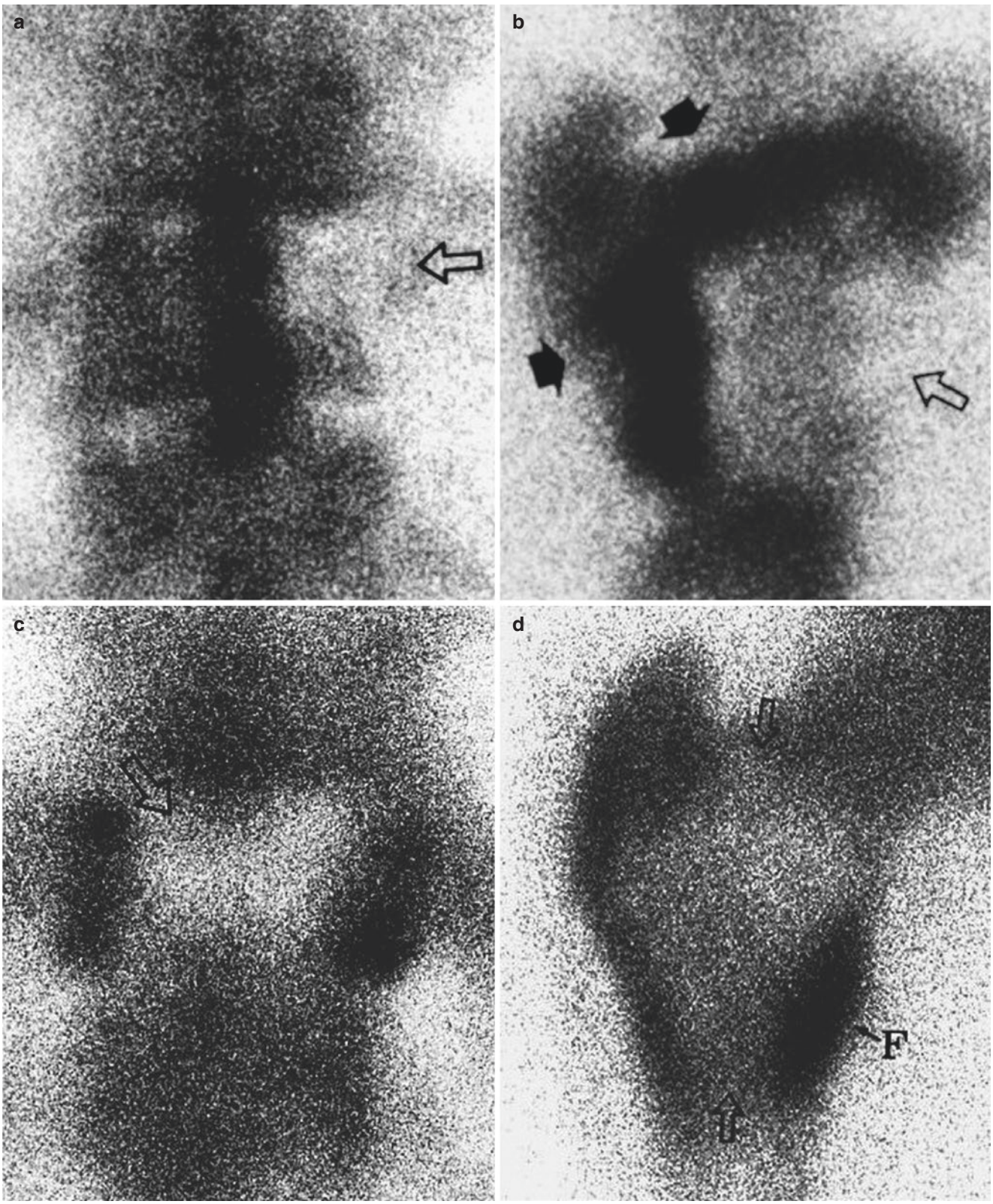

Fig. 17.12 Photopenic metastases from various primary carcinomas. Anterior pinhole scintigraphs of (**a**) L1 vertebra (*open arrow*), (**b**) manubrium sterni (*open arrow*), (**c**) T12 vertebra (*open arrow*), and (**d**) right femur show photopenic metastases (*open arrows*) from gastric carcinoma, breast carcinoma, laryngeal carcinoma, and cholangiocarcinoma, respectively (**d** *F* pathological fracture)

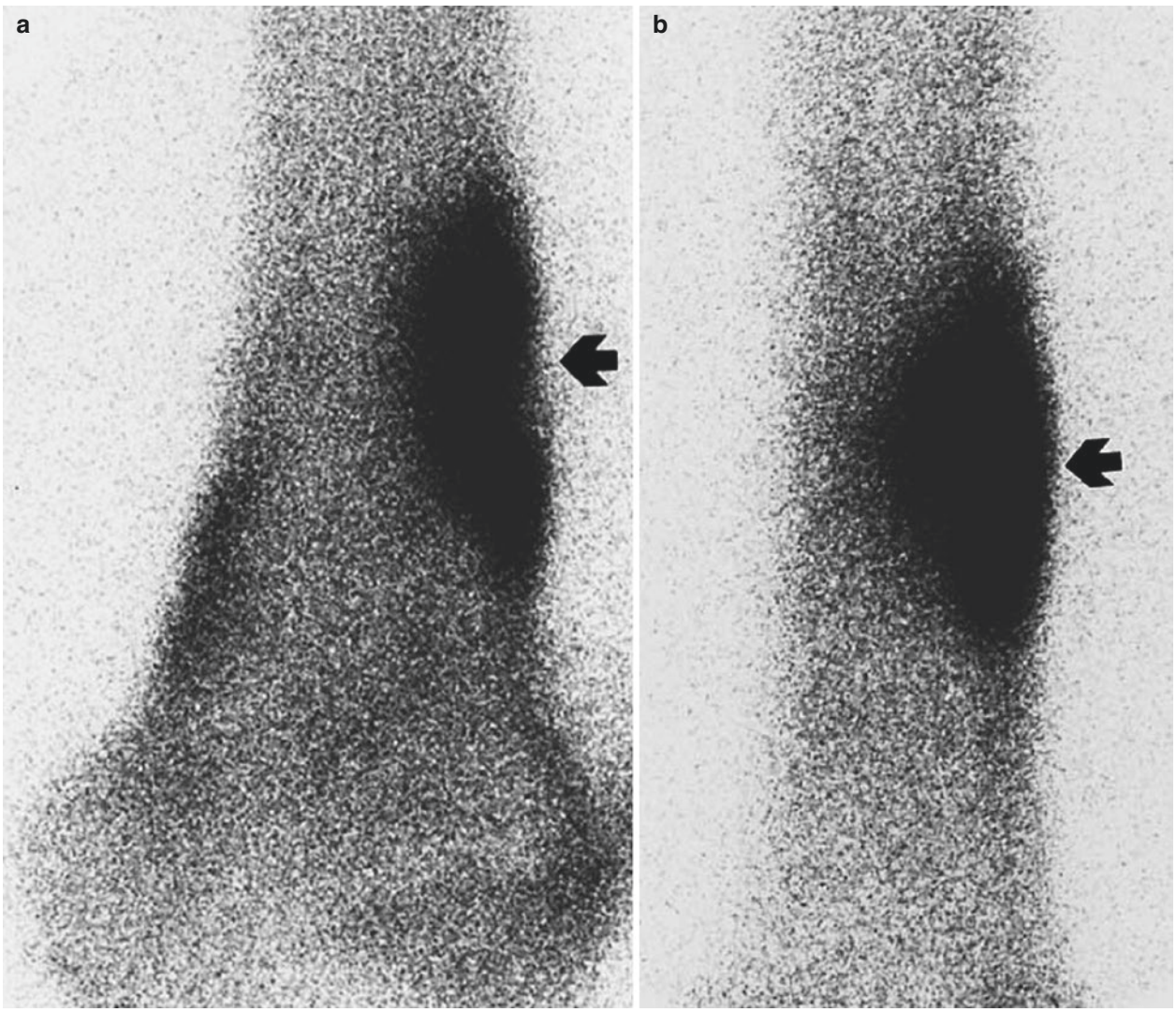

Fig. 17.13 Indistinguishable femoral cortical metastasis from carcinomas of the lung and kidney. (**a**) Anterior pinhole scan of the left distal femur in a 53-year-old female with lung cancer metastasis shows well-defined intracortical tracer uptake (*arrow*). (**b**) Anterior pinhole scintigraph of the left distal femur in a 57-year-old female with renal cell carcinoma metastasis shows exactly the same intracortical uptake (*arrow*)

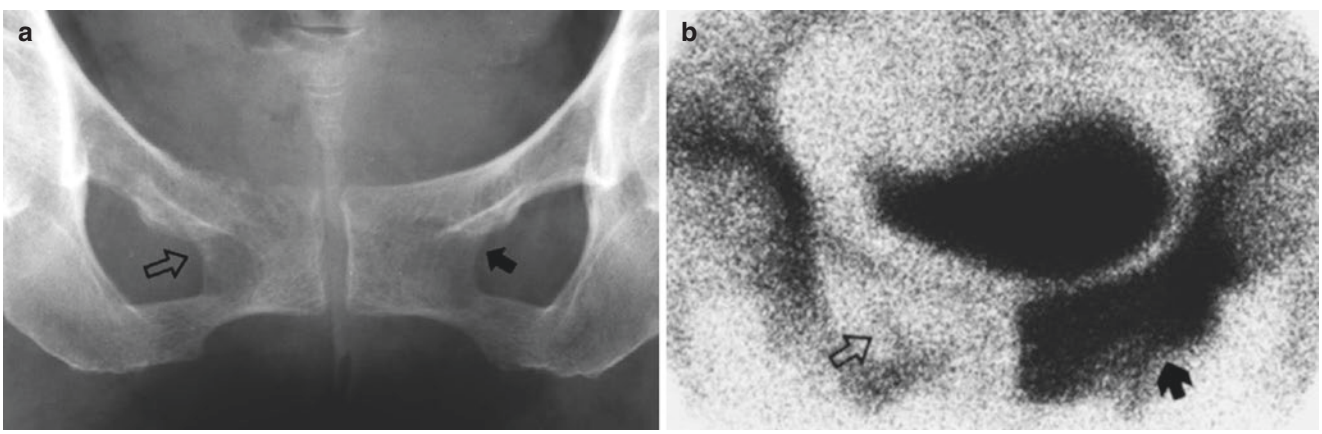

Fig. 17.14 Concurrence of photopenic metastasis in one pubic bone and photodense metastasis in the other pubic bone from gastric carcinoma. (**a**) Anteroposterior radiograph of the pubis in a 64-year-old female shows geographic osteolytic metastases in the right and left pubic bones (*arrows*). (**b**) Anterior pinhole scintigraph, however, reveals a photon defect in the right pubic bone (*open arrow*) and intense uptake in the left pubic bone (*solid arrow*)

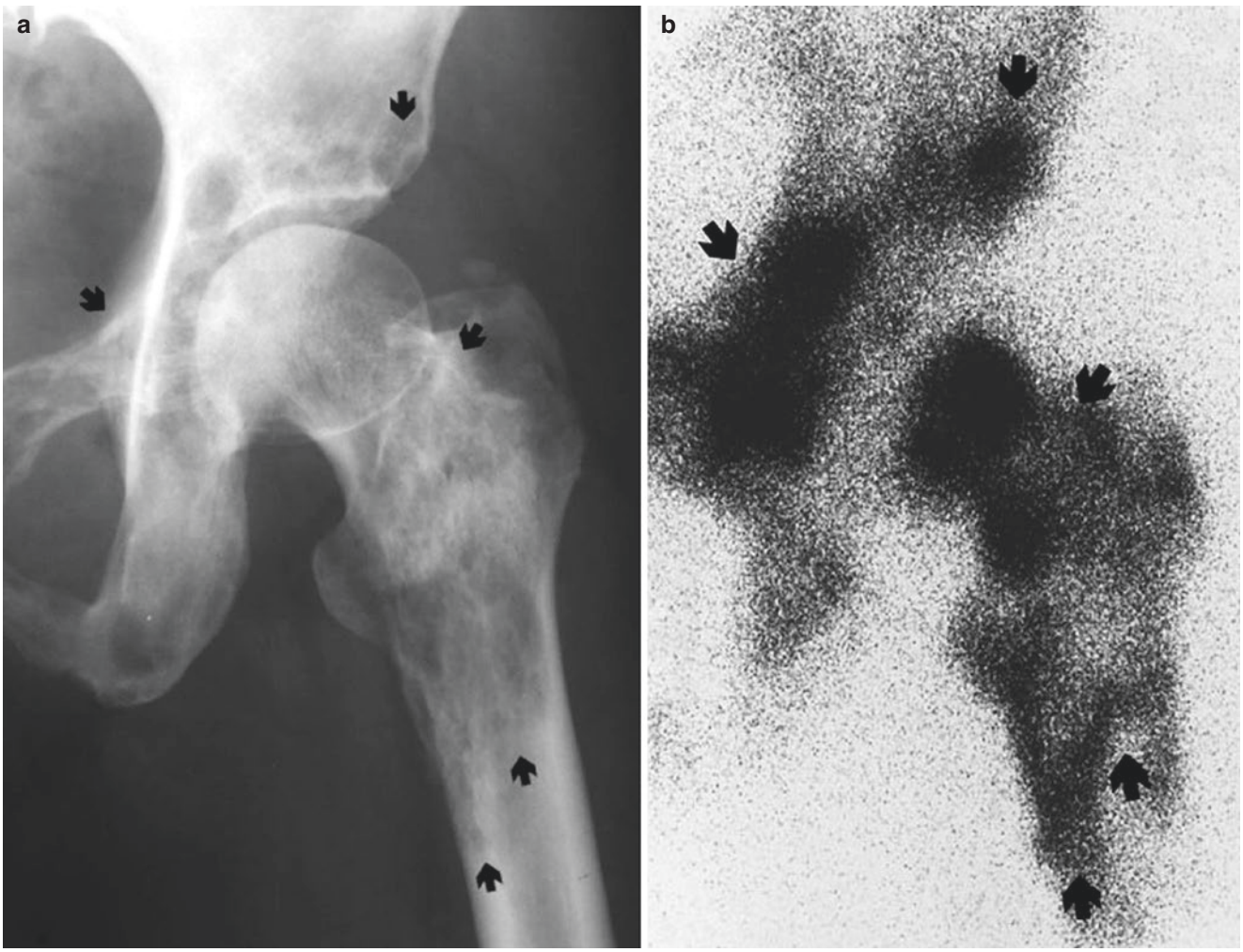

Fig. 17.15 Mixed metastasis from breast carcinoma. (**a**) Anteroposterior radiograph of the left hip and proximal femur in a 51-year-old female with breast carcinoma metastases shows irregular osteolytic and osteoblastic lesions (*arrows*). (**b**) Anterior pinhole scintigraph reveals a mixture of photopenic and photodense lesions (*arrows*). There is no uniform correlation between radiographic and scintigraphic changes

nasopharyngeal cancer with neighboring bone invasion (see "Nasopharyngeal Cancer" in Chap. 20). The direct rib invasion may (Fig. 17.27) or may not show tracer uptake (Fig. 17.28), requiring pinhole scintigraphy for accurate diagnosis (Fig. 17.27). Pinhole scintigraphy is very useful for the separate delineation of individual metastatic lesions that are closely positioned on the planar scintigraph (Fig. 17.29).

Cortical bone metastases occur as the result of hematogenous dissemination of tumor cells from almost any kind of carcinoma (Coerkamp and Kroon 1988). Extended application of the pinhole technique by us to the analysis

Fig. 17.16 Diffuse metastasis in hematopoietically active marrows. Posterior whole-body scintigraph in a 56-year-old man with gastric carcinoma metastases shows randomly spread tracer uptake with heavier involvement of the axial skeleton

Fig. 17.17 The "superscan" sign produced by extensive skeletal metastases. Anterior whole-body scintigraph in a 59-year-old female with breast carcinoma metastases shows generalized skeletal uptake involving from the skull through the axis to the appendicular bones

of long-bone metastases has been shown to be highly rewarding. Indeed, pinhole scanning distinguishes selective involvement of the cortex (Fig. 17.30), periosteum (Fig. 17.6), endosteum (Fig. 17.31), panosteum or all bone layers (Fig. 17.32), and medullary space (Fig. 17.33). In contrast to the absolute high prevalence of axial bone involvement, metastases are extremely rare in the bones of the hands and feet (Asthana et al. 2001; Bahk et al. 2006) (Fig. 17.34) and uncommon in the patella (Fig. 17.35) and mandible (Fig. 17.11).

The last but not least important use of bone scintigraphy in skeletal metastases is intra- and posttherapeutic follow-up (Gabuniia et al. 1989; Cook and Fogelman 2001). Pinhole scanning is particularly useful in this situation since anatomy and pathology are appreciated in greater detail. This examination efficiently and reliably portrays, first, treatment-naive metastasis (Fig. 17.36a), the flare phenomenon (Fig. 17.36b), and, finally, the cured state (Fig. 17.36c) after adjuvant chemotherapy or external irradiation. The flare is a transient increase in the intensity of bone uptake during treatment, usually chemotherapy, with subsequent recovery. In one recent series, 24.4% of 33 patients who received chemotherapy for non-small cell lung carcinoma showed the flare phenomenon (Lemieux et al. 2002).

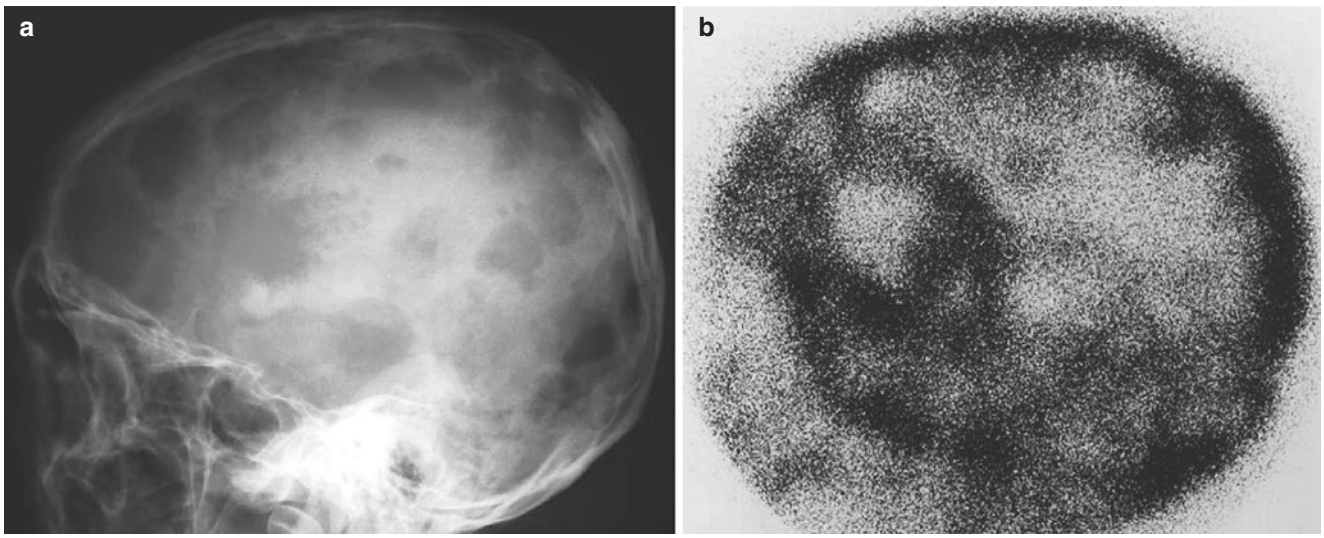

Fig. 17.18 Multiple bubbly cranial metastases from esophageal carcinoma. (**a**) Lateral radiograph of the skull in a 58-year-old male with esophageal carcinoma shows multiple round geographic lesions. (**b**) Lateral pinhole scintigraph reveals numerous photon defects with peripheral tracer uptake corresponding to lytic lesions

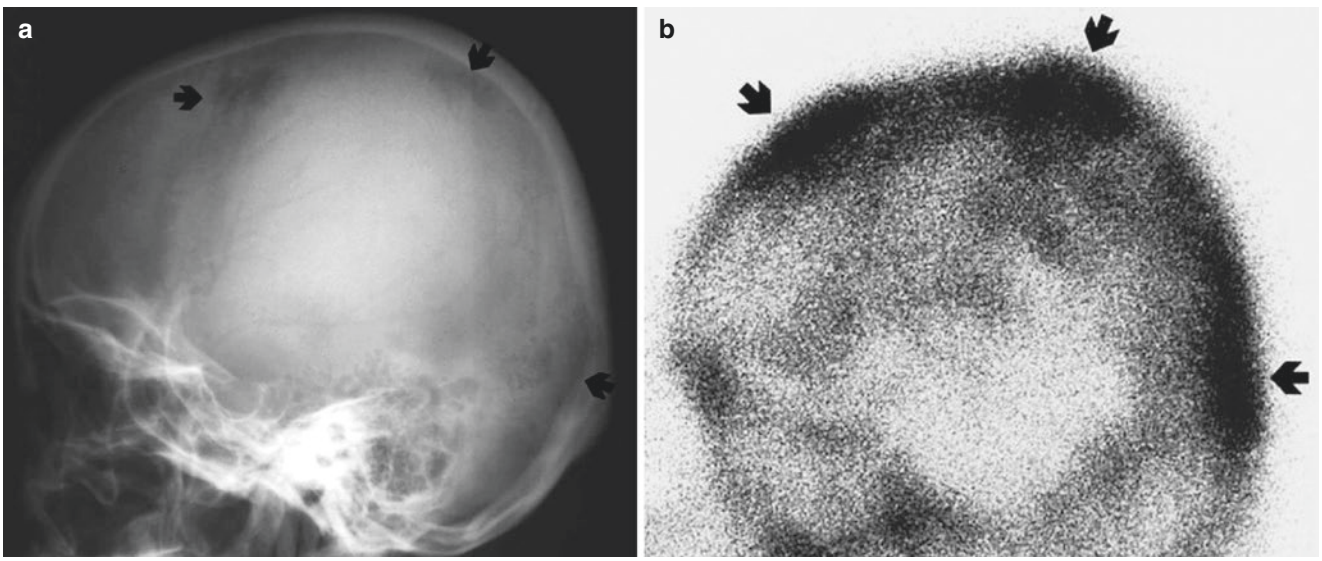

Fig. 17.19 Mixed-type cranial metastases from breast carcinoma. (**a**) Lateral radiograph of the skull in a 39-year-old female with breast carcinoma shows coexistence of patchy lysis and osteoblastic lesions (*arrows*). (**b**) Lateral pinhole scintigraph reveals patchy tracer uptake in lytic lesions (*arrows*) and less intense uptake in blastic lesions

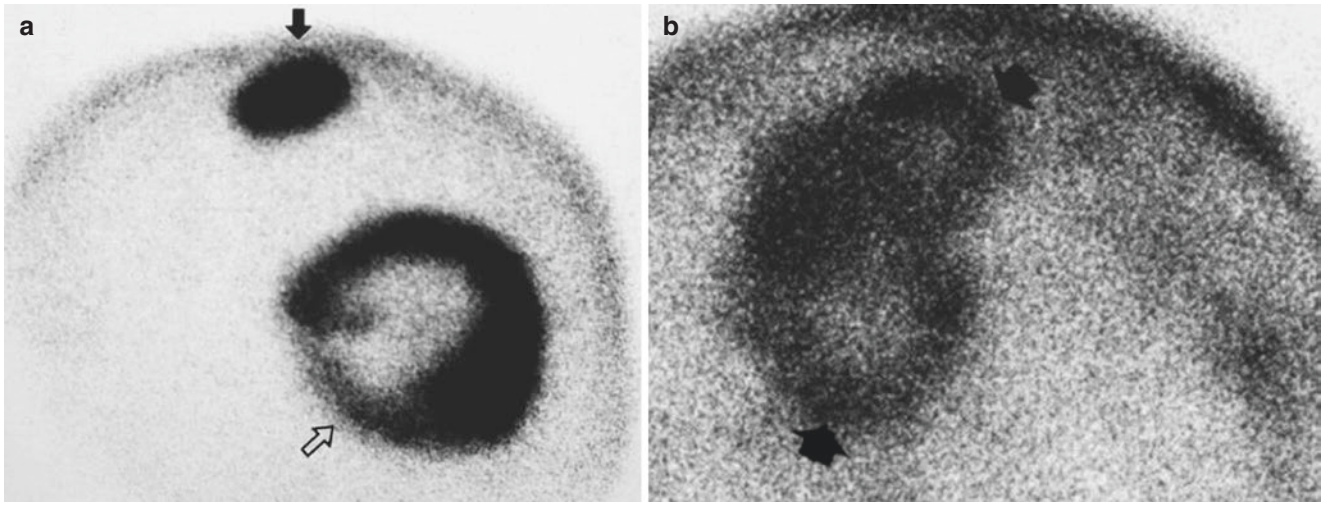

Fig. 17.20 Ringlike cranial metastasis from lung and breast carcinomas. (**a**) Lateral pinhole scintigraph of the skull in a 49-year-old female with lung carcinoma shows a ringlike metastasis (*open arrow*). A smaller daughter lesion is seen in the vertex (*solid arrow*). (**b**) Oblique pinhole scintigraph of the skull in a 37-year-old female with breast carcinoma shows a twin ringlike metastasis in the posterior parietal bone (*arrows*)

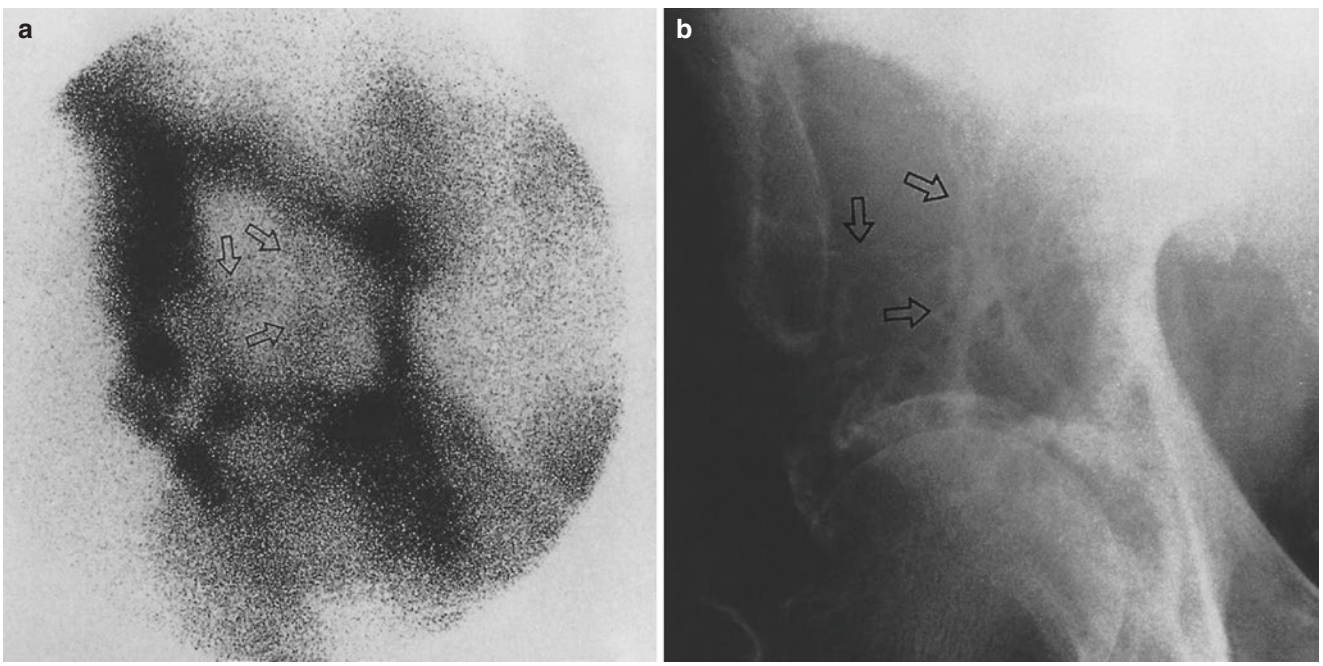

Fig. 17.21 Septated photopenic metastasis in follicular thyroid carcinoma. (**a**) Anterior pinhole scintigraph of the right innominate bone reveals a large, irregular photopenic defect surrounded by intense tracer uptake. Also linear tracer uptake can be seen within the defect, representing "septation" (*open arrows*). (**b**) Anteroposterior radiograph demonstrates a large area of bone destruction with "septation" (*open arrows*)

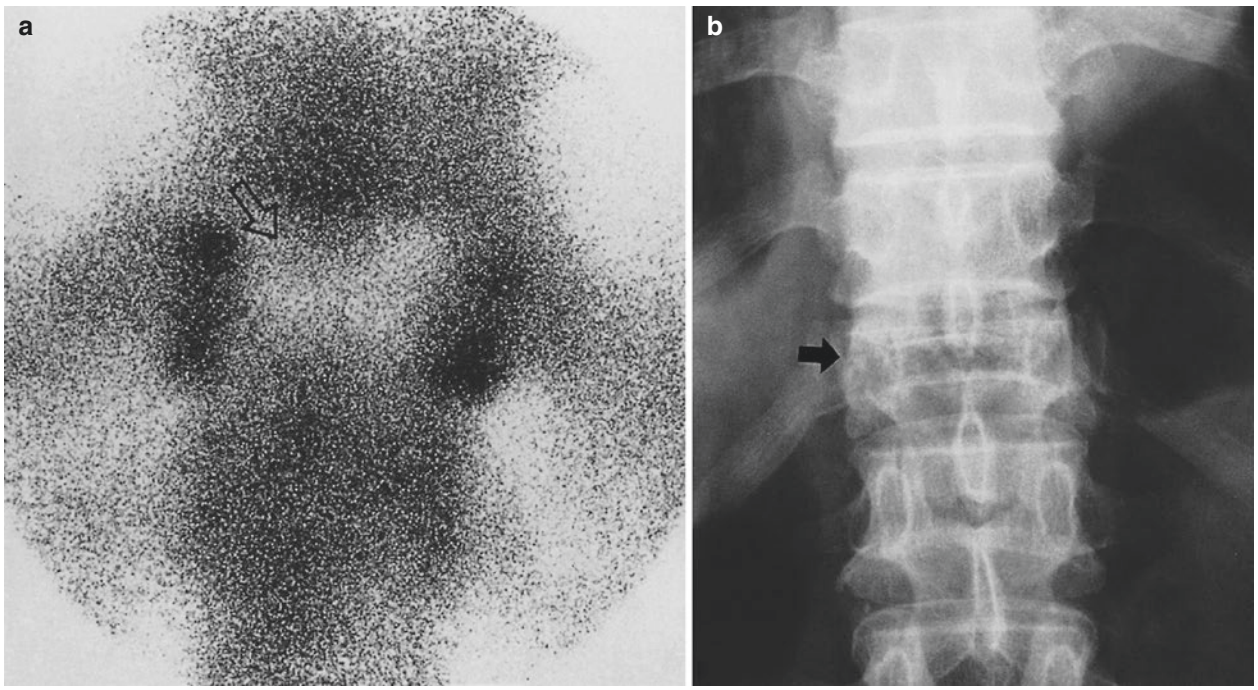

Fig. 17.22 Photopenic metastasis from laryngeal carcinoma. (**a**) Posterior pinhole scintigraph of the T12 vertebra in a 58-year-old man with squamous cell carcinoma of the larynx shows a large photopenic defect involving the whole vertebral body (*arrow*). The defect is bilaterally sided by the pedicles which are spared and concentrate tracer intensely. (**b**) Anteroposterior radiograph reveals osteolysis with moderate collapse. The pedicles are preserved (*arrow*)

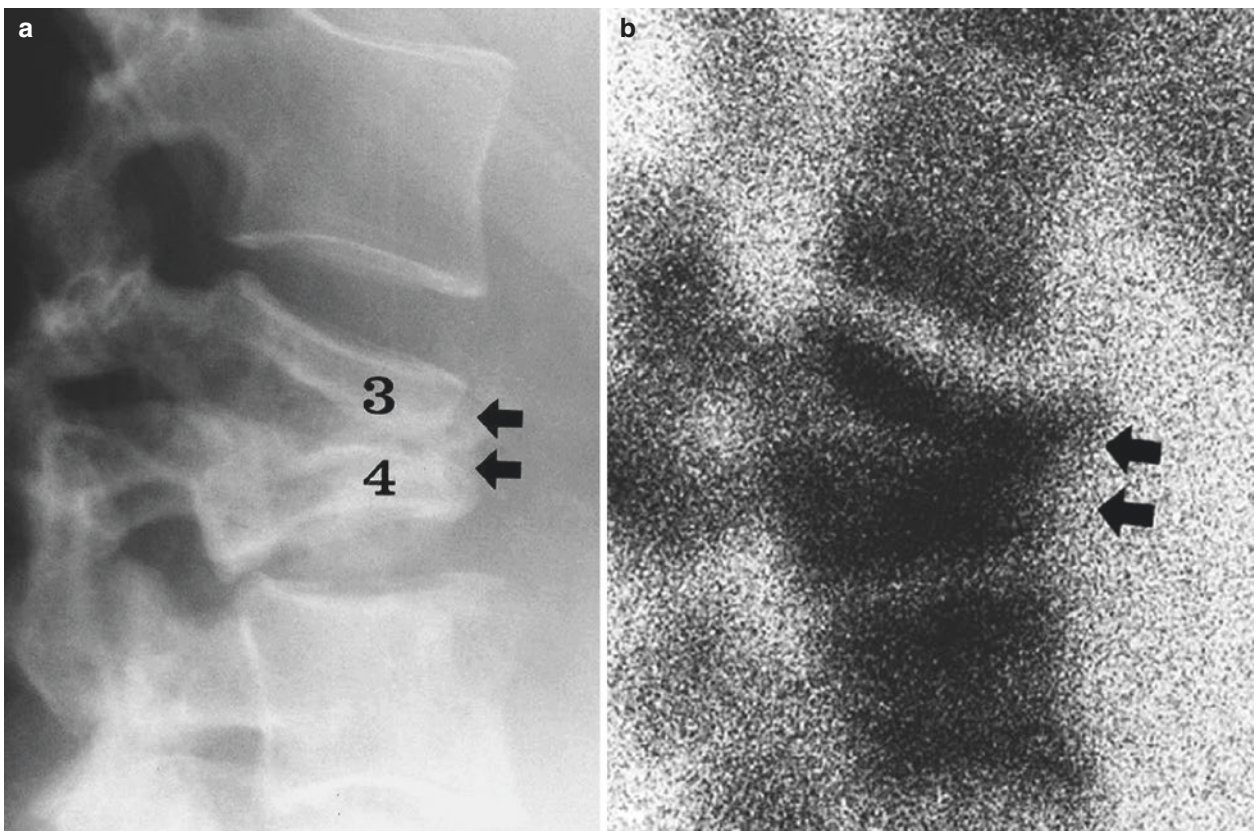

Fig. 17.23 Pinhole scan of tuberculous spondylitis. (**a**) Lateral radiograph of L3 and L4 in a 29-year-old female with advanced tuberculosis shows vertebral collapse with narrowed disk space (*arrows*). (**b**) Lateral pinhole scintigraph reveals intense tracer uptake in collapsed vertebrae with narrowed disk space (*arrows*)

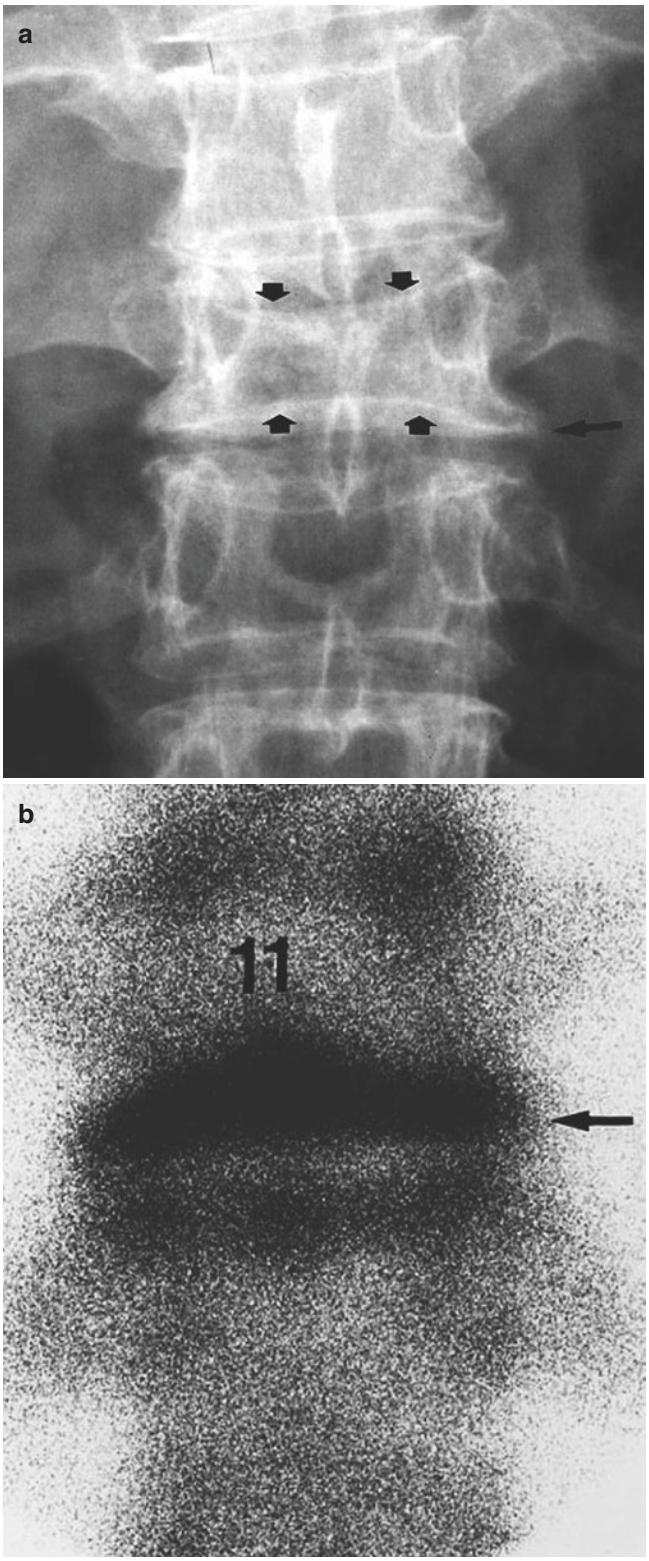

Fig. 17.24 Pinhole scan of spinal compression fracture. (**a**) Anteroposterior radiograph of T11 in a 64-year-old female shows compression of both the upper and lower endplates (*arrows*). There is preexisting hypertrophic change with spurs (*large arrow*). (**b**) Anterior pinhole scintigraph, however, reveals tracer uptake only in the lower endplate and not in the upper endplate indicating that the fresh fracture is in the lower endplate and that the upper endplate compression is due to an ancient fracture

Fig. 17.25 Simultaneous demonstration of metastasis and primary tumor site. Anterior whole-body scan in a 20-year-old male with osteosarcoma treated by right upper limb disarticulation (DA) shows a single metastasis in the skull (*arrow*)

17.1.1 Bone Marrow Scintigraphy in Metastasis

Cancer cells are carried to the bone marrow via the bloodstream and are anchored and implanted in the medullary sinusoidal arteries. Surviving tumor cells are facilitated to extravasate into the marrow space because blood flow is sluggish, the endothelium is loose, and the basement membrane is not present. Bone marrow metastases can occur without cortical involvement, for example, in breast carcinoma (Kamby et al. 1987). ^{99m}Tc-NCA95 bone marrow scintigraphy can sensitively and accurately detect metastases, which are visualized as photopenic lesions (Fig. 17.37a). This finding sharply contrasts with the photodense (increased uptake) manifestation on ^{99m}Tc-MDP scans (Fig. 17.37b). Approximately 90% of bone marrow metastases are blood borne, and, hence it is natural that bone marrow metastases

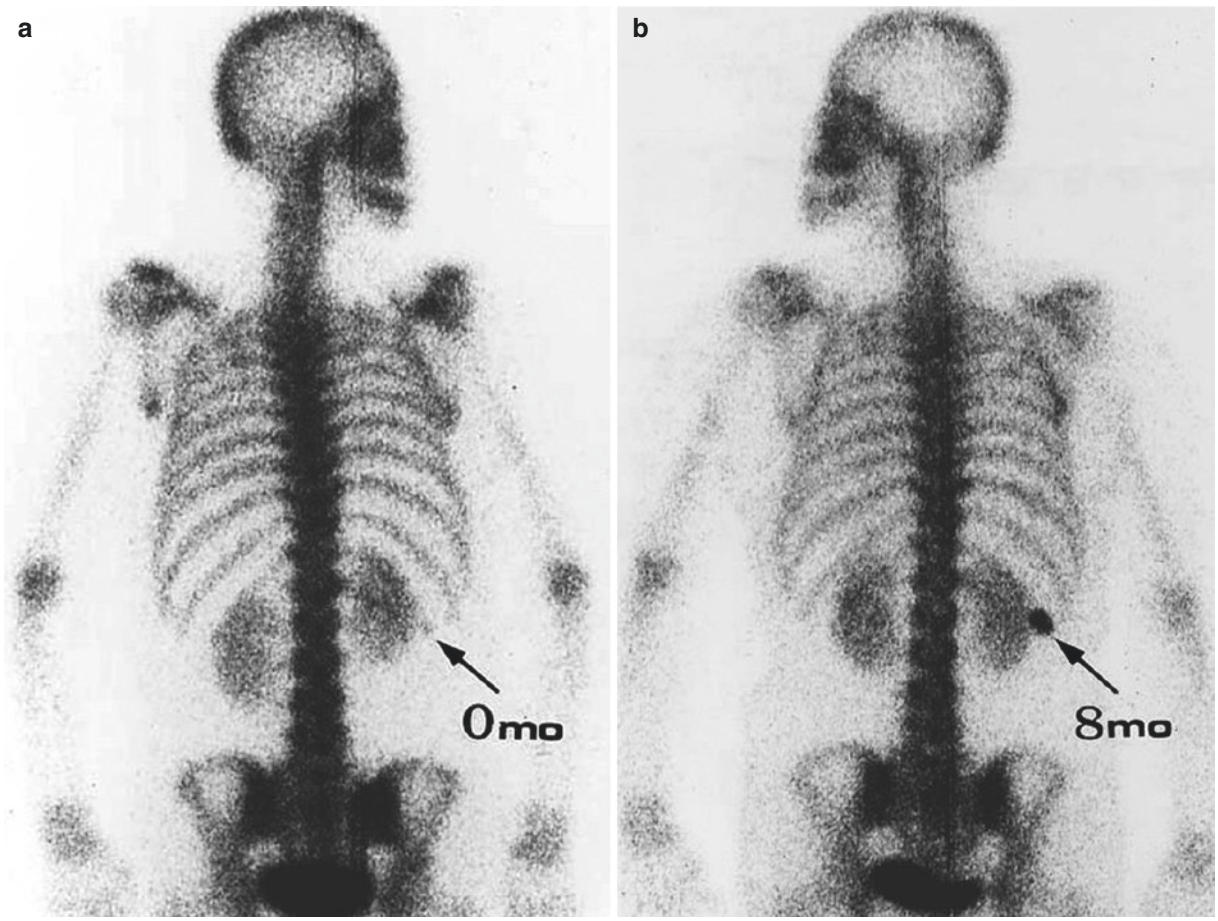

Fig. 17.26 High index of suspicion helps diagnose early metastasis. (**a**) Posterior planar scan of the axial skeleton in a 47-year-old female with breast carcinoma shows questionable uptake in the lateral edge of the right 12th rib (*arrow*). (**b**) Follow-up scan 8 months later reveals unmistakable metastasis (*arrow*)

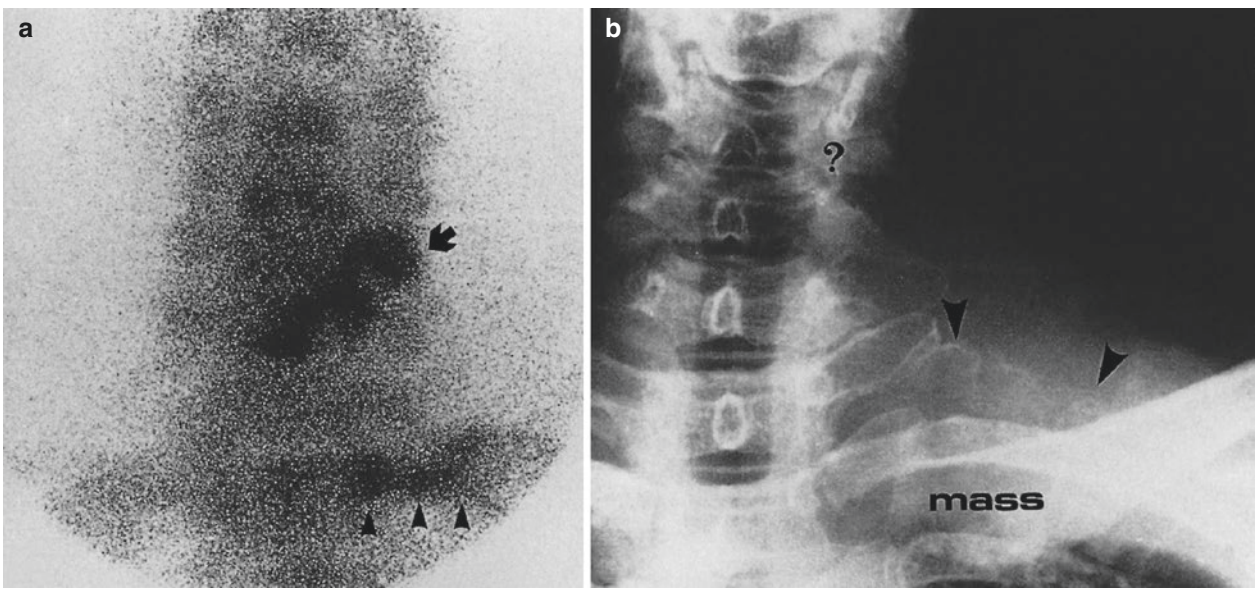

Fig. 17.27 Direct rib invasion by thoracic inlet (Pancoast's) tumor and incidental distant metastases. (**a**) Posterior pinhole scintigraph of the left thoracic inlet in a 50-year-old woman with Pancoast's tumor shows subtle tracer uptake in the first rib near the spine, indicating direct cancer invasion (*arrowheads*). Incidentally, the lower cervical spine shows patchy tracer uptake in the metastases (*arrow*). The scintigraph is printed with the right side on the left to match the radiograph. (**b**) Anteroposterior radiograph reveals lysis in the posterior first rib near the spine (*arrowheads*) and the primary tumor in the thoracic inlet (*mass*). The metastases in the lower cervical spine clearly shown by scintigraphy are not certain radiographically (*?*)

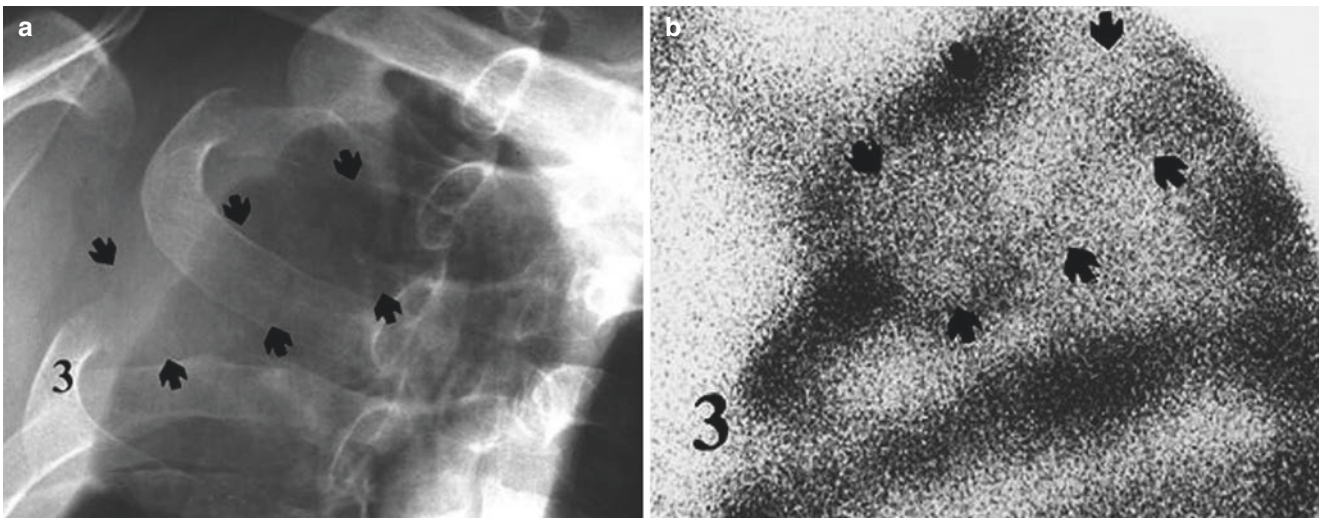

Fig. 17.28 Contiguous rib invasion by peripheral bronchogenic carcinoma. (**a**) Anteroposterior radiograph of the right upper chest in a 42-year-old male shows lysis of the posterior portion of the third rib (*arrows*). Tumor is not seen because of the high penetration technique. (**b**) Posterior pinhole scintigraph reveals concordant photon defect (*arrows*) with reactive rib uptake (*3*)

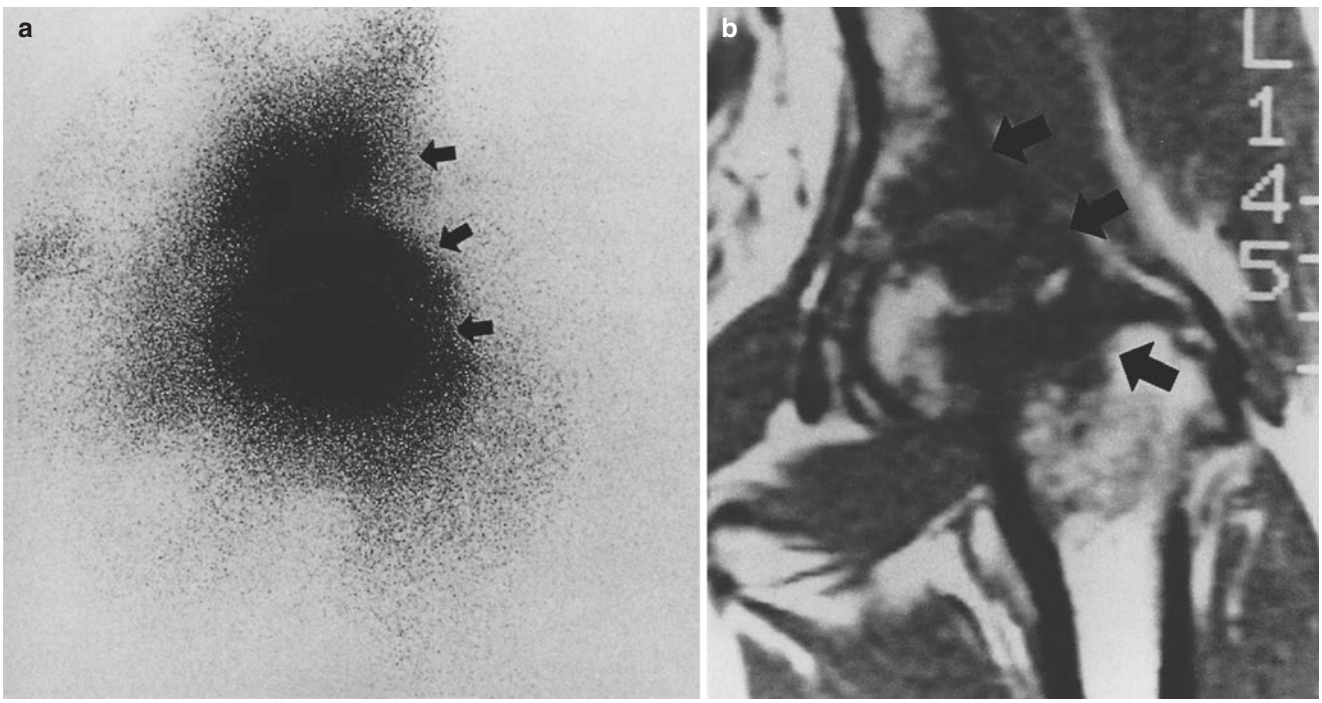

Fig. 17.29 Discreteness of the multiple individual lesions that are close to each other, a differential point in favor of metastasis. (**a**) Anterior pinhole scintigraph of the left hip in a 45-year-old woman with breast cancer shows discrete tracer uptake in the acetabulum (*top arrow*) and femoral head (*lower arrows*) across the clear joint, favoring the diagnosis of metastases at two different sites. The lesions were presented as a single pathology of the hip joint on ordinary scintigraph, raising the possibility of coxitis (not shown here). Also observe that the more intense tracer uptake occurs centrally in the tumor and the less intense uptake peripherally in the watershed. (**b**) T1-weighted coronal MRI shows decreased signal intensity in metastases in both the acetabulum (*top arrow*) and femoral head (*lower arrows*)

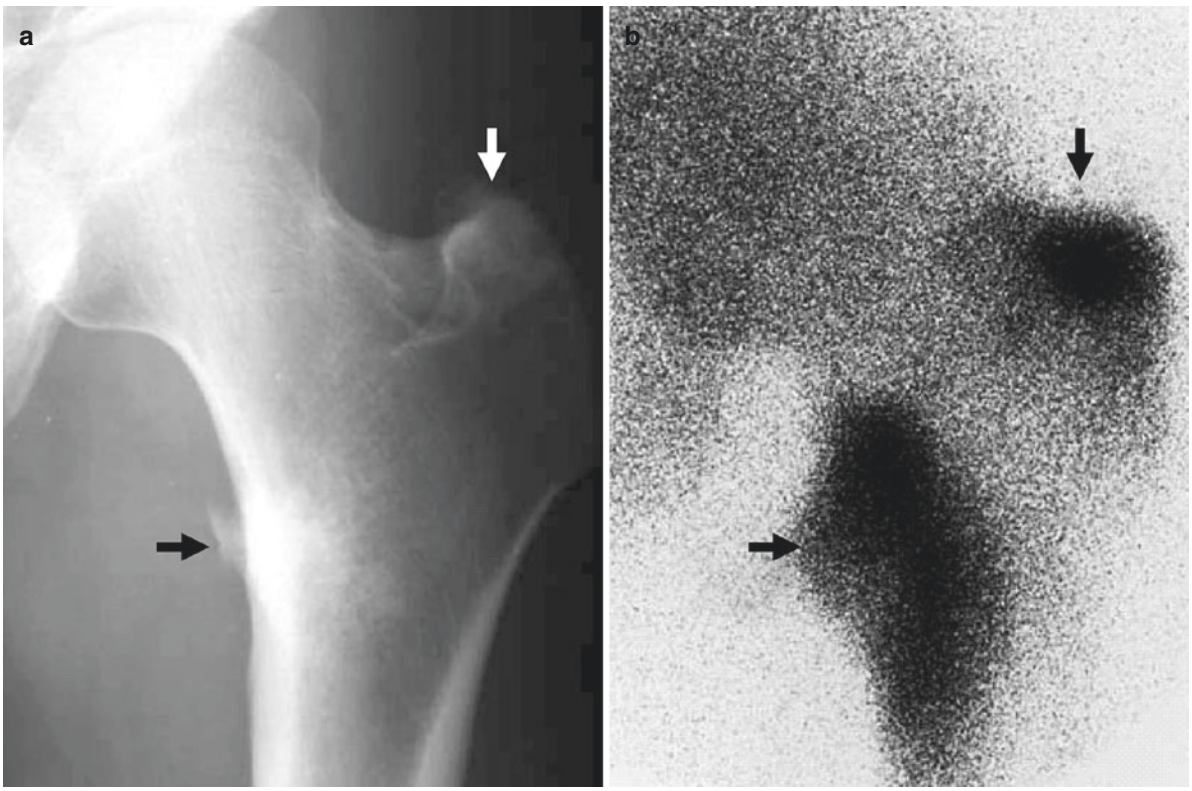

Fig. 17.30 Trochanteric metastasis. (**a**) Anteroposterior radiograph of the left proximal femur in a 26-year-old male with thymoma shows osteoblastic metastases to the greater and lesser trochanters (*arrows*). (**b**) Anterior pinhole scan reveals concordant tracer uptake (*arrows*)

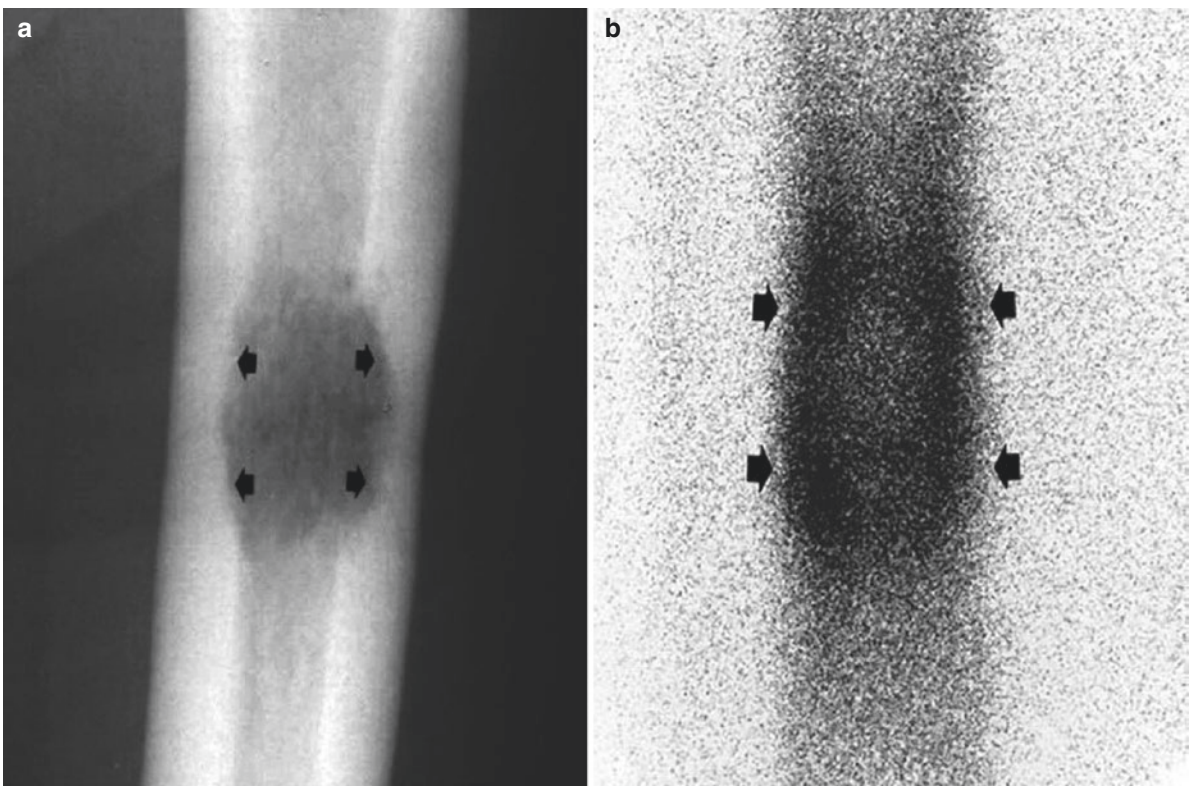

Fig. 17.31 Endosteal metastatic invasion. (**a**) Anterior pinhole scintigraph of the right femoral shaft in a 54-year-old male with pancreatic cancer metastasis shows increased tracer uptake localized to endosteums (arrows). (**b**) Anteroposterior radiograph reveals an expansive osteolytic lesion invading endosteums

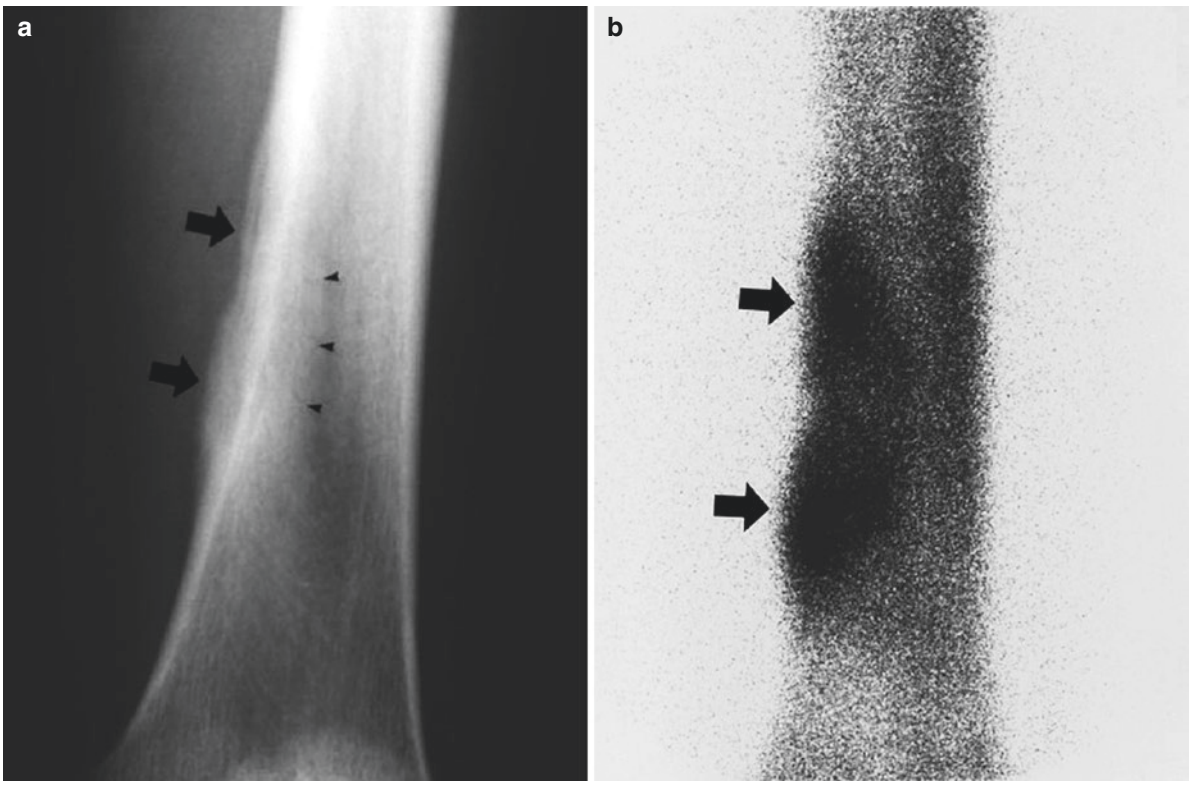

Fig. 17.32 Panosteal metastasis. (**a**) Anteroposterior radiograph of the left femoral shaft in a 47-year-old female with breast carcinoma shows diffuse thickening of the endosteum (*arrowheads*), periosteum (*arrows*), and cortex. (**b**) Anterior pinhole scintigraph reveals increased tracer uptake in all bone layers (*arrows*)

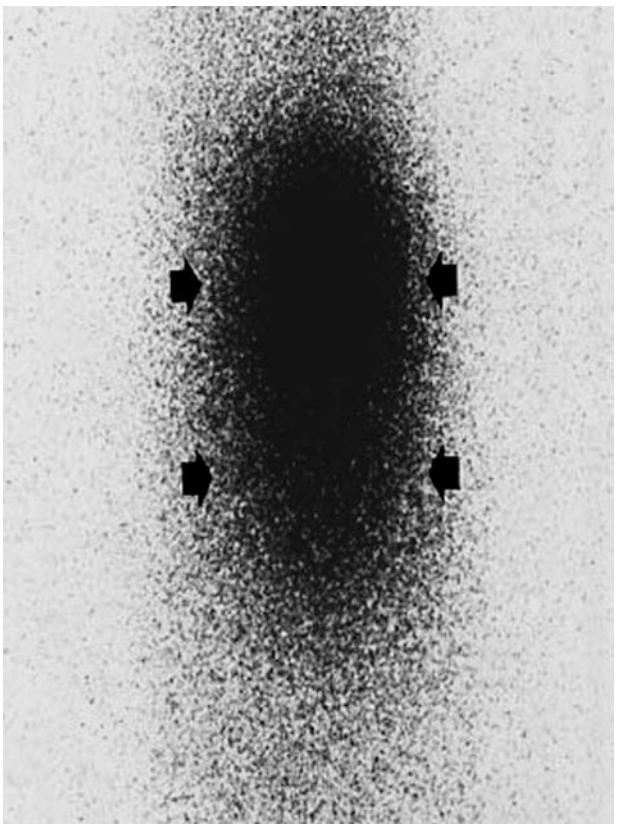

Fig. 17.33 Medullary metastasis. Anterior pinhole scintigraph of the right humeral shaft in a 64-year-old male with lung carcinoma shows fusiform tracer uptake within the medullary cavity (*arrows*)

Fig. 17.34 Multiple acrometastases. Dorsopalmar radiograph of the right hand shows prominent bony clubbing of all fingertips due to osteoblastic metastases from gastric adenocarcinoma

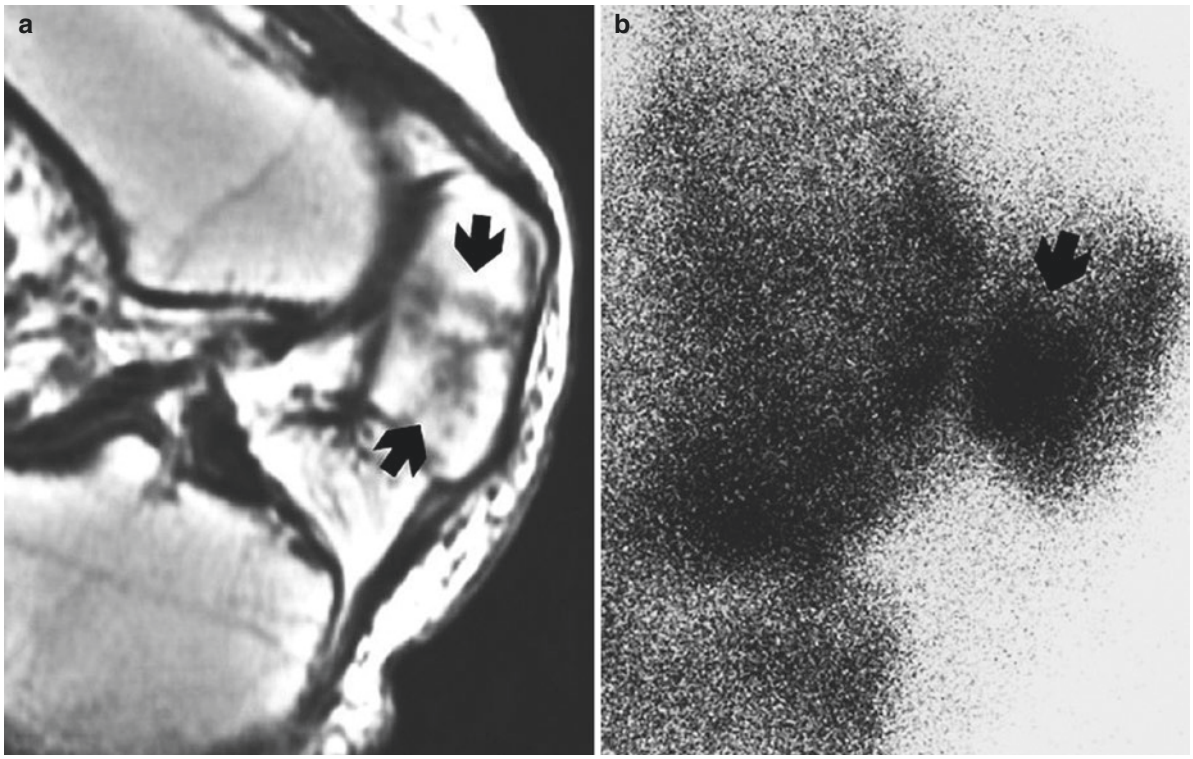

Fig. 17.35 Patellar metastasis. (**a**) Sagittal T1-weighted MRI of the right patella in a 57-year-old male with lung carcinoma shows irregular low signal in the lower half of the marrow space (*arrows*). (**b**) Lateral pinhole scan reveals concordant patchy uptake in the inferoposterior aspect of the patella (*arrow*)

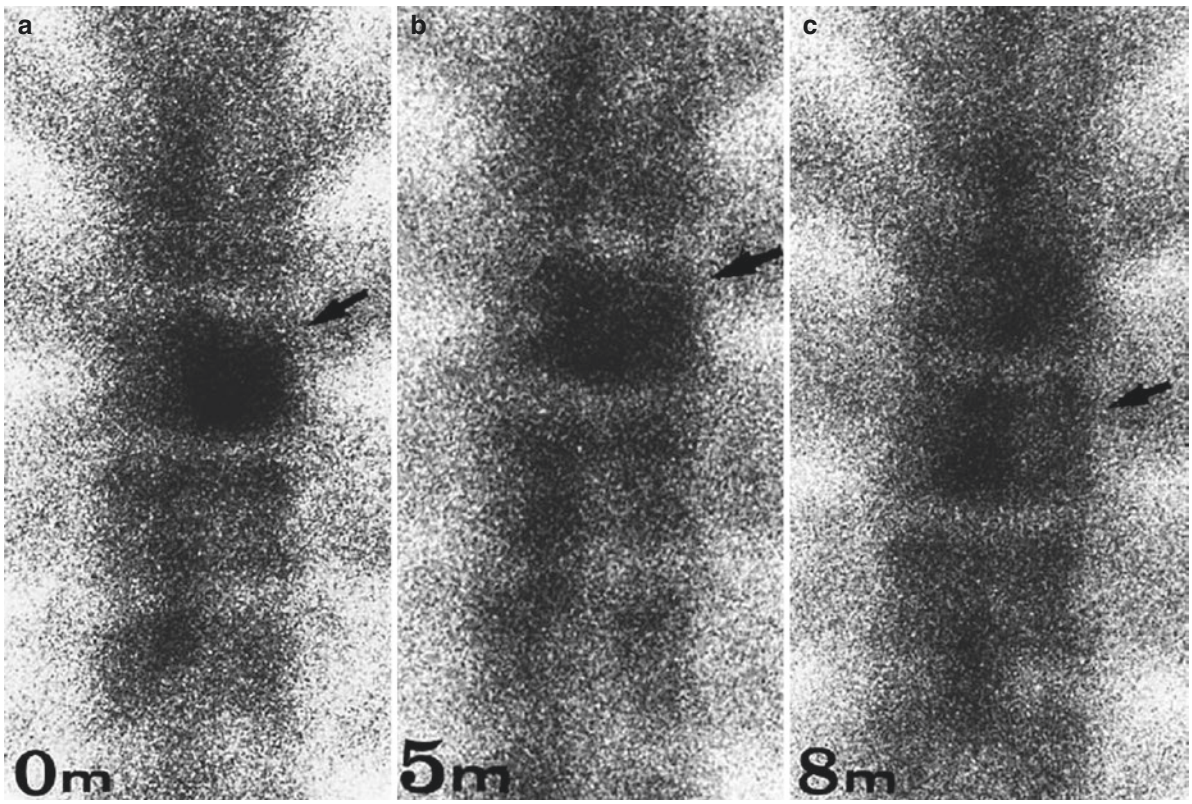

Fig. 17.36 Pre- and postadjuvant therapy evaluation of bone metastasis. (**a**) Initial pinhole scintigraph of the T7 vertebra in a 57-year-old female with breast carcinoma metastasis shows patchy uptake in therapy-naive metastasis (*arrow*). (**b**) First, postadjuvant chemotherapy scan taken 5 months later shows "flare uptake" (*arrow*). (**c**) Second, follow-up at 8 months shows no pathological tracer uptake (*arrow*)

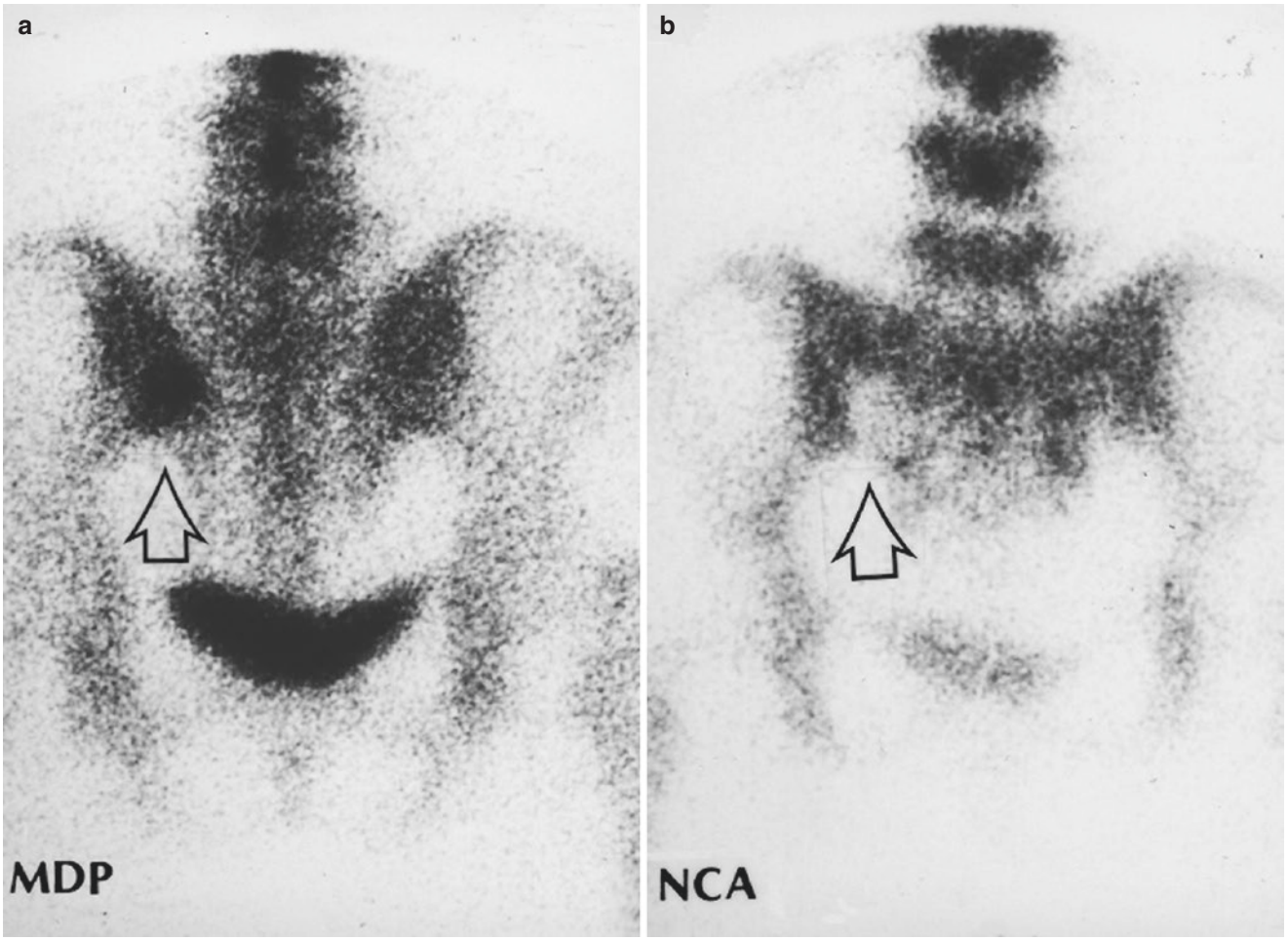

Fig. 17.37 Immunoscintigraphy of bone metastasis. (**a**) Posterior ^{99m}Tc-MDP bone scintigraph of the pelvis in a patient with metastasis from prostate carcinoma shows prominent tracer uptake in the left lower sacroiliac joint (*arrow*). (**b**) Posterior planar ^{99m}Tc-NCA95 immunoscintigraph reveals concordant photon defect (*open arrow*)

exist in the absence of affected bone (Fig. 17.38). The agents for bone marrow scanning are largely limited, including only ^{99m}Tc nanocolloid and ^{99m}Tc-labeled anti-nonspecific cross-reacting antigen (anti-NCA) 95.

Immunoscintigraphy has been shown to be a sensitive indicator of the presence and extent of malignant marrow infiltration (Reske et al. 1989; Duncker et al. 1990). It can distinguish malignancy from benignity in patients with an equivocal ^{99m}Tc-MDP bone scintigraphic change (Lee et al. 1995). The sensitivity and specificity were 100% and 79%, respectively. False-positives occur in degenerative arthritis of the spine, the marrow of which has been replaced with fat. If a marrow scan defect is found in concordance with a positive bone scan, radiography is mandatory to exclude benign conditions such as red marrow involution (Cooper et al. 1992), focal osteonecrosis (Haubold-Reuter et al. 1993), Paget's disease, and bone infarction (Yuasa et al. 1991).

Duncker et al. (1990) assessed the usefulness of immunoscintigraphy in patients with breast cancer suspected of having bone metastasis, finding marrow defects in 25 of 32 patients and bone invasion subsequently confirmed in 23 of 25 patients. ^{99m}Tc-MDP bone scintigraphy detected metastases in 17 of 32 patients, whereas anti-NCA95 antibody scan detected more metastatic sites in 12 of 17 patients. Other investigators have also reported that bone marrow scintigraphy is superior to bone scintigraphy in diagnosing metastases in patients with carcinomas of the lung, kidney, bladder, and prostate (Widding et al. 1990; Bourgeois et al. 1991)

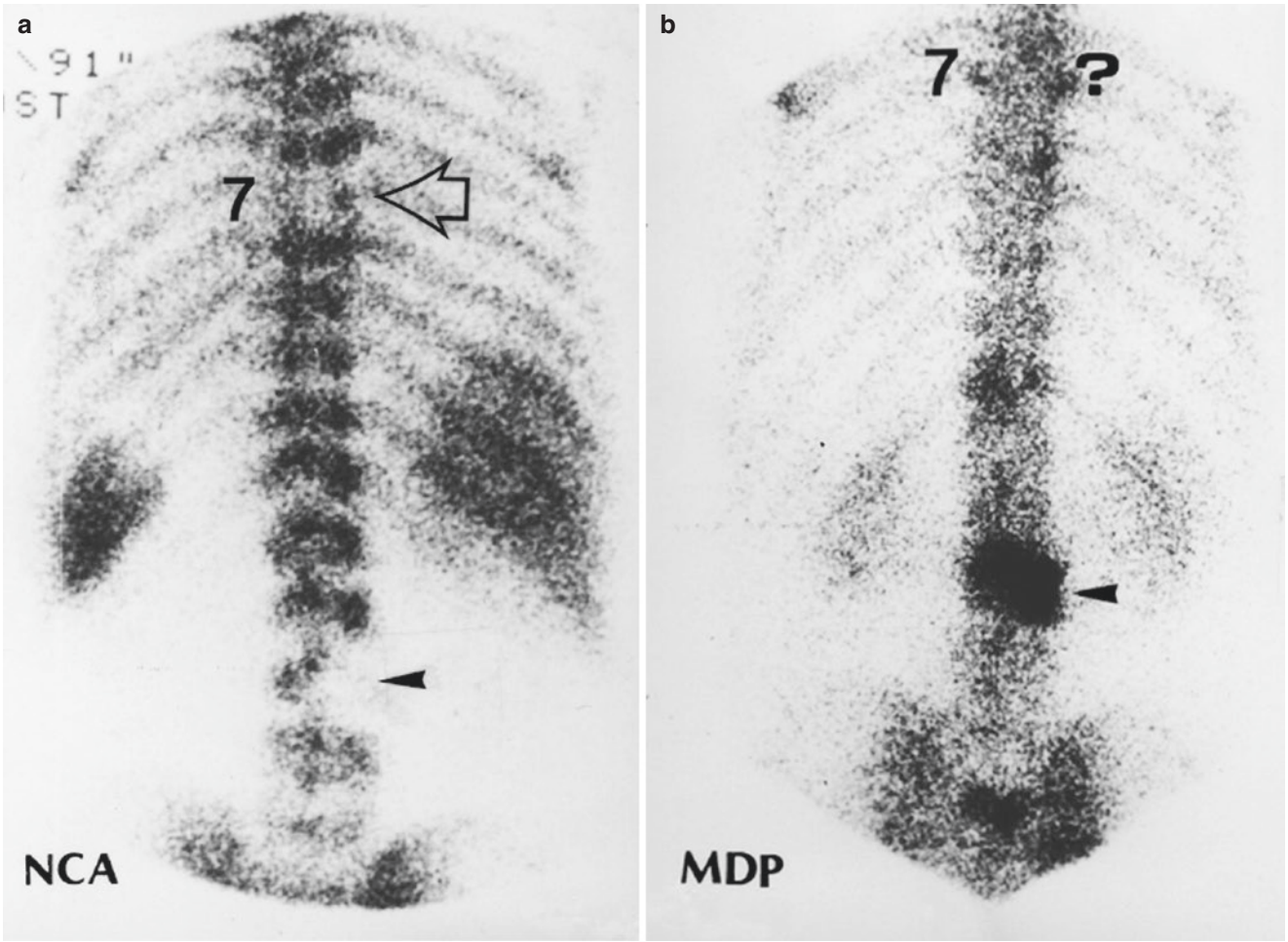

Fig. 17.38 Higher sensitivity of immunoscintigraphy in bone metastasis. (**a**) ^{99m}Tc-NCA95 immunoscintigraph of the spine with gastric cancer metastases shows photon defects in T7 and L3. (**b**) However, ^{99m}Tc-MDP bone scintigraph shows positive tracer uptake only in L3 (*arrow*) and no uptake in T7 (*?*)

(Fig. 17.38). However, Bourgeois et al. found that the specificity of bone scan was 100% compared to 87% specificity for marrow scan.

17.2 Primary Malignant Bone Tumors

Radiography is the single most efficient imaging method for primary bone tumors, both benign and malignant. Accordingly, bone scintigraphy was once not enthusiastically explored in primary bone tumors. However, with the popularization of refined gamma cameras, bone tumors have been subjected to extensive scintigraphic studies, leading to the accumulation of a volume of knowledge (Kirchner and Simon 1981; McLean and Murray 1984; Gilday et al. 1977). In addition, continued application of the pinhole technique to the diagnosis of bone tumors and tumorous conditions has theoretically and substantially contributed to widening of the horizon of ^{99m}Tc-MDP scanning in bone oncology (Baek et al. 1997; Bahk 1996, 1998; Bahk et al. 1995). This section describes the bone scintigraphic features of osteosarcoma, chondrosarcoma, Ewing's sarcoma, fibrosarcoma, and myelomas.

17.2.1 Osteosarcoma (Osteogenic Sarcoma)

Osteosarcoma is pathologically characterized by its ability to produce neoplastic bone in a fibrous stroma, hence osteogenic sarcoma. This is known as the most common variety of primary malignant bone tumor in the pediatric and adolescent age groups. Boys are affected slightly more frequently than girls. The most commonly affected bones are those of the knee with the proximal humerus the next most commonly affected. The location of tumor may be either central or parosteal in the metadiaphysis of the long bone with, not uncommonly, invasion of the adjacent soft tissue. Multiple primaries have been reported. Pathological fracture

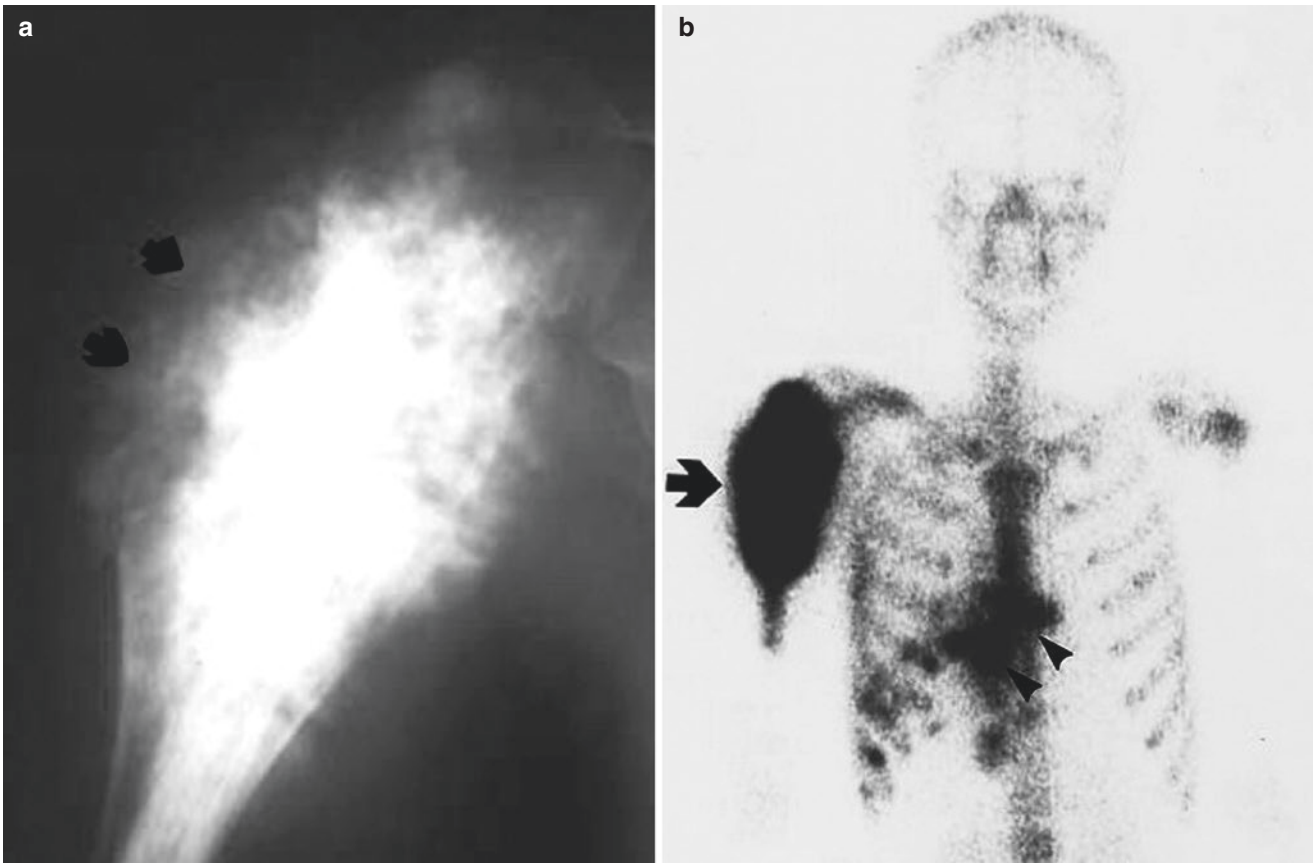

Fig. 17.39 Sclerotic osteosarcoma. (**a**) Anteroposterior radiograph of the right proximal humerus in a 12-year-old girl shows an Indian club-shaped radiodense tumor with a shaggy contour (*arrow*). (**b**) Anterior bone scintigraph reveals intense tracer uptake in the tumor (*arrow*). The tracer uptake in the ribs and sternum are also due to metastasis (*arrowheads*)

is relatively common, deforming the affected bone. Zeifang et al. (2000) surgically treated 30 patients with pathological fracture out of 336 patients with primary malignant bone tumors, reflecting approximately a 9% frequency.

The essential radiographic features of osteosarcomas are osteosclerosis (Fig. 17.39a), osteolysis (Fig. 17.40a), and their combination (Fig. 17.41a). Spicular, sunburst-like, and corona-like bone formation that arises from the lesional bone and periosteum is pathognomonic, especially when the adjacent soft tissues are concomitantly invaded (Fig. 17.42a). Periosteal osteogenesis with elevation and rupture (Codman's triangle) is another important but not specific sign (Fig. 17.43a). Pathological fractures modify radiographic appearance, manifesting as fracture lines and fragmentation with or without dislocation within a tumor mass, which is the seat of osteolysis and hemorrhage and/or necrosis (Fig. 17.44a).

Contrast angiography provides valuable information on tumor vascularity and blush (Fig. 17.45). Unlike the more common varieties of osteosarcoma, the telangiectatic subtype radiographically presents as an osteolytic tumor strongly resembling aneurysmal bone cyst. Being high-grade osteosarcoma, this subtype produces minimal osteoid with a greater portion of tumor replaced by hemorrhage and/or necrosis (Figs. 17.46a and 17.47a). MRI is an excellent imaging method that can be used for in vivo tumor tissue characterization of the telangiectatic subtype of osteosarcoma (Murphey et al. 2003) (Fig. 17.47).

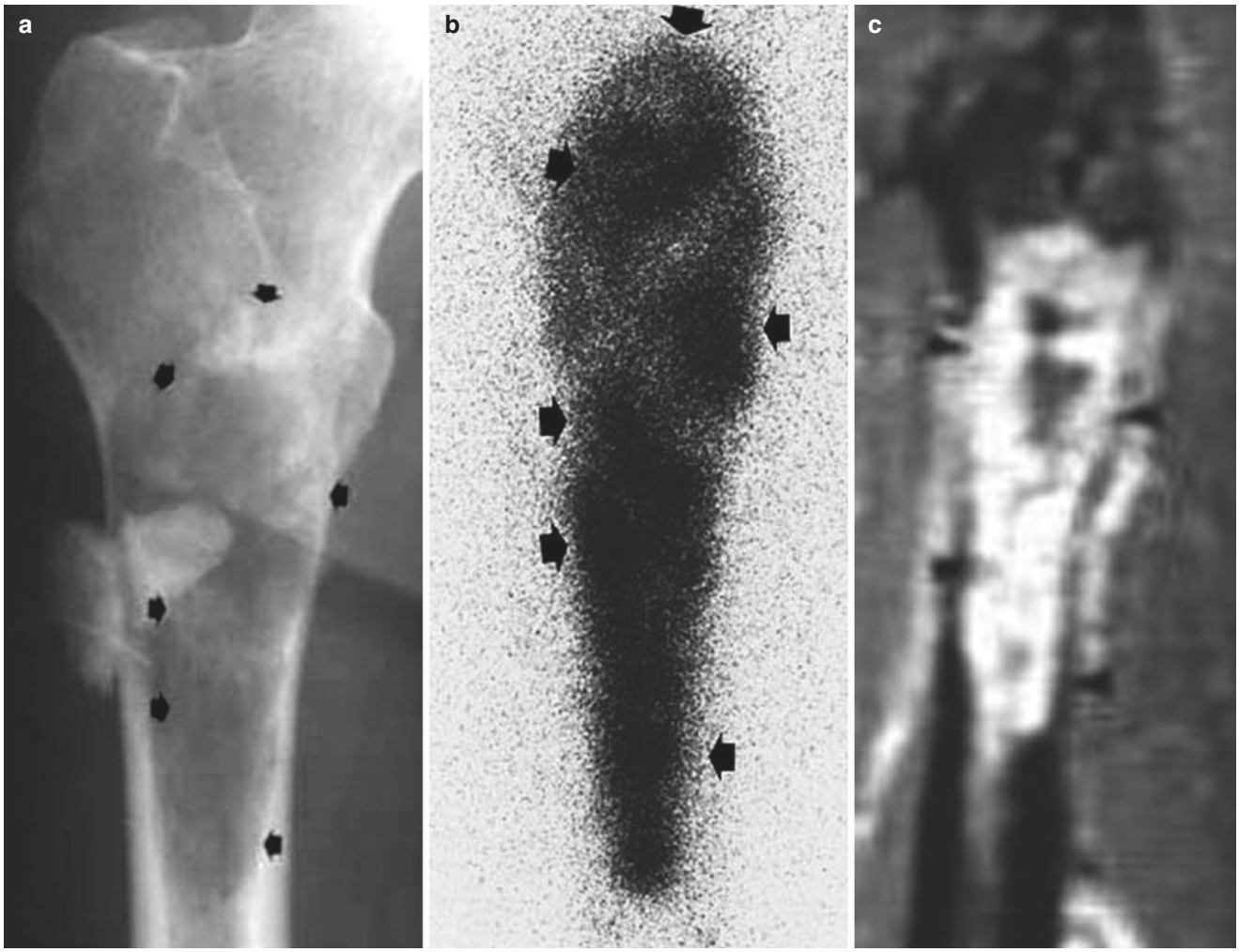

Fig. 17.40 Osteolytic osteosarcoma. (**a**) Anteroposterior radiograph of the right proximal femoral shaft in a 49-year-old male shows a large elongated concentric osteolytic tumor (*arrows*). The fingertip-like opaque shadow is exogenous material used as a stopper of a fenestration for biopsy. (**b**) Anterior bone scintigraph reveals intense tracer uptake in intramedullary tumor (*arrows*). (**c**) Gadolinium-enhanced T1-weighted MRI shows diffuse enhancement (*arrows*)

Scintigraphic manifestations vary according to the histological characteristics of the tumor. In general, the uniformly osteogenic or sclerotic type accumulates tracer extremely intensely (Fig. 17.39b), and the osteolytic type also accumulates tracer (Fig. 17.40b). The mixed type with intratumoral hemorrhage and/or necrosis presents as a mixture of photodense and photopenic areas (Fig. 17.41b). The main body of tumor within a long bone presented as a longitudinally oriented "hot" mass in both sclerotic and lytic types. The mass is fairly well demarcated on scintigraphs (Fig. 17.40b) but becomes distorted with patchy uptake when pathological fracture supervenes (Fig. 17.44c). Interestingly, the larger portion at the center of osteosarcoma with numerous fine tumor vessels and white blush is imaged as photopenia, and conversely the peripheral zone of tumor with lowered vascularity accumulates tracer rather intensely (Fig. 17.45). Fracture is usually indistinct on plain scintigraphs and can be imaged as such only by pinhole scintigraphy (Fig. 17.47). Characteristically, soft-tissue invasion produces the scintigraphic "sunburst" sign (Figs. 17.41b and 17.42b). It is to be emphasized that magnification scanning is extremely helpful for the visualization and analysis of all these pathological changes in detail. Indeed, simple bone distortion and increased uptake seen on

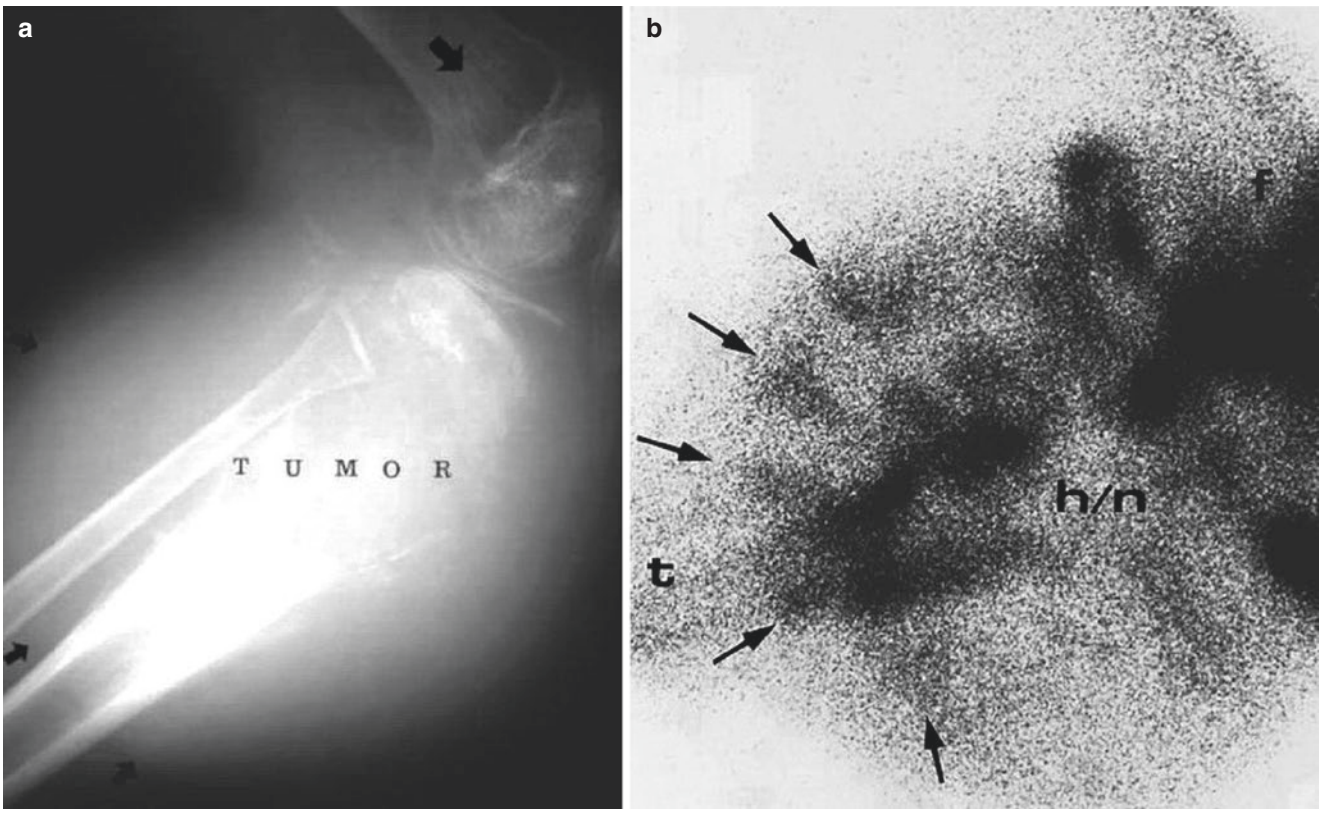

Fig. 17.41 Combined sclerotic and lytic osteosarcoma. (**a**) Lateral radiograph of the right proximal tibia in a 15-year-old boy shows a bizarre expansive tumor with sclerosis and lysis and soft-tissue invasion (*arrows*). (**b**) Lateral pinhole scintigraph reveals irregular areas of intense uptake mixed with photon defects (*arrows*) (*h/n* area of hemorrhage and necrosis as evidenced by MRI)

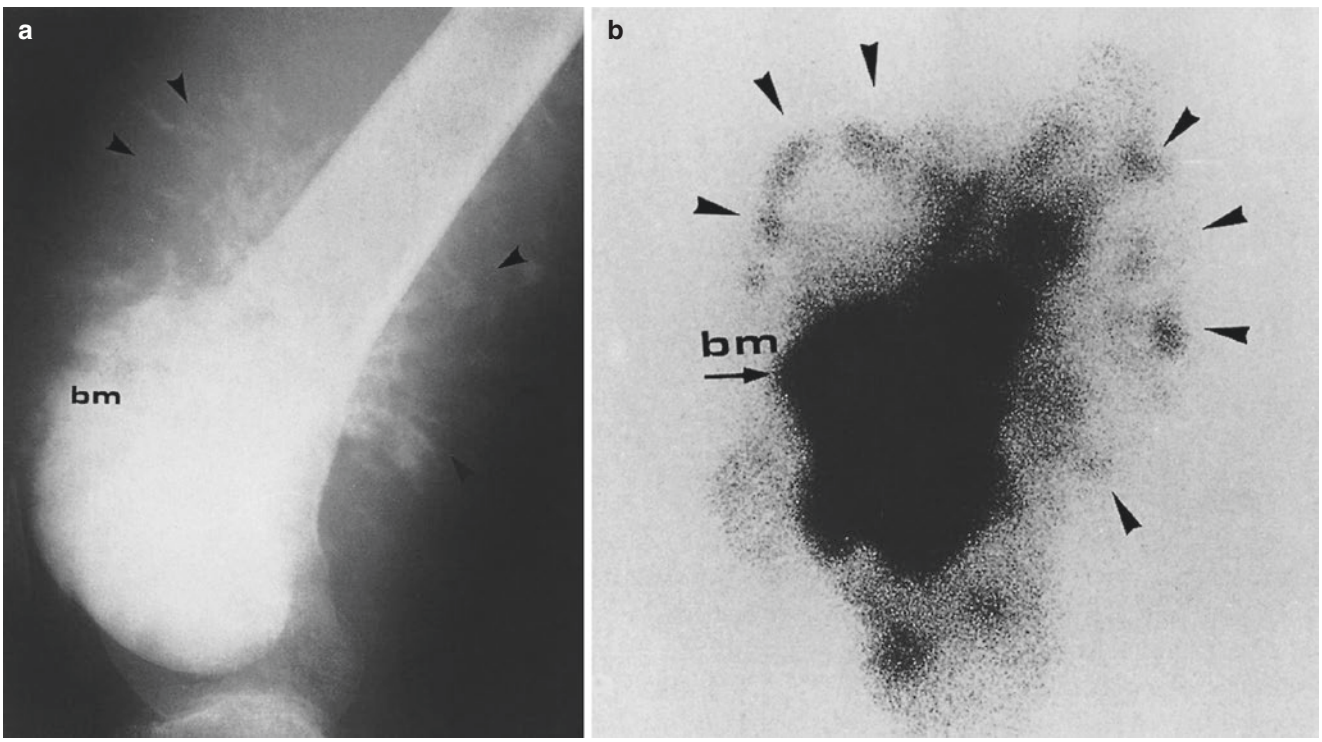

Fig. 17.42 Scintigraphic manifestation of the "sunburst" sign in osteogenic sarcoma. (**a**) Lateral radiograph of the right distal femur in a 21-year-old young man shows extensive neoplastic ossifications radiating into the muscles from a large sclerotic bone mass in the distal femur (*bm*). (**b**) Medial pinhole scan reveals bizarre linear and mottled tracer uptake radiating into the muscles (*arrowheads*) from the large tumor with extremely intense uptake in the distal femur (*bm*)

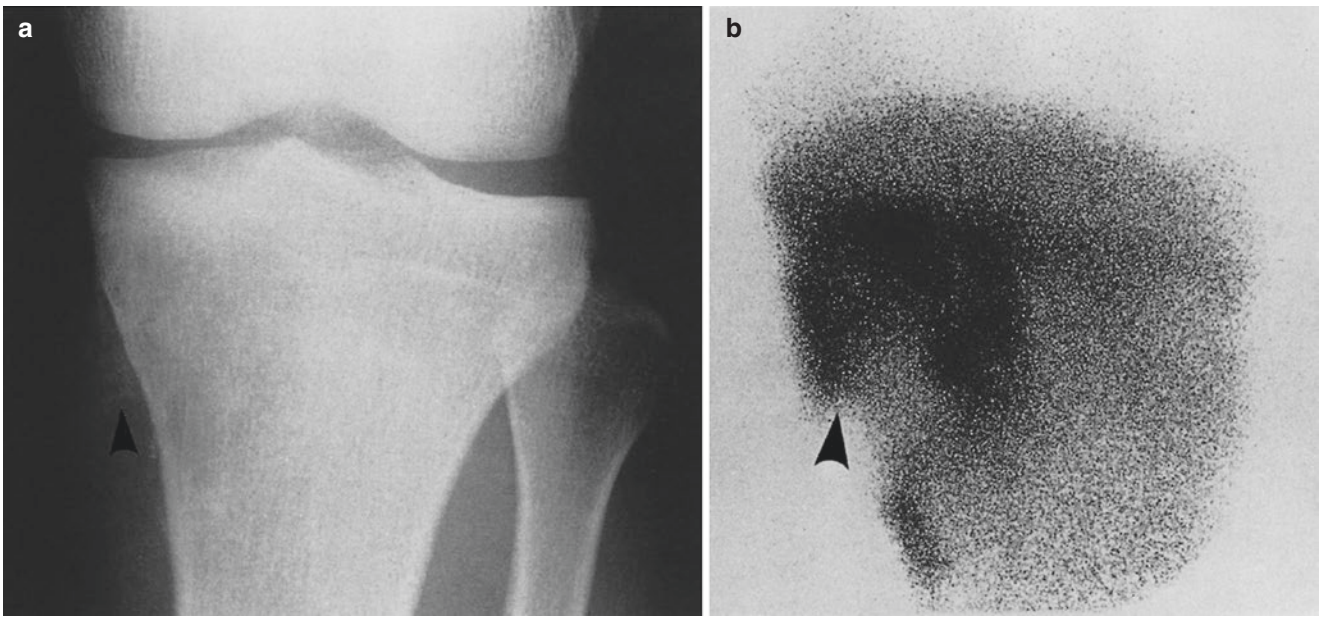

Fig. 17.43 Scintigraphic Codman's angle in osteogenic sarcoma. (**a**) Anteroposterior radiograph of the left knee in a 19-year-old young man reveals the classic, triangular periosteal elevation in the medial proximal tibial metaphysis (*arrowhead*) and osteolysis. (**b**) Anterior pinhole scan shows acutely angled, elevated periosteal uptake (*arrowhead*) and diffusely increased uptake in and around the destroyed bone

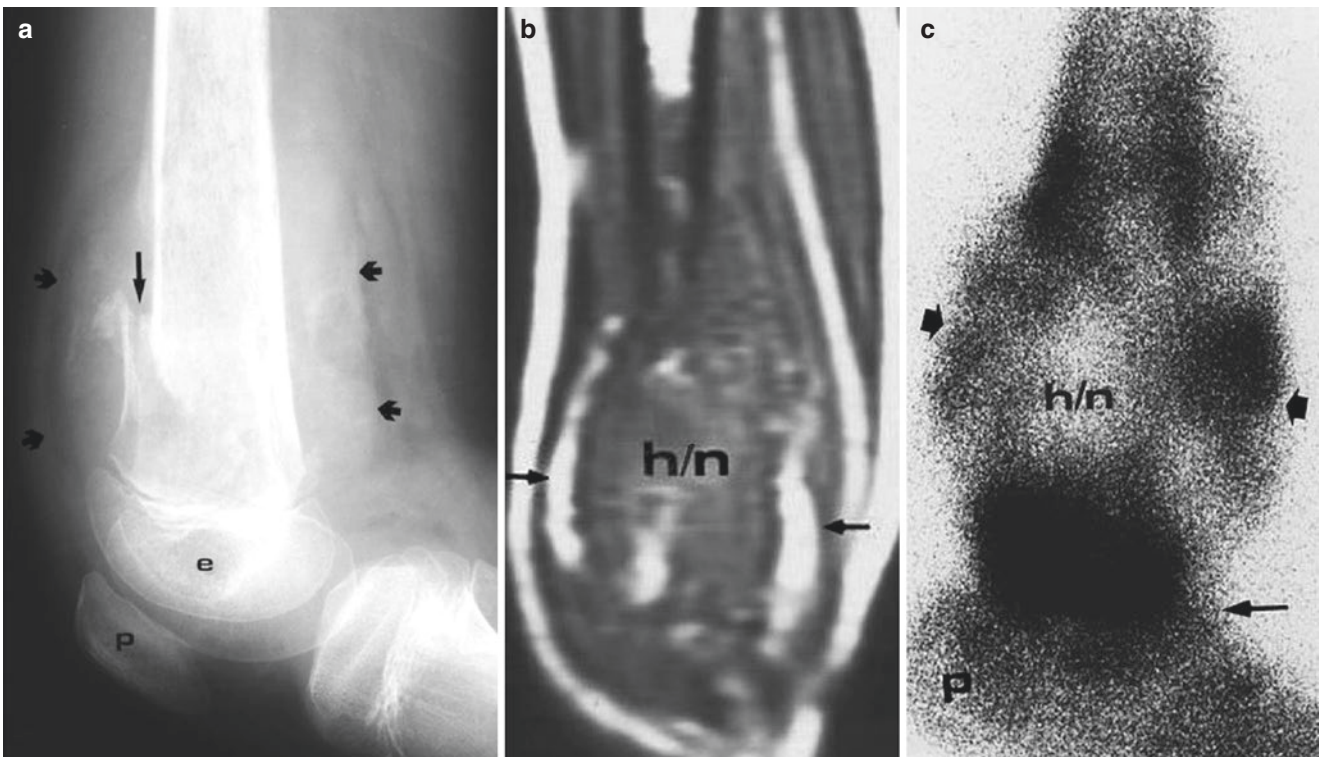

Fig. 17.44 Radiographic-MRI-scintigraphic correlation of osteosarcoma complicated with Codman's triangle. (**a**) Lateral radiograph of the left distal femur in a 13-year-old boy shows a mixture of sclerosis and lysis with soft-tissue invasion and tumefaction (*small arrows*). Note fracture line with dislocated fragments (*large arrow*) (*e* epiphysis, *p* patella). (**b**) Coronal T1-weighted MRI shows mixed signals of hemorrhage and necrosis within the main tumor (*h*/*n*). Rind-like bright and dark signals, respectively, denote fascial fat and ballooned cortex (*arrows*). (**c**) Anterior pinhole scan reveals a mixture of increased tracer uptake and photon defects in the main tumor (*h*/*n*) and surrounding nebulous uptake in expansive osteosarcoma (*small arrows*) (*large arrow* intense physeal and epiphyseal tracer uptake, *P* patella)

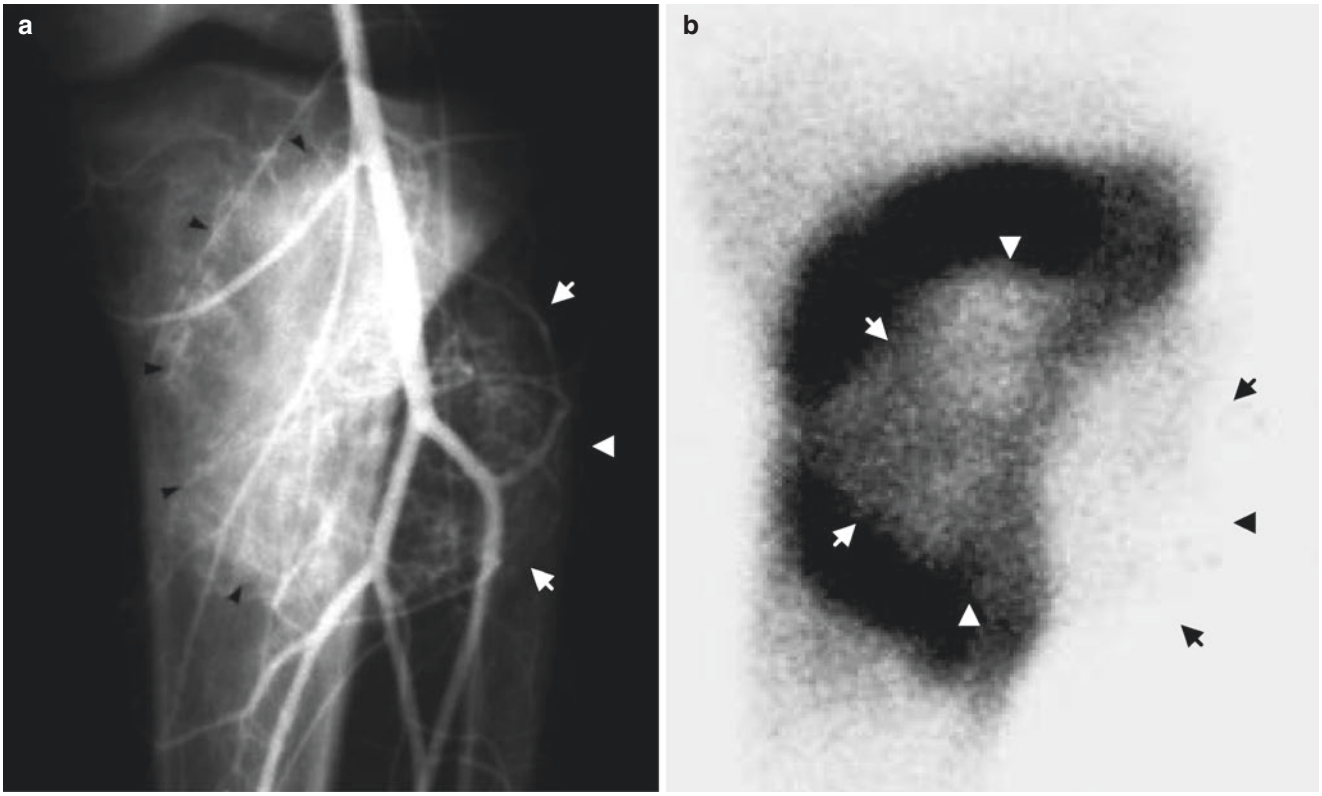

Fig. 17.45 Contrast angiography and pinhole scintigraphy in osteosarcoma. (**a**) Contrast arteriogram of the left proximal tibia with sclerotic tumor and soft-tissue invasion shows a fine meshwork of tumor vessels within the main tumor (*arrows*) and periphery (*arrowheads*). (**b**) Anterior pinhole scintigraph reveals subtle tracer uptake in the main tumor (*arrows*) and prominent reactive uptake in the periphery. The faintness of tumor uptake is presumably due to necrosis and neovascularization and prominent peripheral uptake due to reactive bone and neoplastic osteogenesis

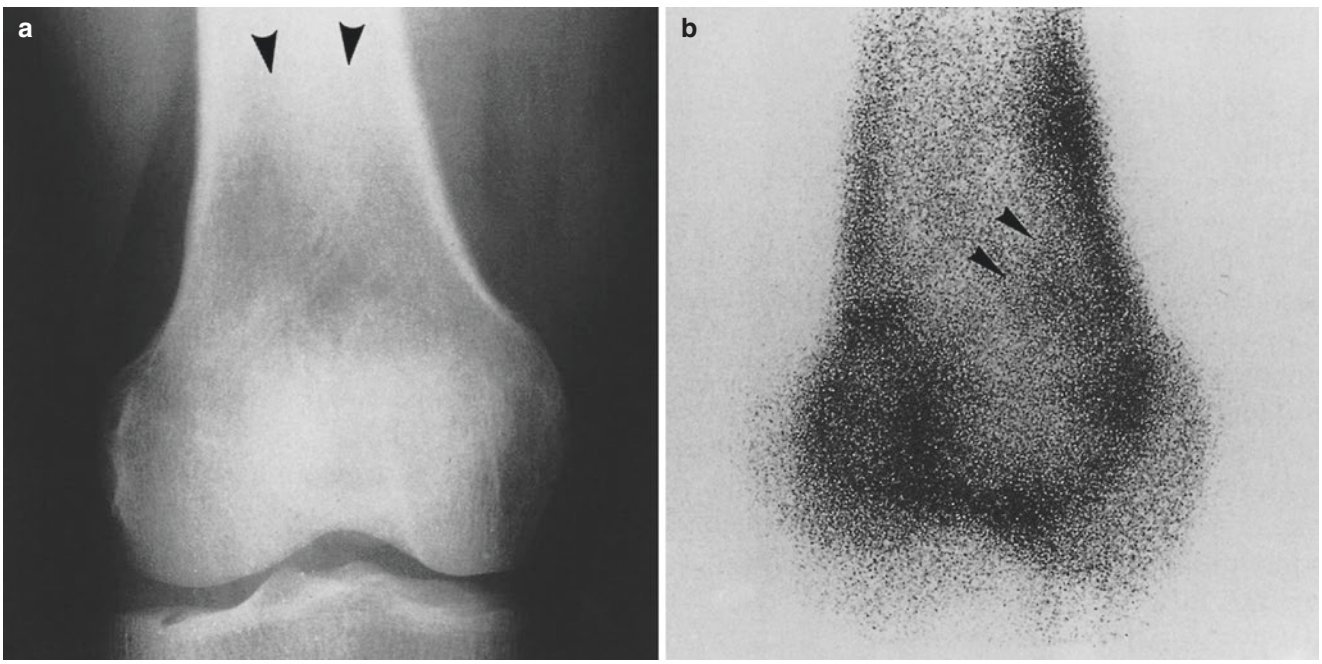

Fig. 17.46 Lucent and photopenic presentation of telangiectatic subtype of osteogenic sarcoma. (**a**) Anteroposterior radiograph of the right distal femur in a 33-year-old man reveals lysis with effaced trabeculae in the distal metaphysis (*arrowheads*). (**b**) Anterior pinhole scintigraph shows a large, well-demarcated, photopenic defect surrounded by a "hot" border. Mottled intratumoral tracer uptake is due to pathological fracture (*arrowheads*). The same case as Fig. 17.47 before overt fracture

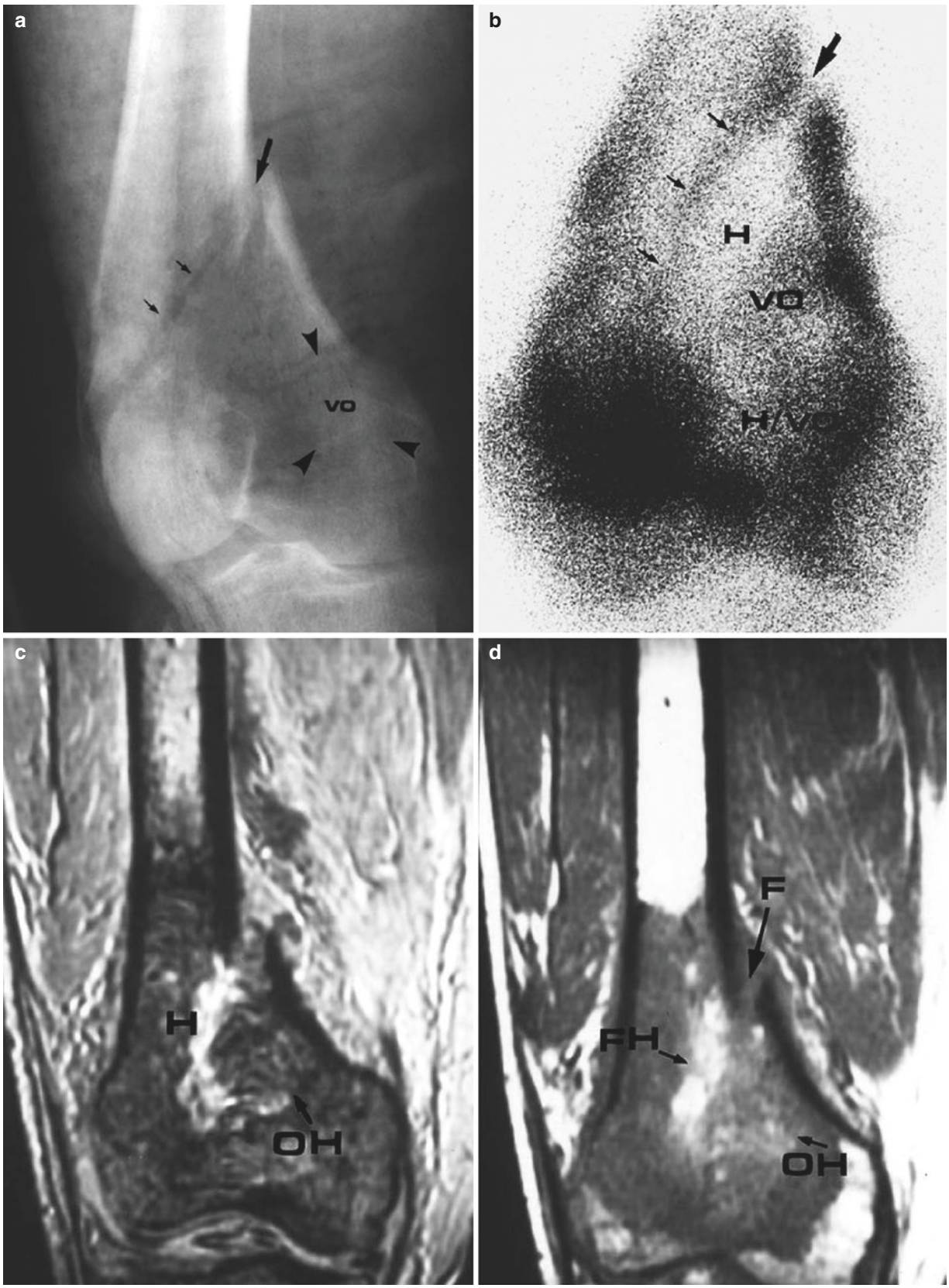

Fig. 17.47 Telangiectatic osteosarcoma. The same case as Fig. 17.46 after fracture. (**a**) Anteroposterior radiograph of the right distal femur in a 33-year-old male shows a large lytic lesion with fracture (*arrows*) and small island of visible osteoid (*VO*). (**b**) Anterior pinhole scintigraph reveals concordant photopenia in osteolysis and minimal uptake in visible osteoid (*VO*) (*H* hemorrhage, *H*/*VO* hemorrhage/osteoid). (**c**) Fat suppression MRI demonstrates hemorrhage in the fracture site (*H*) and old hemorrhage (*OH*). (**d**) T1-weighted MRI reveals fresh hemorrhage (*FH*) in the fracture (*F*) and old intratumoral hemorrhage (*OH*)

ordinary scintigraphs of an osteosarcoma can be resolved into the main bone change with intratumoral hemorrhage or necrosis and more importantly neoplastic osteogenesis in the periostea and the adjacent soft tissues.

As is mentioned above, the telangiectatic osteosarcoma produces minimal osteoid tissues and is replaced by hemorrhage and necrosis. Scintigraphically, the tumor is presented as a large irregular photopenic lesion in the long-bone metadiaphysis (Fig. 17.46b). Occasionally, pathological fracture and viable melted host bone or neoplastic osteoid may accumulate tracer visibly on pinhole scintigraphs (Fig. 17.47b).

17.2.2 Chondrosarcoma

The exact tissue origin of chondrosarcoma is obscure, but clearly the basic tissue is hyaline cartilage that may be transformed to myxoid, calcified, or ossified tissue. The cell differentiation ranges from almost benign to highly malignant. A chondrosarcoma is primary in nature or metamorphosed from osteochondroma, enchondroma, or exostosis. The incidence of the primary type is over 90% (WHO 2002). This is a malignant tumor of the middle-aged and elderly population and affects men 1.5 times more commonly than women. As with osteosarcoma, intraosseous localization may be central, juxtacortical, or peripheral. The femur, humerus, and axial skeleton are affected in more than 75% of cases and epimetaphysis is the typical site of involvement. Conventional radiography, CT, and MRI (Collins et al. 2003) and bone scanning are used for diagnosis.

Radiographic findings vary from well-defined osteolysis with mild calcification through poorly defined bone destruction with moderate calcification (Fig. 17.48a) to expansive tumefaction with cortical rupture and soft-tissue invasion (Fig. 17.49a). CT scan shows all these features more clearly, distinguishing tumor matrices, calcification, and soft-tissue invasion (Fig. 17.48b), and MRI demonstrates characteristic signal intensity changes of cartilage, myxoid tissue, and calcification (Fig. 17.49). For example, T1-weighted MR images reveal a geographic lesion with low signal intensity that may occasionally contain multiple daughter tumors with increased signal intensity (Fig. 17.49b). Enhanced by contrast agent, the daughter tumors and reactive bone encapsulation become distinctly delineated with bright signal intensity (Fig. 17.49c).

On pinhole scintigraphy, tracer uptake is mild (Fig. 17.48c), moderate, or marked (Fig. 17.49d) according to the degree of calcification.

Visual correlation of the tracer uptake and radiographic change indicates that mild uptake occurs in the tumor matrix with mild calcification, while marked uptake occurs with marked calcification (Fig. 17.48). Conventional angiography in one of our chondrosarcoma cases showed that the grade of neovascularization roughly paralleled the radiopacity of tumor and the intensity of tracer uptake (Fig. 17.48). Radiographically and on CT, lucent tumor matrix with photopenia showed normal vascularity, whereas the matrix with calcification showed hypervascularization. Thus, it appears that tumor vessels are unrelated with tracer uptake in chondrosarcoma as they are in osteosarcoma (Fig. 17.45).

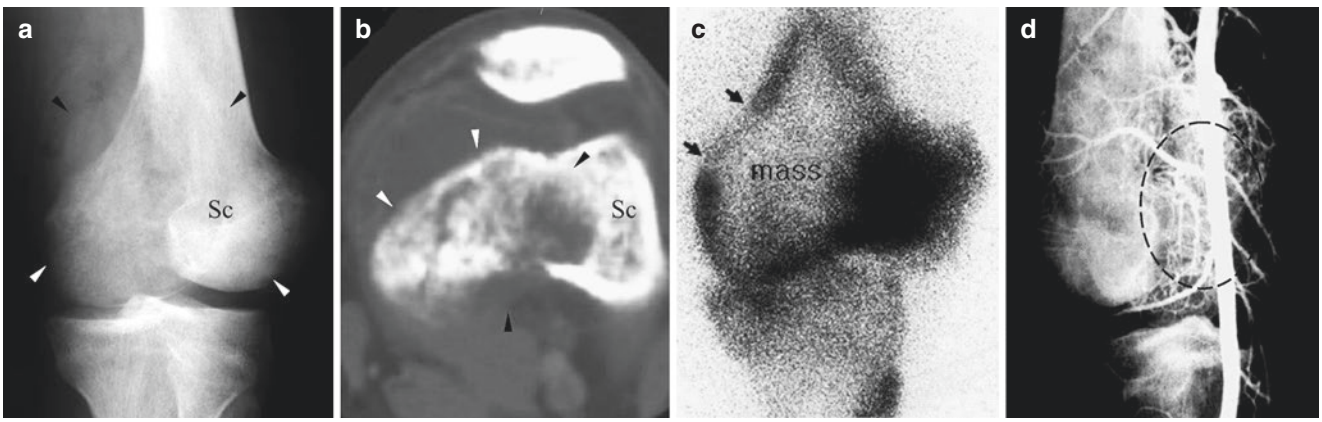

Fig. 17.48 Primary chondrosarcoma. (**a**) Slightly oblique radiograph of the left distal femur in a 28-year-old man shows poorly defined expansive tumor (*arrowheads*). The tumor consists of a lucent area in the left half and a sclerotic area in the right half (*Sc*). (**b**) Axial CT scan shows lytic and sclerotic zones (*arrowheads*). (**c**) Pinhole scan shows mild uptake in the chondroid portion (*mass*) and intense uptake in the osteoid portion. Note reactive high uptake in cortex with low uptake in rupture (*arrows*). (**d**) Contrast angiography shows profuse neovascularization in the osteoid portion (*circle*)

Fig. 17.49 Clear and granular cell chondrosarcoma with transcortical invasion. (**a**) Anteroposterior radiograph in a 77-year-old woman with growing painful mass in the left distal femur shows a poorly defined tumor with amorphous diffuse calcification (*large arrows*) and barely discernible muscular extension (*small arrow*). (**b**) T1-weighted (481/20) MR image shows multilobular intermediate signal intensity tumor (*large arrows*) with transcortical invasion of muscle (*small arrow*). (**c**) Contrast-enhanced T1-weighted image shows stain of multilobular tumor against the background of low signal matrix. Note enhancement of reactive bone capsule in the main (*large arrows*) and extended tumors (*small arrow*). (**d**) Enlarged planar bone scan shows a large tumor with intense tracer uptake consisting of multiple nodular daughter tumors (*large arrows*). Peculiarly, the extended tumor does not accumulate tracer, presumably due to the sparsity of calcification (*circles*). Diagnosis was confirmed by biopsy and the tumor was treated conservatively (courtesy of Bom Sahn Kim, M. D. Ewha Women's University Hospital, Seoul)

17.2.3 Ewing's Sarcoma

Ewing's sarcoma is a highly malignant tumor, consisting of small round cells of unknown tissue origin. The tumor predominantly affects children and young adults, with a strong predilection for males. No bones are immune, but the long bones of the lower extremity and pelvic bones are affected in 60% of patients. Not infrequently the spine and ribs are involved. The tumor tends to metastasize early to the bone and lung.

Radiographic features vary between patients, manifesting any of osteosclerosis, osteolysis, and mixed change and any combination of these. Bone condensation in the sclerotic type is intense, often with periosteal lamellation (Fig. 17.50a). The lamellation may be either single or multiple layered, giving rise to the "onion skin" sign if multilayering. Codman's triangle may be seen as in other malignant bone tumors. Osteolysis within the marrow space is permeative and poorly demarcated (Fig. 17.51a), and the mixed form shows a mixture of lysis and sclerosis (Fig. 17.51a). Occasional lesions of the irregular bones such as the pelvis and vertebrae may show ballooning (Fig. 17.52a). The ballooning may represent rapidly expanding osteolysis or "pseudoaneurysmal bone cyst."

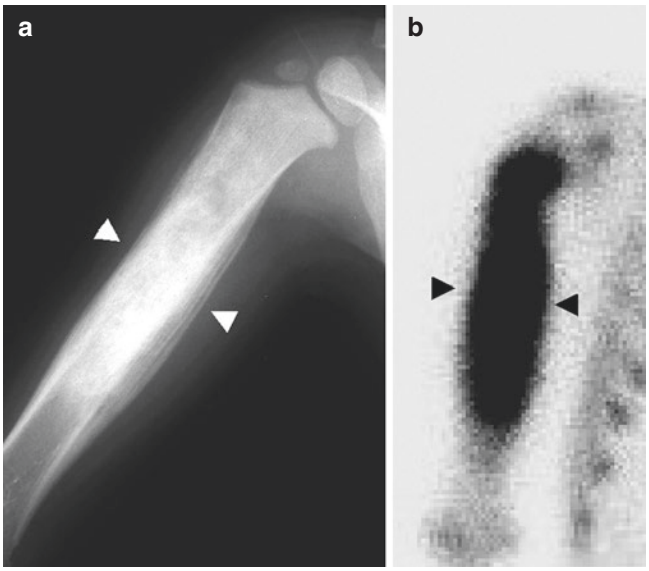

Fig. 17.50 Ewing's sarcoma. (**a**) Near lateral radiograph of the right humerus in a 5-year-old male child shows osteosclerosis with periosteal thickening (*arrowheads*). (**b**) Planar scintigraph reveals intense tracer uptake in sclerosing tumor (*arrowheads*)

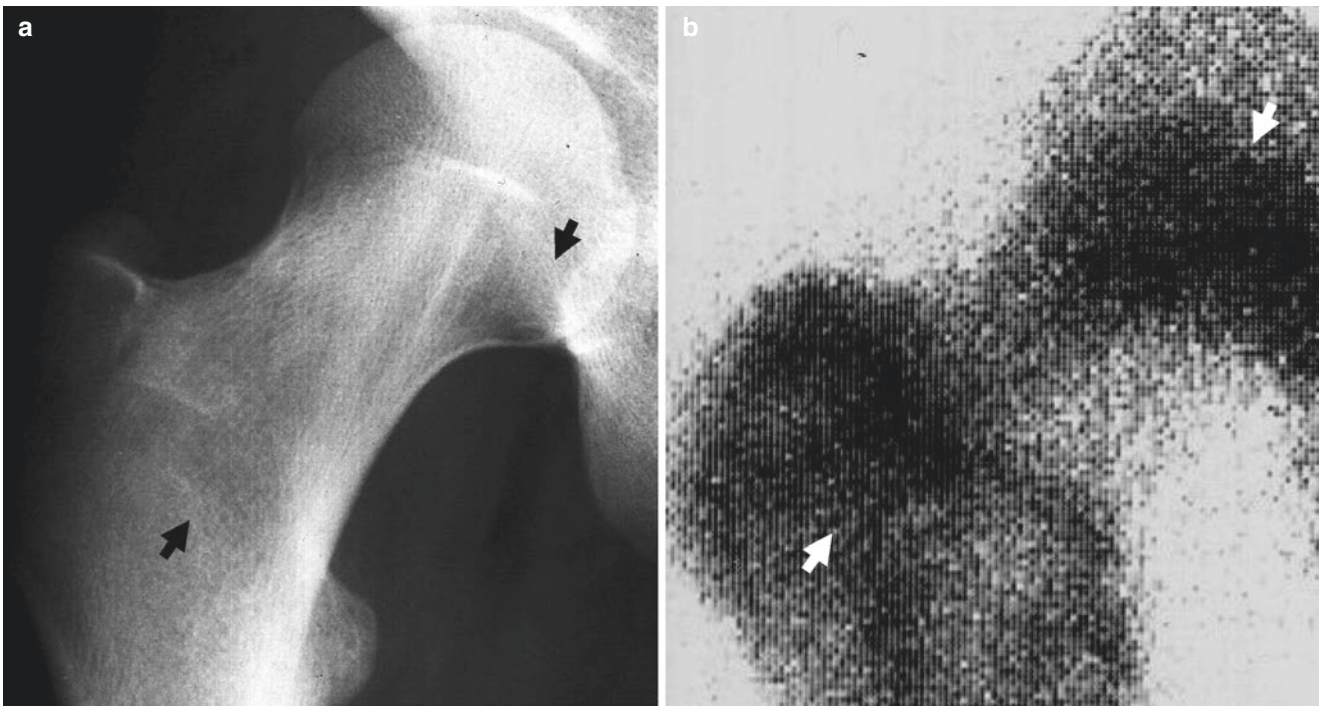

Fig. 17.51 Ewing's sarcoma. (**a**) Anteroposterior radiograph of the right proximal femur in a 17-year-old male shows two large ill-defined areas of permeative osteolysis in the upper and lower portions of the neck (*arrows*). (**b**) Magnified anterior planar scintigraph reveals two large concordant areas of increased tracer uptake (*arrows*)

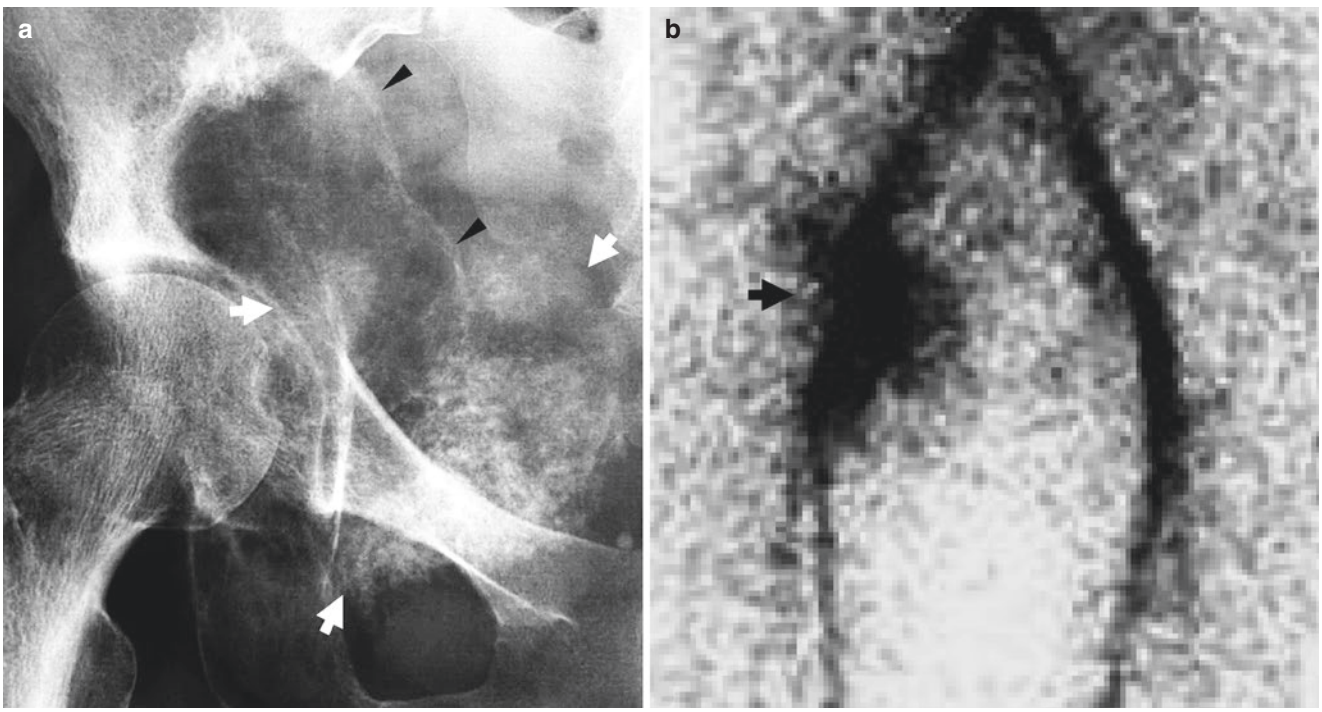

Fig. 17.52 Ewing's sarcoma in the iliac bone. (**a**) Anteroposterior radiograph of the right pelvis in an adult shows a large irregular tumor with bone formation (*arrows*) and central ballooning osteolysis with rind (*arrowheads*). (**b**) Nuclear angiogram reveals prominent blood pool at the center of the tumor that corresponds to expansive lysis (*arrow*)

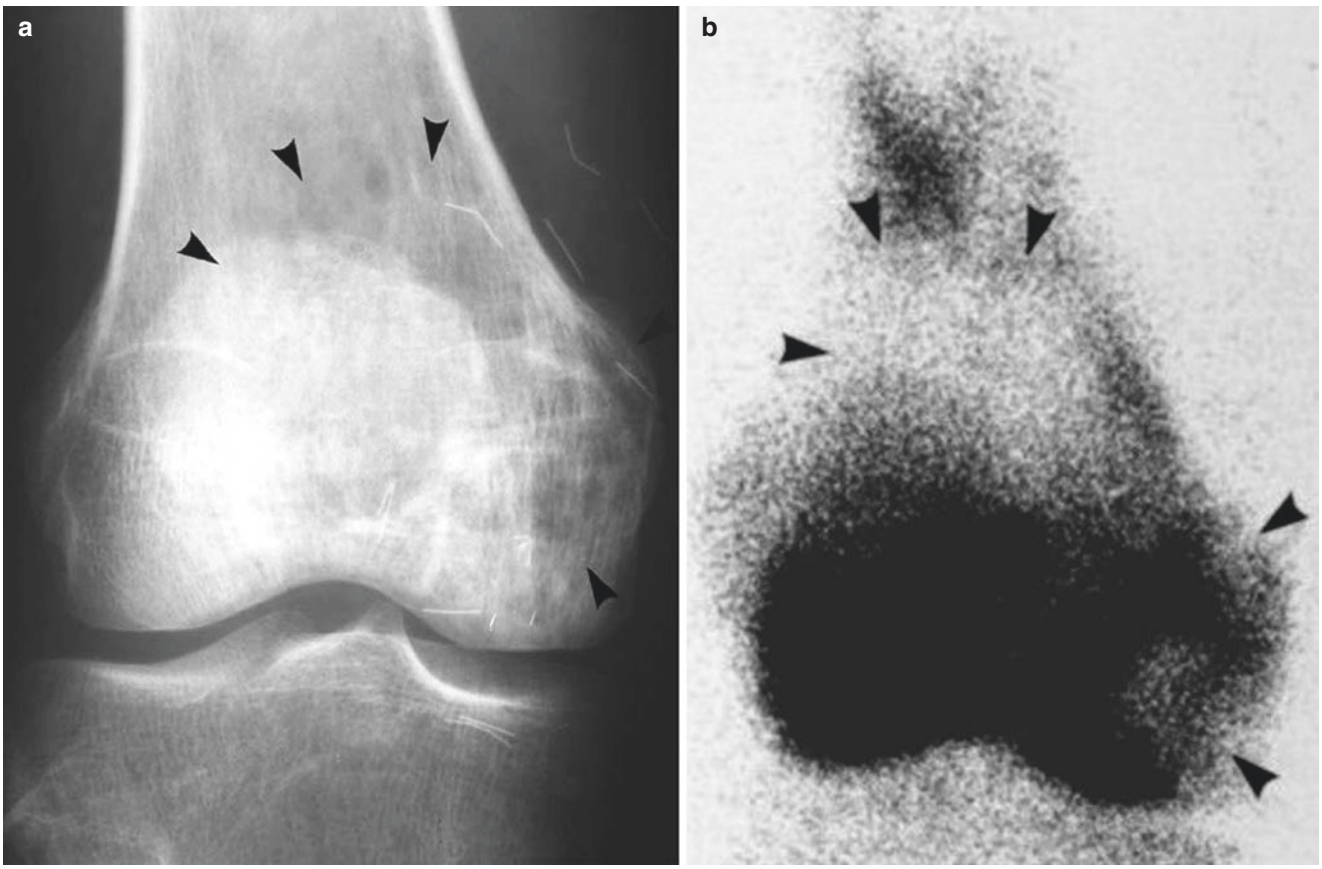

Fig. 17.53 Bone destruction in fibrosarcoma. (**a**) Anteroposterior radiograph of the right distal femur in a 36-year-old female shows large geographic bone destruction (*arrowheads*). (**b**) Anterior pinhole scan reveals a large photon defect in the main tumor (*upper three arrowheads*) with marginal tracer uptake in the reactive zone (*lower pair of arrowheads*)

Scintigraphic features also vary according to the tumor type. Basically, the osteosclerotic type accumulates tracer intensely (Fig. 17.50b), while the osteolytic type accumulates less tracer (Fig. 17.51b). Understandably, the tracer uptake in the mixed variant is irregular and heterogeneous (Fig. 17.51b). Nuclear angiography is ideal for detecting aneurysmal cystic change of Ewing's sarcoma or tumor hypervascularity (Fig. 17.52b). Bone scintigraphy has the additional diagnostic advantage of discovering regional and distant metastases in Ewing's sarcoma as in other malignancies.

17.2.4 Fibrosarcoma

Malignant fibrous tumors of bone include the primary and secondary fibrosarcomas and malignant fibrous histiocytoma that has been established as a distinctly independent entity.

The primary form may originate from the medullary space, periostea, or soft tissues, with secondary extension to bone. Pathologically, the tumor cells are spindle shaped, producing no bone, and the differentiation varies from low to highly malignant. This is a tumor of middle age, without gender predilection. Slightly more than 50% of cases are seen in the bones about the knee and in the humerus. Secondary fibrosarcomas are the result of malignant transformation of benign bone disorders such as Paget's bones, medullary bone infarcts, or irradiated bones.

The characteristic radiographic manifestation of fibrosarcomas of bone is large geographic bone destruction, the contour of which is poorly defined because reactive sclerosis is minimal or absent (Fig. 17.53a). Osteolysis in this tumor is permeative, and accordingly the border shows a moth-eaten appearance. Periosteal invasion is uncommon, but it may cause spiculation, lamellation, or even the Codman's triangle sign when present. Malignant fibrous histiocytoma also

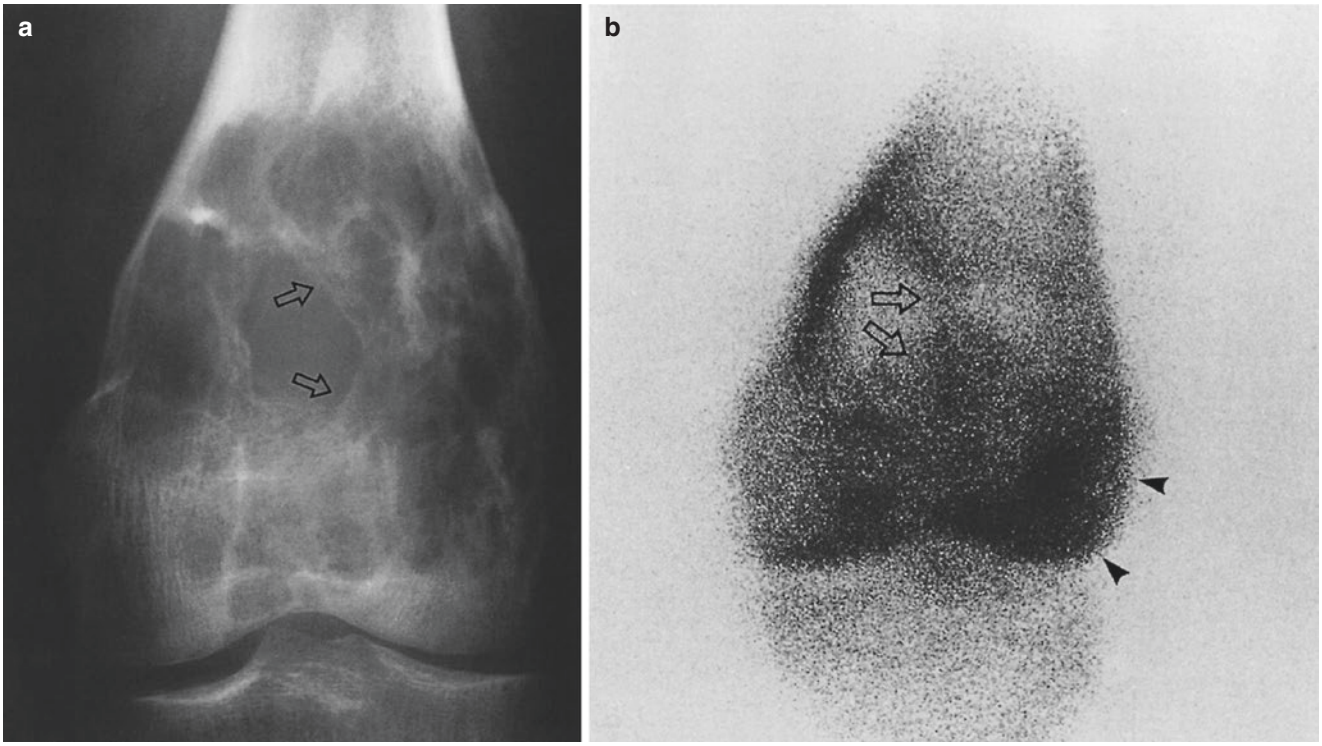

Fig. 17.54 Malignant fibrous histiocytoma. (**a**) Anteroposterior radiograph of the left distal femur in a 34-year-old man shows a large, expansile, lytic tumor involving centrally the metaphysis with multiple, irregular septations (*open arrows*). The cortices appear expanded, thinned, and scalloped but not ruptured. (**b**) Anterior pinhole scintigraph shows a large, expansile, photopenic mass with irregular septation (*open arrows*). The regional cortex shows increased tracer uptake medially where it is thinned and bulged. Patchy tracer uptake in the lateral condyle may represent extended uptake (*arrowheads*)

involves bone, forming a single large defect or multiple small defects located centrally or eccentrically in long-bone diaphyses. In occasional cases small lytic areas may coalesce (Capanna et al. 1984), and the tumor becomes expansive showing a bubbly appearance due to septum-like formations (Fig. 17.54).

Pinhole scintigraphy of primary fibrosarcoma shows a large ill-defined photon defect surrounded by an irregular rim of watershed or extended uptake (Fig. 17.53b). The photopenic manifestation of this tumor may be explained on the basis of that fibrous matrix is basically not osteogenic. The nonosteogeny of tumor along with the absence of significant reactive osteosclerosis may be a likely reason for poor scintigraphic demarcation. Infiltrating variants may present as patchy areas of intense tracer uptake intermingled with irregular photopenic areas. The intramedullary spread can be diagnosed by bone scan. The basic scan manifestations of malignant fibrous histiocytoma with bone destruction are essentially the same as those of osteolytic type primary fibrosarcoma except for the expansiveness and multicystic appearance with septation (Fig. 17.54b). The latter finding has a strong resemblance to that in metastatic follicular thyroid carcinoma with septation (Fig. 17.21a).

17.2.5 Myeloma (Plasma Cell Myeloma)

Myeloma is characterized by neoplastic proliferation of abnormal plasma cells in the red bone marrow. Multiple myeloma is not a rare disease, accounting for 1% of all malignant tumors. This is primarily a disease of the elderly, but the range of incidence is wide, between 25 and 80%. One most recent population study performed in the South Thames area of the United Kingdom has shown the age-standardized

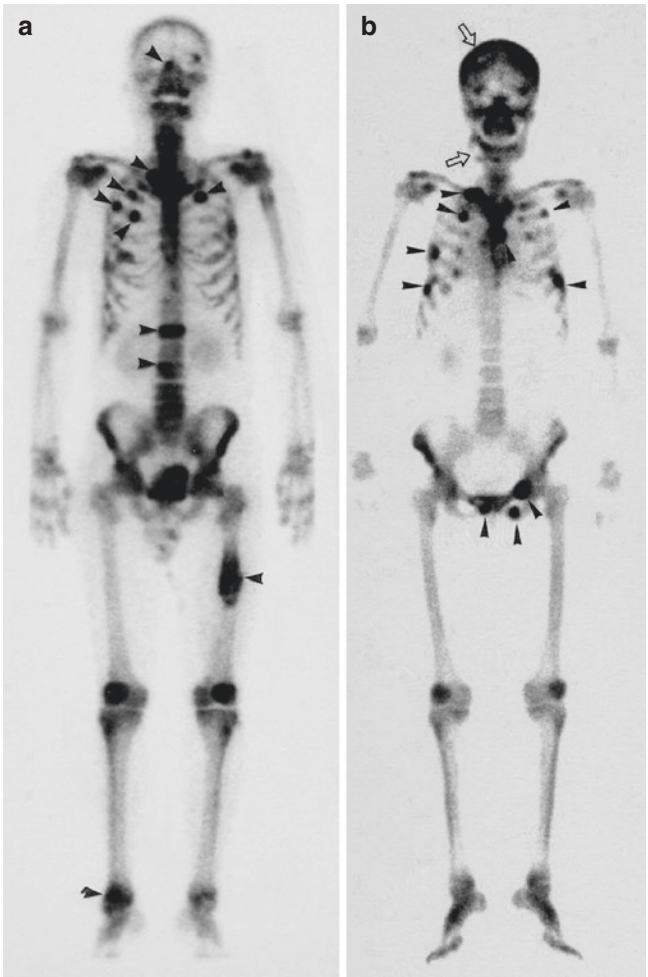

Fig. 17.55 Varied axial skeletal involvement in multiple myeloma in two different patients. (**a**) Anterior whole-body scintigraph in a 58-year-old man with multiple myeloma shows widely scattered spotty uptake in the nasal bone, ribs, spine, right femur, and left distal tibia (*arrowheads*). (**b**) Anterior whole-body scintigraph in a 56-year-old woman with multiple myeloma reveals involvement of the cranium, ribs, sternum, and pelvis (*arrowheads*). *Open arrow* in the skull denotes photopenic manifestation

rate of multiple myeloma to be 3.29 per 100,000 with the median age of those affected being 73 years (Phekoo et al. 2004). When first seen in the clinic, the lesions are either multiple (more than 50%), generalized (15%), or solitary (25%). Solitary myeloma may eventually develop into multiple or generalized lesions. The axial skeleton including the skull, spine, pelvis, sternum, and shoulder bones, as well as the limb bones, are involved (Fig. 17.55). Symptoms include malaise, fatigability, skeletal pain especially in the spine and rib cage, and bone deformity. The solitary form may well pass unnoticed and the generalized form may be disguised as simple osteoporosis. In either form, the first event that brings the patient to hospital may be pathological fractures. Protein electrophoresis may reveal an increase in the globulin fraction, and immunoelectrophoresis can identify different types of globulin such as IgG, IgA, and rarely IgM.

The radiographic features include multiple or diffusely spread bone destructive changes or solitary lysis. Characteristically, lesions in the skull are well defined and discrete and give rise to a "punched-out" or "bubbly" appearance (Fig. 17.56). If generalized, however, the individual lesions imperceptibly blend into advanced senile osteoporosis (Fig. 17.57). Myelomatous bones are fragile and prone to pathological fracture, but the fractures are radiographically undetectable in most cases because of severe osteoporosis. An interesting radiographic sign of multiple myeloma is endosteal scalloping caused by the physical effect of proliferative plasma cells that are expansive (Fig. 17.58). With gradual increase in volume, myelomas in small bones such as the sternum and ribs may become expansive, eventually breaking the cortex (Fig. 17.59a). On occasion, such lesions are permeant and expansive and induce a periosteal reaction (Fig. 17.60).

^{99m}Tc- MDP bone scintigraphy was once held to be of limited value since the plasma cells of myeloma do not accumulate tracer regardless of the disease type (Wahner et al. 1980; Waxman et al. 1981). However, the extended application of whole-body and pinhole scans to the diagnosis of myelomas has indicated that bone scintigraphy is not only useful but also even indispensable in certain clinical settings. The first and most important situation is probably pathological fractures that are common in myelomatosis. Radiographic diagnosis of such fractures is notably difficult and even harder when advanced myelomatosis is superimposed on severe porosis (Fig. 17.57). Fortunately, fractures intensely accumulate tracer regardless of the porosis in host bones. The second advantageous situation is solitary myelomas in the long tubular bones and small bones such as the ribs and sternum (Fig. 17.59a). A sizeable lesion may be missed radiographically in these bones, but pinhole scintigraphy can reveal signs that strongly suggest or indicate the diagnosis. Myeloma in the sternum presents as an expansive photon defect visualized as broken eggshell-like uptake in the ruptured cortex (Fig. 17.59a). CT scan is an excellent alternative (Fig. 17.59b). Pinhole scintigraphy is far more informative in studying solitary myeloma in the long bones because it can

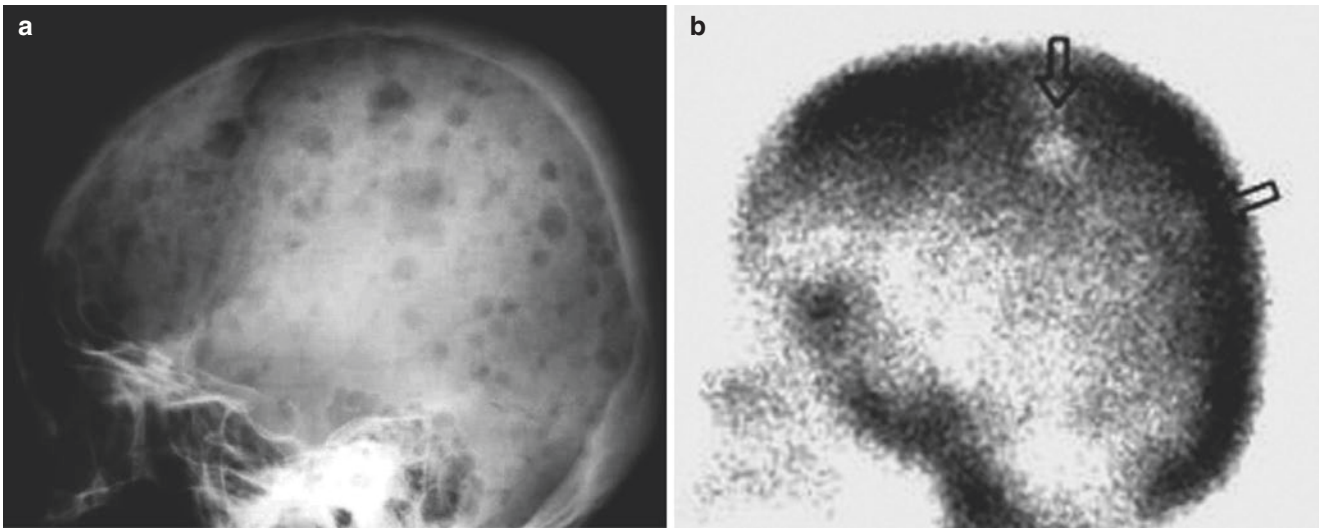

Fig. 17.56 Punched-out lysis in multiple myeloma. (**a**) Lateral radiograph of the skull in a 60-year-old female shows classic multiple punched-out lesions. (**b**) Lateral pinhole scintigraph reveals many roundish photopenic areas (*open arrows*). Note that only large lesions are visualized. The planar scan did not reveal these lesions

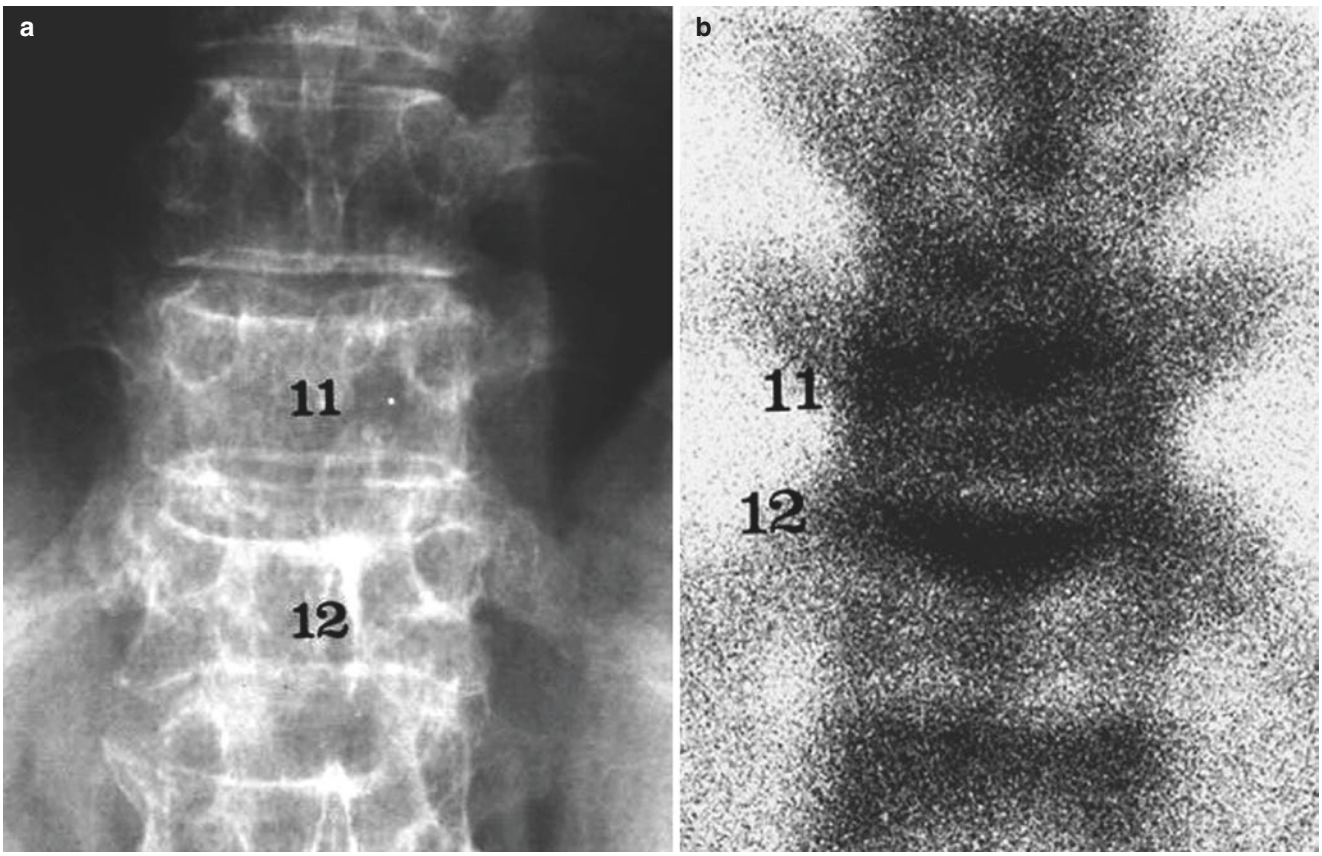

Fig. 17.57 Myelomatosis in porotic skeleton. (**a**) Anteroposterior radiograph of the lower thoracic spine with severe porosis shows blending of myeloma with porosis concealing fractures. (**b**) Posterior pinhole scan reveals diffusely increased bone uptake with prominent uptake in T11 and T12 upper endplates denoting compression fractures

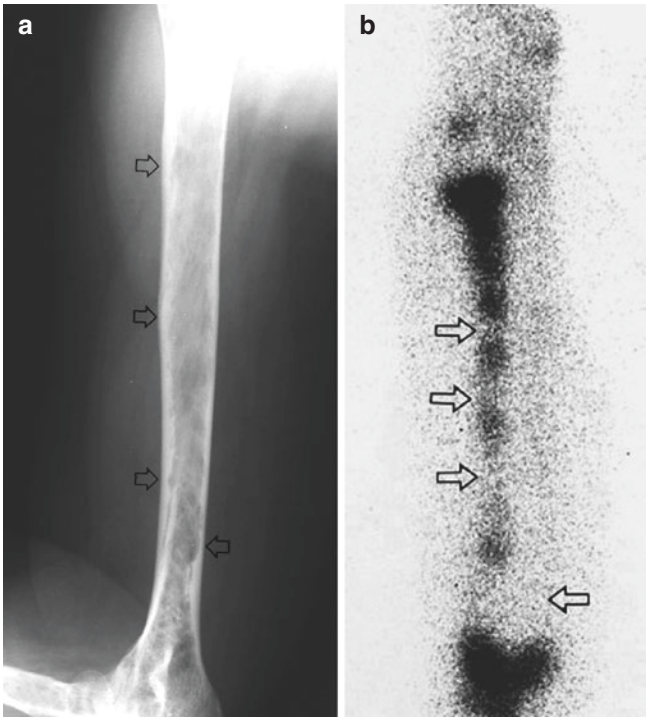

Fig. 17.58 Bone marrow scan of myelomatosis with endosteal scalloping. (**a**) Lateral radiograph of the right humerus in a 58-year-old female shows endosteal undulation (*open arrows*). (**b**) ^{99m}Tc-tin colloid scan reveals spotty photon defects due to myelomas that cause endosteal scalloping (*open arrows*)

distinguish permeative bone invasion from simple expansion (Fig. 17.60b). The tracer uptake in simple expansion or scalloping is negligible or very subtle at most, but that in actively invaded or ruptured cortex is obvious. The third advantage is scintigraphic detection of radiographically invisible myelomas, but this is rare.

On the other hand, ^{99m}Tc-tin colloid bone marrow scintigraphy is a useful adjunct to the diagnosis of myelomas (Feggi et al. 1988) and the myelomas, metastases, lymphoma, and leukemia that are rooted in the red bone marrow (Lentle et al. 1987). Bone marrow scanning using radiocolloids relies on the phagocytosis of reticuloendothelial cells. Accordingly, once the bone marrow has been replaced with myeloma cells, they become photopenic on colloid scintigraphs (Fig. 17.58). ^{18}F-FDG PET is a useful adjunct to the diagnosis of multiple myeloma. The sensitivity and specificity in detecting multiple myeloma lesions have been reported to be 85 and 92%, respectively (Bredella et al. 2005). The superiority of ^{18}F-FDG PET is based on the fact that ^{18}F-FDG PET can directly visualize denatured plasma cells that avidly consume glucose, while ^{99m}Tc-MDP bone scintigraphy can image indirect bone change that occurs secondarily (Fig. 17.61). In passing, it is worth mentioning that pinhole scintigraphy can conveniently and reliably evaluate and archive the results of adjuvant chemotherapy, external irradiation, or bone marrow replacement (Fig. 17.62).

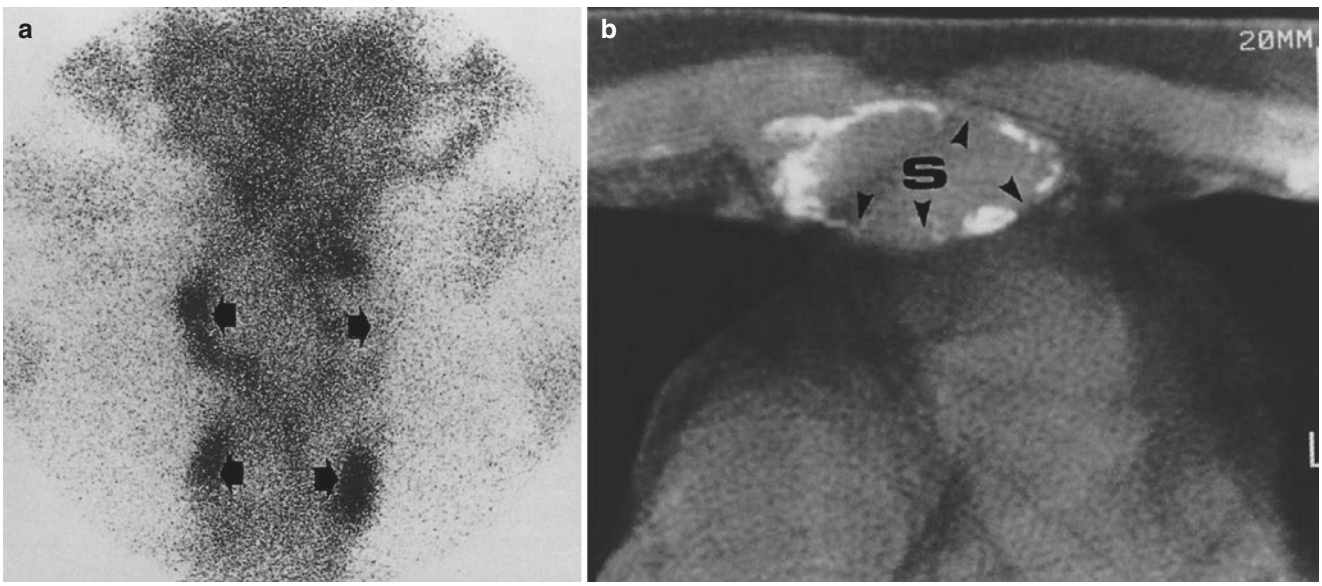

Fig. 17.59 Solitary plasmacytoma in the sternum. (**a**) Anterior pinhole scintigraph of the upper sternum shows expansile photopenic lesions in the upper two segments of the sternal body with bulging cortices that concentrate tracer intensely (*arrows*). The tracer uptake in the left lateral aspect of the uppermost lesion is decreased due to rupture. (**b**) Transverse CT scan of the first sternal segment(s) reveals broken eggshell-like cortical rupture and expansile marrow (*arrowheads*)

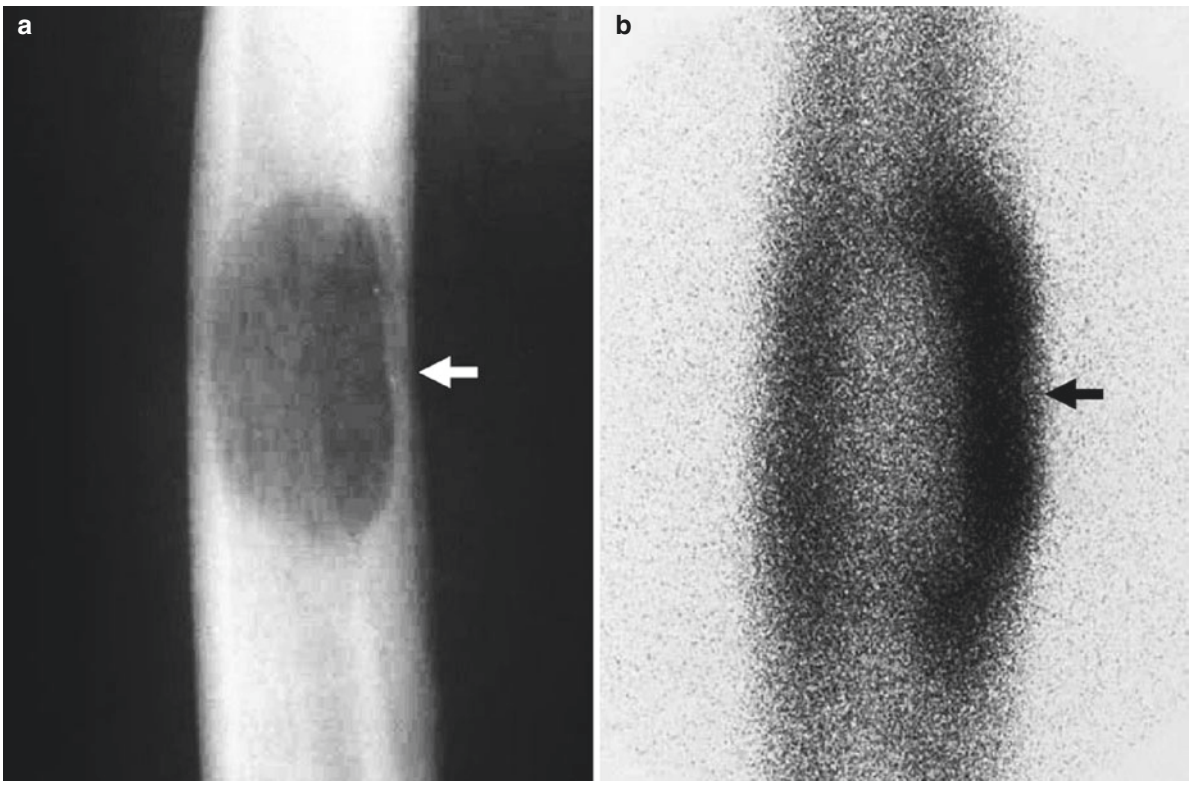

Fig. 17.60 Expansive myeloma with cortical invasion. (**a**) Anteroposterior radiograph of the right femur in a 62-year-old male shows a large ovoid lytic lesion in the marrow space with the invasion of local cortex and periosteum (*arrow*). (**b**) Anterior pinhole scintigraph reveals intense tracer uptake in the cortex (*arrow*)

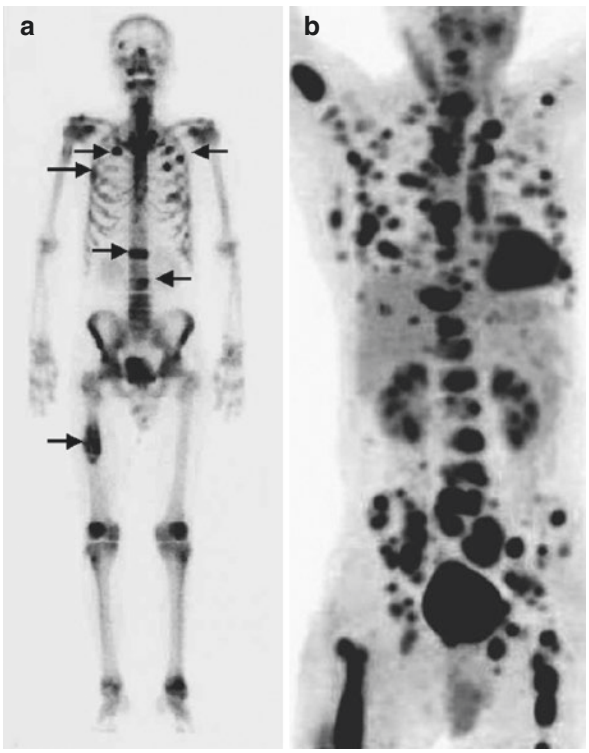

Fig. 17.61 ^{99m}Tc-MDP bone scintigraph and PET in multiple myeloma. (**a**) Anterior whole-body scan shows multiple spotty and mottled tracer uptake involving the skull, ribs, spine, and right femur (*arrows*). (**b**) ^{18}F-FDG PET demonstrates multiple bone uptake. PET is far more revealing because myeloma cells directly accumulate FDG

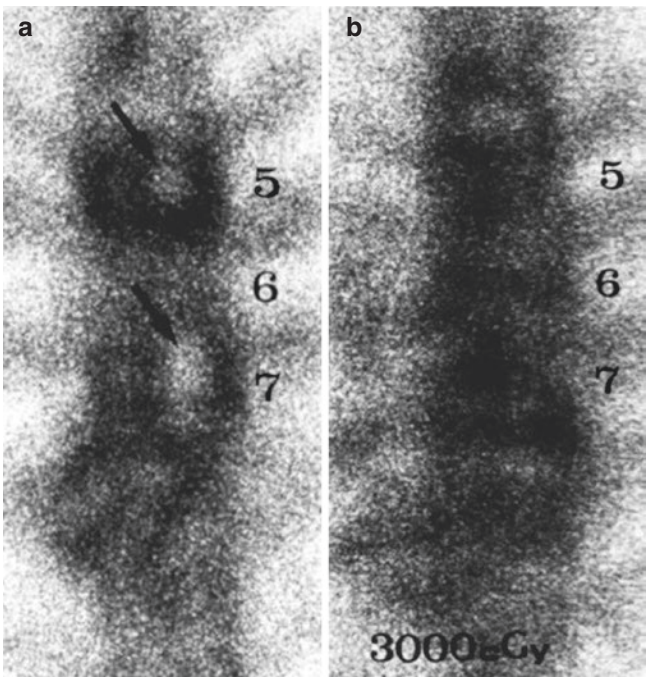

Fig. 17.62 Effect of irradiation effect on myelomas. (**a**) Preirradiation pinhole scan of the midthoracic spine in a 56-year-old female reveals tracer uptake with photon defects in the T5–T7 vertebrae. (**b**) Scan after irradiation (3000 cGy) reveals decreased tracer uptake with cure of the defects

17.3 Leukemias and Lymphomas

Leukemias and lymphomas, respectively, comprise myeloproliferative neoplasms and lymphoreticular tumors of the reticuloendothelial system. Clinically, leukemias are classified into the acute form and the chronic form. Acute leukemia affects both children and adults and chronic leukemia middle-aged adults. Lymphomas arise from the lymphocytic cells, reticulum cells, or primitive precursor cells, and they are pathologically classified as non-Hodgkin's lymphoma, Hodgkin's lymphoma, Burkitt's lymphoma, and mycosis fungoides.

The radiographic changes of bone and bone marrow in acute leukemias are basically not dissimilar to those of multiple myeloma. Thus, radiographic features include diffuse osteopenia, irregular osteolysis and osteosclerosis, lucent metaphyseal band, and periosteal reaction (Fig. 17.63a). Chronic leukemia also manifests as osteopenia and occasional osteolysis that is discrete. On the other hand, lymphomas, both the non-Hodgkin's type and the Hodgkin's type, typically affect the axial bones including the skull, the facial bones, the spine, the pelvis, the ribs, and the femurs. The spread of lymphomas to bone occurs either directly from contiguous lymph nodes or through blood flow. Osteolysis is geographic in appearance with poorly defined borders in large flat or irregular bones such as the sacrum (Fig. 17.64a) or segmental with cortical rupture in small bones such as the ribs (Fig. 17.65a). Endosteal scalloping and periosteal or soft-tissue invasion may occasionally be seen as in myeloma.

^{99m}Tc-MDP bone scintigraphy of acute leukemia in children manifests as band-like uptake in the long-bone metaphyses with small segmental uptake in the diaphyses (Fig. 17.63b). Generally, the scintigraphic features of

Fig. 17.63 Acute lymphocytic leukemia. (**a**) Anteroposterior radiograph of the right proximal tibia in a 16-year-old female shows a mixture of sclerosis and lysis due to leukemia in the metadiaphysis (*arrows*). (**b**) Planar bone scintigraph reveals intense tracer uptake in the right proximal tibial metadiaphysis and left tibial midshaft (*arrows*)

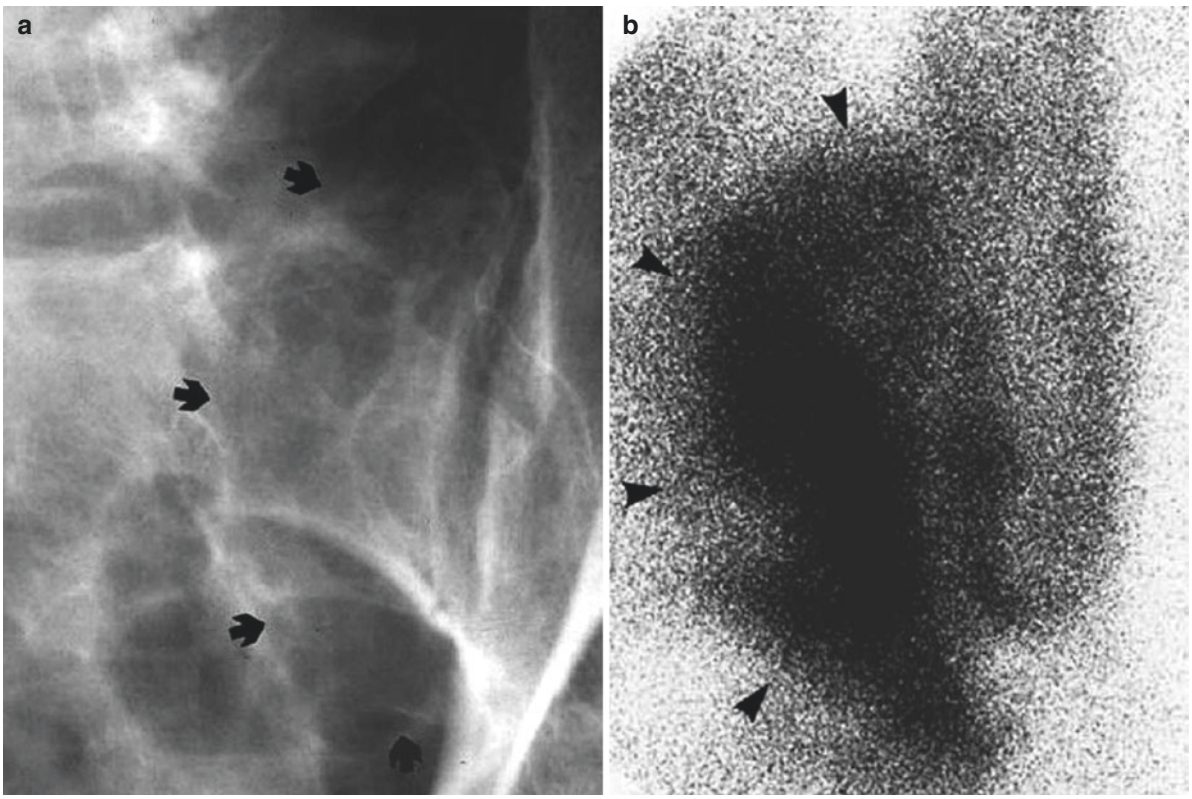

Fig. 17.64 Lymphoma in the sacrum. (**a**) Anteroposterior radiograph of the left half of the sacrum in a 47-year-old female shows a large geographic lysis delimited by the sacroiliac joint barrier (*arrows*). (**b**) Anterior pinhole scintigraph shows concordant tracer uptake (*arrowheads*)

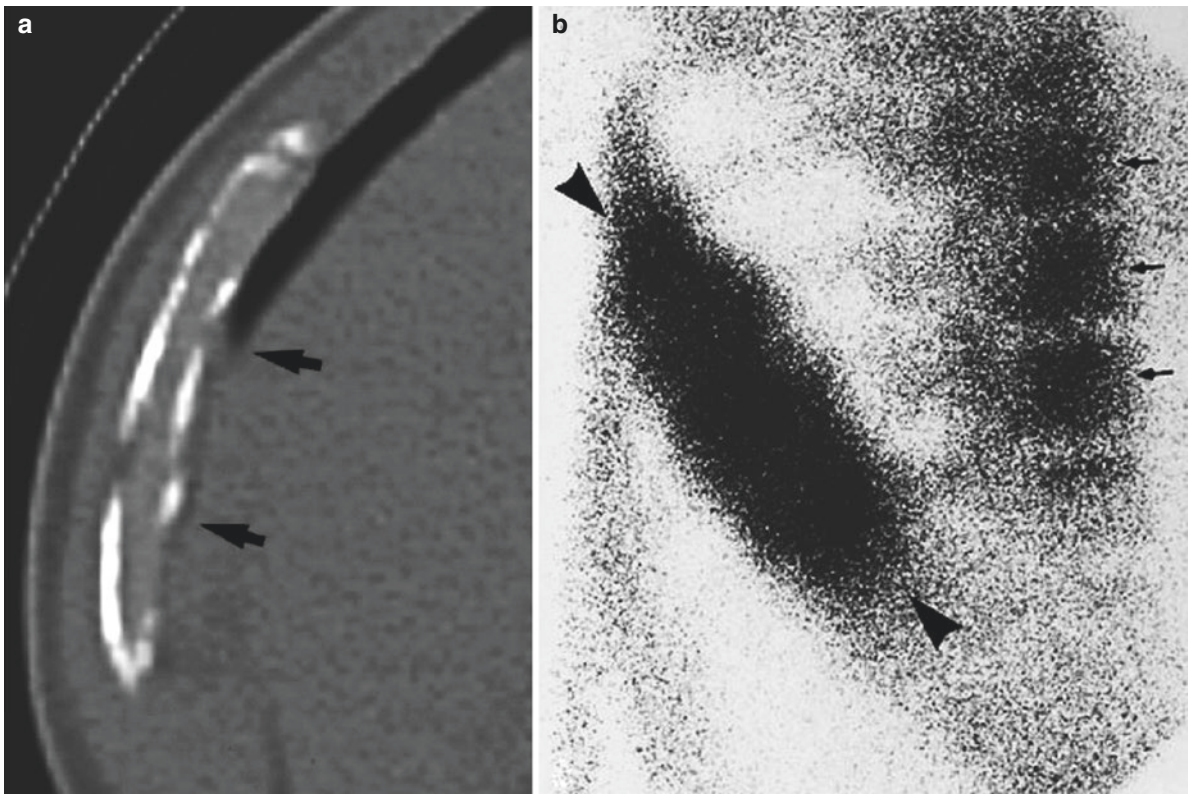

Fig. 17.65 Lymphoma in the rib. (**a**) Transverse CT of the right seventh rib in a 43-year-old male shows an expansive intramedullary lesion with cortical ruptures (*arrows*). (**b**) Pinhole scan reveals intense expansive tracer uptake (*arrowheads*). The uptake in the spine also represents lymphomatous involvement (*arrows*)

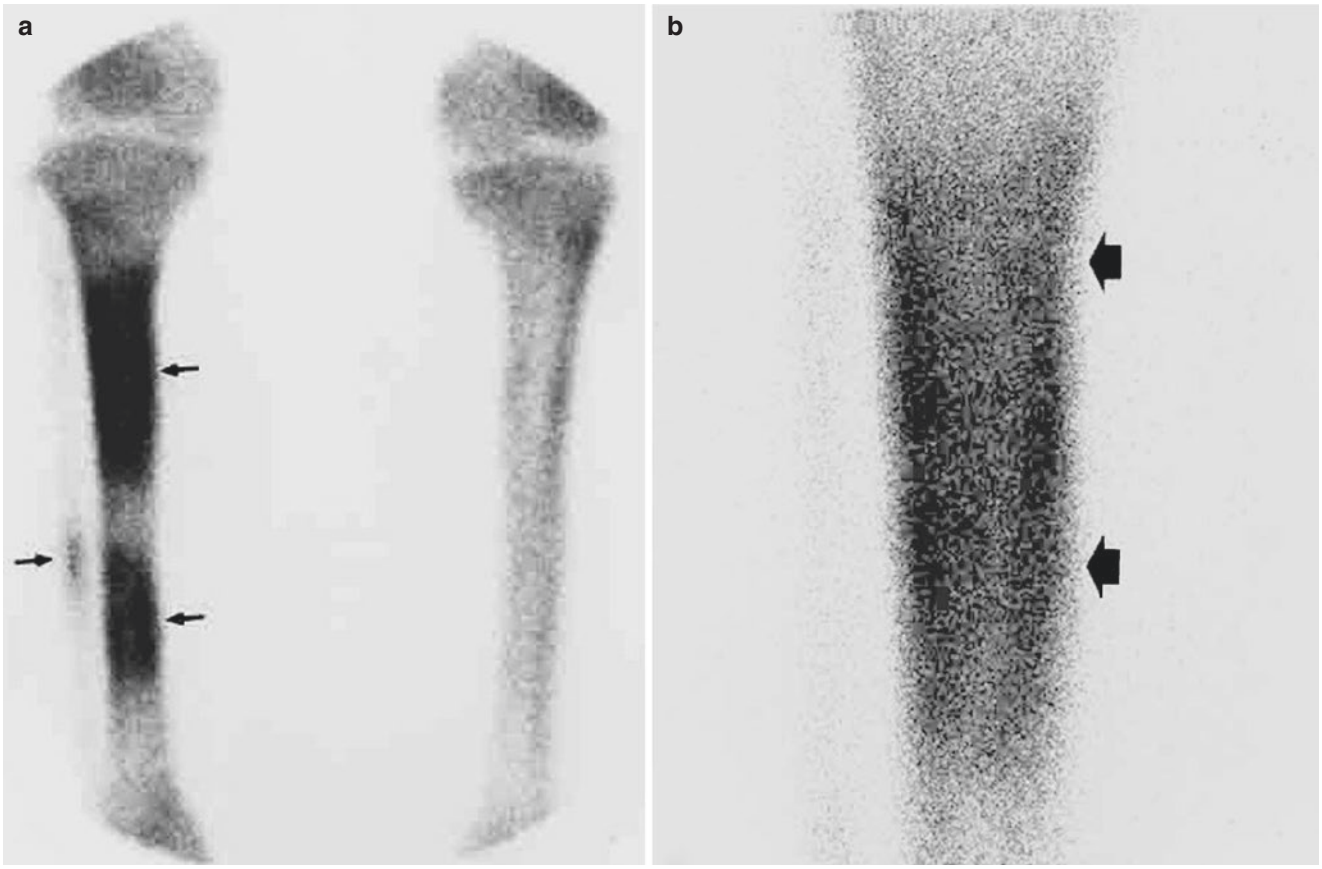

Fig. 17.66 Acute lymphocytic leukemia with endosteal involvement in an adult patient. (**a**) Anterior planar scintigraph of both legs in a 51-year-old female shows segmental tracer uptake in the upper and lower thirds of the right tibia (*pair of arrows*) and fibular midshaft (*single arrow*). (**b**) Anterior pinhole scintigraph localizes increased uptake to localize to endosteums (*arrows*)

lymphoma are similar to those of other osteolytic tumors (Fig. 17.64b). Tracer uptake becomes markedly intensified when the affected bone is fractured (Fig. 17.65b). Lymphocytic leukemia in adults characteristically accumulates tracer in scalloped endosteums of the long bones reflecting bone marrow involvement (Fig. 17.66).

17.4 Chordoma

Chordoma is a slow-growing, low-grade malignancy that arises from primitive notochordal mucoid intercellular material. The tumor is strongly inclined to involve both the caudal sacral region and the clivus near the spheno-occipital synchondrosis. The incidence ranges from 1 to 4% and is nearly twice as common in men as in women, with the vast majority of cases occurring between the fourth and seventh decades of life. Sacrococcygeal lesions are more common in women than in men, whereas the spheno-occipital lesions have an equal sex distribution. Clinical manifestations relate to the location of the tumor. In the early stages the symptoms are mild and nonspecific. Sacrococcygeal invasion causes progressive perineal pain, constipation, urinary difficulties, and bleeding, whereas chordomas at the cranial base lead to increased intracranial pressure and compression of the adjacent structures causing headaches, blurred vision, memory loss, and emotional instability. When vertebrae are involved, tumors invade the spinal cord and nerve roots with pain, numbness, motor weakness, and paralysis.

Radiography shows an expansive, osteolytic mass with a lobular or geographic appearance. Typically, the tumors are located in the midline in the caudal sacrum or the skull base. Sacral chordoma produces an anteriorly protruding mass that contains irregular bony shards when seen on lateral radiographs. Rarely, the entire tumor mass may be located within the sacrum. Not infrequently, the sacral mass is overshaded by the intestinal contents and gas. A CT scan is ideal for revealing the lobular mass with osteolysis and irregular fragmentations (Fig. 17.67a).

Pinhole scintigraphy is valuable for the mapping of large, expansile, intraosseous photonic tumor, which is characteristically situated in the midline of the caudal sacrum. The tumor can be outlined by irregular, interconnected, spotty "hot" areas of reactive or destroyed bones around it (Fig. 17.67b).

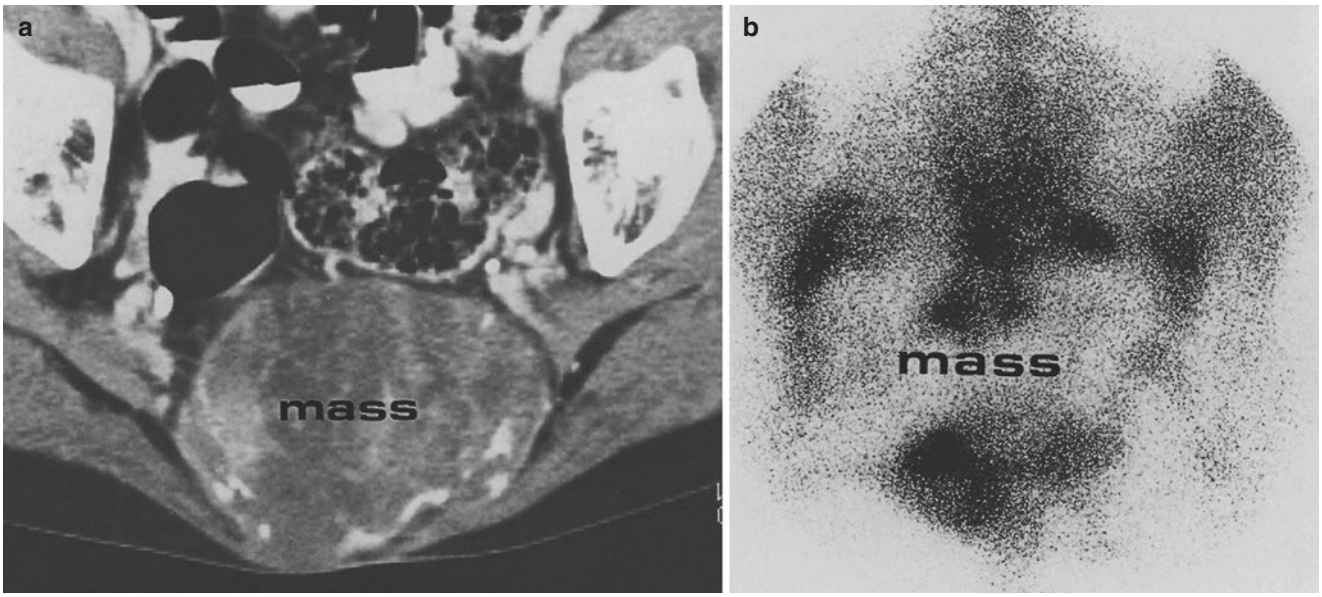

Fig. 17.67 Sacral chordoma with expansile mass. (**a**) Transverse CT scan of the lower sacrum in a 59-year-old woman with a large pelvic mass reveals an expansile tumor with irregularly broken cortices (mass). (**b**) Posterior pinhole scan of the sacrum shows a large, lobulated, photopenic mass (*mass*) surrounded by intense tracer uptake. The lateral borders appear photopenic due to rupture

17.5 Periosteal Leiomyosarcoma

Leiomyomas and leiomyosarcomas outside the uterus and gastrointestinal tract are extremely rare. Conklin et al. (1981) reported a case of leiomyoma that occurred in the tibia. Their case showed mild but diffusely increased tracer uptake. Recently, we came across a case of exophytic leiomyosarcoma arising from the sub-periosteal layer of the juxtaspinal portion of the right ninth rib in a 40-year-old man (Fig. 17.68a,b). The tumor was photopenic with faint tracer uptake in the periphery where a bone fragment was detached from the rib that was widely destroyed (Fig. 17.68c). Moderately intense uptake was noted in the host bone as well as the suprajacent rib that was compressed by the tumor. Histologically, the tumor was necrotic with hemorrhage.

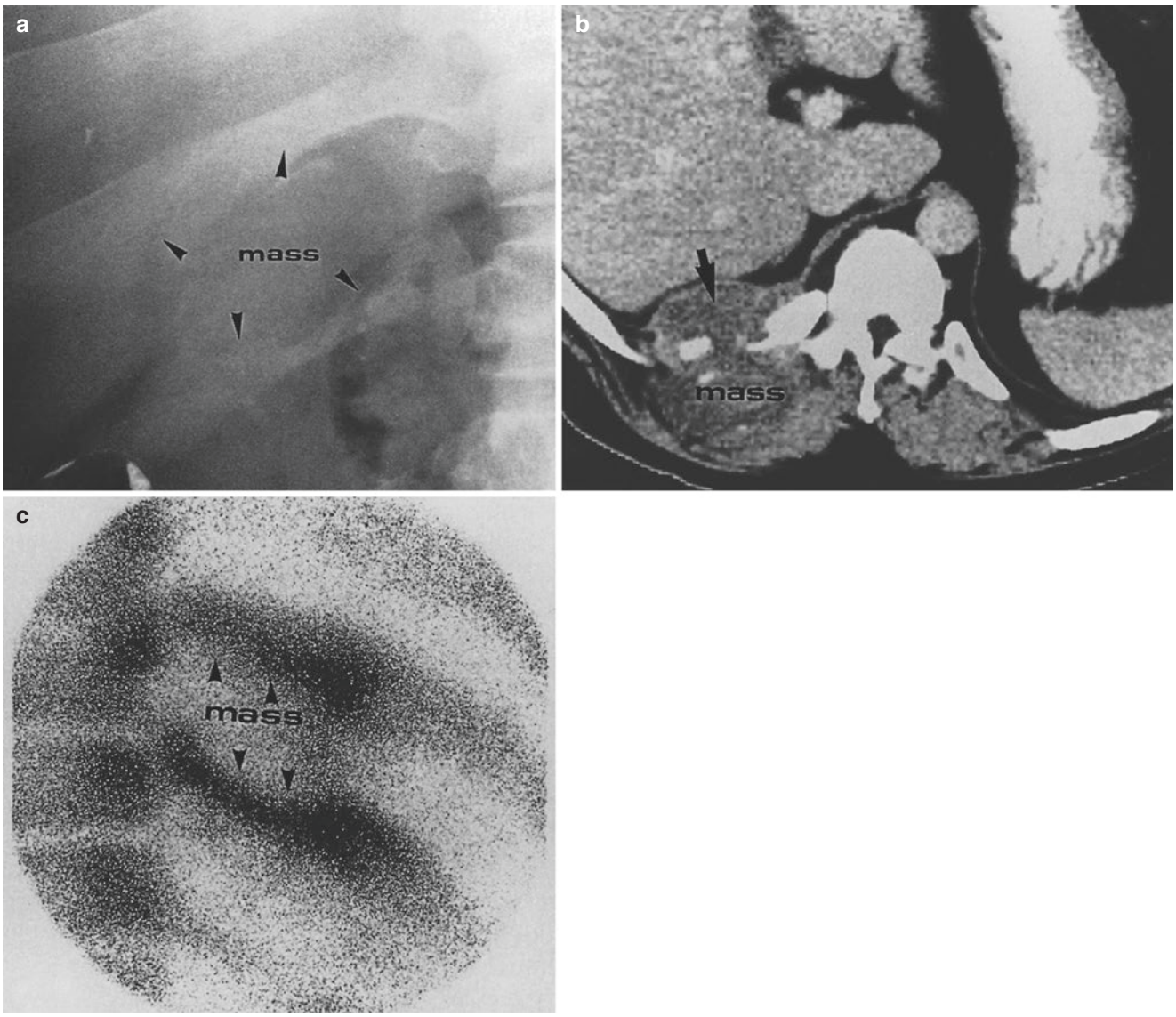

Fig. 17.68 Periosteal leiomyosarcoma with exophytic mass in the rib cage. (**a**) Anteroposterior radiograph of the right lower rib cage in a 40-year-old man shows an ovoid, soft-tissue mass interposed between the two lowermost ribs near the spine (*mass*). The regional ribs are eroded (*arrowheads*). (**b**) Transverse CT scan demonstrates the tumor to be expansile and to consist of a soft-tissue mass (*mass*) with irregular rib destruction (*arrow*). (**c**) Posterior pinhole scintigraph shows moderate tracer uptake in the ribs that are eroded and compressed by the tumor interposed between them. The tumor itself is photopenic (*mass*)

References

Asthana S, Deo SV, Shukla NK, Raina V (2001) Carcinoma breast metastatic to the hand and the foot. Australas Radiol 45:380–382

Baek JH, Lee SY, Kim SH et al (1997) Pinhole bone scintigraphic manifestation of fibrous dysplasia. Korean J Nucl Med 31:452–458

Bahk YW (1996) Pinhole scanning in tumors and tumorous conditions of bone: a new imaging approach to skeletal radiology. J Orthop Sci 1:70–89

Bahk YW (1998) Pinhole scintigraphic diagnosis of bone tumors. J Korean Bone Joint Tumor Soc 4:1–12

Bahk YW, Kim OH, Chung SK (1987) Pinhole collimator scintigraphy in differential diagnosis of metastasis, fracture, and infections of the spine. J Nucl Med 28:447–451

Bahk YW, Park YH, Chung SK, Chi JG (1995) Bone pathological correlation of multimodality imaging in Paget's disease. J Nucl Med 36:1421–1426

Bahk WJ, Rhee SK, Kang YK et al (2006) Gastric cancer acrometastases to all digits of one hand following closed intramedullary nailing. Skelet Radiol 35:529532

Bahk WJ, Lee AH, Chang ED et al (2017) Thymic carcinoma initially presented with geographic destruction of scapula in a child. Skeletal Radiol. doi:10.1007/s00256-017-2696-4

Bourgeois P, Malarme M, Van Franck R et al (1991) Bone marrow scintigraphy in prostatic carcinoma. Nucl Med Commun 12:35–45

Bredella MA, Sreinbach L, Caputo G et al (2005) Value of FDG PET in the assessment of patients with multiple myeloma. Am J Roentgenol 184:1199–1204

Capanna R, Bertoni F, Bacchini P et al (1984) Malignant fibrous histiocytoma of bone. The experience at the Rizzoli Institute: report of 90 cases. Cancer 54:177–187

Citrin DL, McKillop JH (1978) Atlas of technetium bone scans. Saunders, Philadelphia

Coerkamp FG, Kroon HM (1988) Cortical bone metastases. Radiology 169:525–528

Collins MS, Koyama T, Swee RG, Inwards CY (2003) Clear cell chondrosarcoma: radiographic, computed tomographic, and magnetic resonance findings in 34 patients with pathological correlation. Skelet Radiol 32:687–694

Conklin JJ, Camargo EE, Wagner H Jr (1981) Bone scan detection of peripheral periosteal leiomyoma. J Nucl Med 22:97

Cook GJ, Fogelman I (2001) The role of nuclear medicine in monitoring treatment in skeletal malignancy. Semin Nucl Med 31:206–211

Cooper M, Miles KA, Wraight EP, Dixon AK (1992) Degenerative disc disease in the lumbar spine: another cause for focally reduced activity on bone marrow scintigraphy. Skelet Radiol 21:247–249

Deutch A, Resnick D (1980) Eccentric cortical metastases to the skeleton from bronchogenic carcinoma. Radiology 137:49–52

Duncker CM, Carrio I, Berna L et al (1990) Radio-immune imaging of bone marrow in patients with suspected bone metastases from primary breast cancer. J Nucl Med 31:1450–1455

Feggi LM, Spanedda R, Scutellari PN et al (1988) Bone marrow scintigraphy in multiple myeloma. A comparison with bone scintigraphy and skeletal radiology. Radiol Med (Torino) 76:311–315

Fleming WH, McIlraith ID, King R (1961) Photo scanning of bone lesions utilizing strontium 85. Radiology 77:635–636

Focacci C, Lattanzi R, Iadeluca ML, Campioni P (1998) Nuclear medicine in primary bone tumors. Eur J Radiol 27(Suppl 1):S123–S131

Fogelman I, McKillop JH (1991) The bone scan in metastatic disease. In: Rubens RD, Fogelman I (eds) Bone metastases. Springer, Berlin Heidelberg New York

Gabuniia RI, Godin VP, Gristai AA et al (1989) Scintigraphic evaluation of the efficacy of treatment of cancer of the breast with bone metastases. Med Radiol (Mosk) 34:49–53

Gilday DL, Ash JM, Reilly BJ (1977) Radionuclide skeletal survey for pediatric neoplasms. Radiology 123:399–406

Goodgold HM, Chen DCP, Majd M et al (1984) Scintigraphic features of giant cell tumor. Clin Nucl Med 9:526–530

Greenspan A, Norman A (1988) Osteolytic cortical destruction: an unusual pattern of skeletal metastases. Skelet Radiol 17:402–406

Haubold-Reuter BG, Duewell S, Schilcher BR et al (1993) The value of bone scintigraphy, bone marrow scintigraphy and fast spin-echo magnetic resonance imaging in staging of patients with malignant solid tumours: a prospective study. Eur J Nucl Med 20:1063–1069

Hudson TM (1984) Scintigraphy of aneurysmal bone cysts. AJR Am J Roentgenol 142:761–765

Kamby C, Vejborg I, Daugaard S et al (1987) Clinical and radiological characteristics of bone metastases in breast cancer. Cancer 60:2254–2261

Kim EE, Bledin AG, Gutierrez C (1983) Comparison of radionuclide images and radiographs for skeletal metastases from renal cell carcinoma. Oncology 40:284–286

Kim JY, Chung SK, Park YH et al (1992) Pinhole bone scintigraphic appearances of osteoid osteoma. Korean J Nucl Med 26:160–163

Kim SH, Chung SK, Bahk YW (1993) Pinhole scintigraphic demonstration of trabeculated photopenic metastasis from follicular thyroid carcinoma: report of two cases. Korean J Nucl Med 27:305–308

Kirchner PT, Simon MA (1981) Radioisotopic evaluation of skeletal disease. J Bone Joint Surg Am 63:673–681

Lee KH, Chung J-K, Choi CW et al (1995) Technetium-99 m-labeled antigranulocytic antibody bone marrow scintigraphy. J Nucl Med 36:1800–1805

Lemieux J, Guimond J, Laberge F et al (2002) The bone scan flare phenomenon in non-small-cell lung cancer. Clin Nucl Med 27:486–489

Lentle BC, Kotchen T, Catz Z, Penney HF (1987) Detecting bone marrow metastases at the time of examining the liver with radiocolloid. J Nucl Med 28:184–187

Levine E, De Smet AA, Neff JR et al (1984) Scintigraphic evaluation of giant cell tumor of bone. AJR Am J Roentgenol 143:343–348

Lisbona R, Rosenthall L (1979) Role of radionuclide imaging in osteoid osteoma. AJR Am J Roentgenol 132:77–80

McKillop JH (1987) Bone scanning in metastatic disease. In: Fogelman I (ed) Bone scanning in clinical practice. Springer, Berlin, Heidelberg, New York

McLean RG, Murray IPC (1984) Scintigraphic patterns in certain primary malignant bone tumors. Clin Radiol 35:379–383

Murphey MD, wan Jaovisidha S, Temple HT et al (2003) Telangiectatic osteosarcoma: radiographic-pathologic comparison. Radiology 229:545–553

Nadel HT, Rossleigh MA (1995) Tumor imaging. In: Treves ST (ed) Pediatric nuclear medicine, 2nd edn. Springer, Berlin, Heidelberg, New York, pp 496–527

Neumann RD, Kemp JD, Weiner RE (1995) Gallium-67 imaging for detection of malignant disease. In: Sandler MP et al (eds) Diagnostic nuclear medicine, 3rd edn. Williams and Wilkins, Baltimore, pp 1243–1260

Phekoo KJ, Schey SA, Richards MA et al (2004) A population study to define the incidence and survival of multiple myeloma in a National Health Service Region in UK. Br J Haematol 127:299–304

Pinkas L, Robinson D, Halpern N et al (2001) ^{99m}TcMIBI scintigraphy in musculoskeletal tumors. J Nucl Med 42:33–37

Pistenma DA, McDougall IR, Kriss JP (1975) Screening for bone metastases. JAMA 255:46–50

Reske SN, Karstens JH, Gloeckner W et al (1989) Radioimmunoimaging for diagnosis of bone marrow involvement in breast cancer and malignant lymphoma. Lancet 1(8633):299–301

Tanaka S, Matsumura Y, Tanaka M et al (1991) Bone metastases in breast cancer and its risk factor—follow up study by bone scintigraphy. Kaku Igaku 28:1177–1180

Wahner HW, Kyle RA, Beabout JW (1980) Scintigraphic evaluation of the skeleton in multiple myelomas. Mayo Clin Proc 55:739–746

Waxman AD (1995) Thallium-201 and technetium-99 m methoxyisobutyl isonitrile in nuclear oncology. In: Sandler MP et al (eds) Diagnostic nuclear medicine, 3rd edn. Williams and Wilkins, Baltimore, pp 1261–1274

Waxman AD, Siensen JK, Levine AM et al (1981) Radiographic and radionuclide imaging in multiple myeloma: the role of gallium scintigraphy. J Nucl Med 22:256–260

WHO (2002). Tumors of soft tissue and bone.

Widding A, Stilbo I, Hansen SW et al (1990) Scintigraphy with nanocolloid Tc-99 m in patients with small cell lung cancer, with special reference to bone marrow and hepatic metastases. Eur J Nucl Med 16:717–719

Yuasa K, Sugimura K, Okizuka AH et al (1991) Bone infarction and fat island appearing as local defects in radionuclide bone marrow imaging. Kaku Igaku 28:91–96

Zeifang F, Sabo D, Ewerbeck V (2000) Pathological fractures in primary malignant bone tumors. Chirurg 71:1121–1125